University of Leoben

Doctoral Thesis

Mechanical elastic constants of thin films determined by X-ray diffraction

Klaus Martinschitz

Leoben, July 2008

July 31^{st}, 2008

This doctoral thesis was typeset by the use of KOMA-Script and LaTeX 2_ε.
The template was modified by Dr. Weinhandl and Dr. Vorhauer.

Erich Schmid Institute of Materials Science
Austrian Academy of Sciences
Jahnstrasse 12
A-8700 Leoben
http://www.oeaw.ac.at/esi

Affidavit

I declare in lieu of oath, that I wrote this thesis and performed the associated research myself, using only literature cited in this volume.

Leoben, July 2008

Acknowledgements

I would like to express my gratitude to a number of persons who have contributed and supported me during course of this work. I, particularly, wish to thank:

- Jozef Keckes, my supervisor, for his guidance and support, for the numerous discussions we had and for giving an expertise to this thesis.
- Gerhard Dehm, my co-supervisor and the Head of the Department of Materials Physics, for his support and help and the patience especially during the early stages of my work.
- My family and friends for their support and friendship.
- Balder Ortner, for teaching me fundamental aspects of crystallography.
- Martin Hafok, for supporting me in all kind of mathematical aspects and texture analysis.
- Franz Hubner, Günter Aschauer and Hannes Schlager for assembling technical equipment in the workshop.
- Edeltraud Haberz and Gabriele Moser for their excelent sample preparation.
- Herbert Weinhandl for the modified LaTeX 2_ε template.
- All other employees of the Erich Schmid Institute for their help.
- Austrian Science Fund FWF and Austrian NANO Initiative for supporting this thesis within the project "StressDesign - Development of Fundamentals for Residual Stress Design in Coated Surfaces"

Abstract

This thesis presents a new methodology to quantify mechanical elastic constants of polycrystalline thin films using X-ray diffraction under static conditions. The approach is based on the combination of X-ray diffraction substrate curvature and $\sin^2\psi$ methods. It is shown how to extrapolate the mechanical elastic constants from X-ray elastic constants considering crystal and macroscopic elastic anisotropy. A general formula is presented which can be used to determine a reflection *hkl* and its corresponding value of the X-ray anisotropic factor $3\Gamma_{hkl}$ for which the X-ray elastic strain is equal to the mechanical strain. The method is applied to Cu/Si(100), CrN/Si(100) and TiN/Si(100) thin films deposited onto monocrystalline Si(400) substrates at room temperature. It is demonstrated that, for fiber textured thin films, the $3\Gamma_{hkl}$ value depends strongly on the fiber texture sharpness and the amount of randomly oriented crystallites. The advantage of the new technique remains in the fact that mechanical moduli are determined non-destructively and represent volume-averaged quantities.

Kurzfassung

Diese Arbeit beschreibt eine neue Methode um mechanische elastische Konstanten von polykristallinen dünnen Schichten mittels Röntgendiffraktion unter statischen Bedingungungen zu bestimmen. Die Methode basiert auf einer Kombination der Röntgendiffraktion Substratbiegungs- und der $\sin^2\psi$ Methode. Es wird gezeigt, wie man mechanische elastische Konstanten aus den röntgenographischen elastischen Konstanten, unter Berücksichtigung der kristallinen und makroskopischen Anisotropie, extrapolieren kann. Es wird eine allgemeine Formel präsentiert, die es erlaubt einen kristallographischen Reflex *hkl*, und seinen zugehörigen röntgenographischen Anisotropiefaktor $3\Gamma_{hkl}$, zu bestimmen, bei dem die mechanische Dehnung gleich der röntgenographischen Dehnung ist. Die Methode wird auf die Schichtsysteme Cu/Si(100), CrN/Si(100) und TiN/Si(100) bei Raumtemperatur angewandt. Es wird gezeigt, dass für fasertexturierte Materialien der $3\Gamma_{hkl}$ Wert unterschiedlich zu dem vorhergesagten $3\Gamma_{hkl} = 0.6$ Wert für makroskopisch isotrope Materialien ist. Der Wert $3\Gamma_{hkl}$ hängt von der Textur, der Texturschärfe, sowie vom Mengenanteil der zufällig orientierten Kristallite ab. Der Vorteil der neuen Methode liegt darin, dass mechanische Moduli zerstörungsfrei bestimmt werden können und volumengemittelte Werte darstellen.

Scientia et potentia in idem coincidunt

Francis Bacon (1561 – 1626)

List of abbreviations

a_0	Unstressed lattice parameter
d_0^{hkl}	Unstressed lattice spacing
$d_{\phi,\psi}^{hkl}$	Lattice spacing
$\vec{g}$	Scattering vector
$a_{ij}^{\Phi_1}$	Φ_1 Euler matrix
a_{ij}^{Φ}	Φ Euler matrix
$a_{ij}^{\Phi_2}$	Φ_2 Euler matrix
a_{ij}^{ϕ}	ϕ rotation matrix
a_{ij}^{ψ}	ψ rotation matrix
a_{ij}^{λ}	λ rotation matrix
a_{ij}^{Ω}	Ω rotation matrix
a_{ij}	Rotation matrix $S \rightarrow C$
a_{ij}^{ϵ}	Bunge rotation matrix
a_{ij}^{γ}	γ rotation matrix $L \rightarrow C$
a_{ij}^{ρ}	ρ rotation matrix $S \rightarrow L$
$\{\sigma_{ij}\}$	Stress tensor
$\left\{\sigma_{ij}^{S}\right\}$	Stress tensor in S system
$\left\{\sigma_{ij}^{L}\right\}_{\psi}$	Stress tensor in L system
$\{\epsilon_{ij}\}$	Strain tensor
$\left\{\epsilon_{ij}^{S}\right\}^{\mathrm{M}}$	Mechanical strain tensor in S system
$\left\{\epsilon_{ij}^{L}\right\}_{\psi}^{\mathrm{M}}$	Mechanical strain tensor in L system
$\left\{\epsilon_{ij}^{S}\right\}^{hkl}$	X-ray strain tensor in S system
$\left\{\epsilon_{ij}^{L}\right\}_{\psi}^{hkl}$	X-ray strain tensor in L system
$\left\{\epsilon_{ij}^{S}\right\}^{\mathrm{R},hkl}$	Reuss X-ray strain tensor in S system
$\left\{\epsilon_{ij}^{L}\right\}_{\psi}^{\mathrm{R},hkl}$	Reuss X-ray strain tensor in L system

$\left\{\epsilon_{ij}^{S}\right\}^{\mathrm{V}}$	Voigt X-ray strain tensor in S system
$\left\{\epsilon_{ij}^{L}\right\}_{\psi}^{\mathrm{V}}$	Voigt X-ray strain tensor in L system
$\left\{\epsilon_{ij}^{S}\right\}^{\mathrm{H},hkl}$	Hill X-ray strain tensor in S system
$\left\{\epsilon_{ij}^{L}\right\}_{\psi}^{\mathrm{H},hkl}$	Hill X-ray strain tensor in L system
$\left\{s_{ijkl}^{S}\right\}$	Compliance tensor in S system
$\left\{s_{ijkl}^{L}\right\}_{\psi}$	Compliance tensor in L system
$\left\{s_{ijkl}^{S}\right\}^{\mathrm{M}}$	Mechanical compliance tensor in S system
$\left\{s_{ijkl}^{L}\right\}_{\psi}^{\mathrm{M}}$	Mechanical compliance tensor in L system
$\left\{s_{ijkl}^{S}\right\}^{\mathrm{R,M}}$	Reuss mechanical compliance tensor in S system
$\left\{s_{ijkl}^{L}\right\}_{\psi}^{\mathrm{R,M}}$	Reuss mechanical compliance tensor in L system
$\left\{s_{ijkl}^{S}\right\}^{\mathrm{V}}$	Voigt compliance tensor in S system
$\left\{s_{ijkl}^{L}\right\}_{\psi}^{\mathrm{V}}$	Voigt compliance tensor in L system
$\left\{s_{ijkl}^{S}\right\}^{\mathrm{H,M}}$	Hill mechanical compliance tensor in S system
$\left\{s_{ijkl}^{L}\right\}_{\psi}^{\mathrm{H,M}}$	Hill mechanical compliance tensor in L system
$\left\{s_{ijkl}^{S}\right\}^{hkl}$	X-ray compliance tensor in S system
$\left\{s_{ijkl}^{L}\right\}_{\psi}^{hkl}$	X-ray compliance tensor in L system
$\left\{s_{ijkl}^{S}\right\}^{\mathrm{R},hkl}$	Reuss X-ray compliance tensor in S system
$\left\{s_{ijkl}^{L}\right\}_{\psi}^{\mathrm{R},hkl}$	Reuss X-ray compliance tensor in L system
$\left\{s_{ijkl}^{S}\right\}^{\mathrm{V}}$	Voigt X-ray compliance tensor in S system
$\left\{s_{ijkl}^{L}\right\}_{\psi}^{\mathrm{V}}$	Voigt X-ray compliance tensor in L system
$\left\{s_{ijkl}^{S}\right\}^{\mathrm{H},hkl}$	Hill X-ray compliance tensor in S system
$\left\{s_{ijkl}^{L}\right\}_{\psi}^{\mathrm{H},hkl}$	Hill X-ray compliance tensor in L system
$\left\{c_{ijkl}^{S}\right\}$	Stiffness tensor in S system
$\left\{c_{ijkl}^{L}\right\}_{\psi}$	Stiffness tensor in L system
$\left\{c_{ijkl}^{S}\right\}^{\mathrm{M}}$	Mechanical stiffness tensor in S system

$\left\{c^L_{ijkl}\right\}^{\mathrm{M}}_{\psi}$	Mechanical stiffness tensor in L system
$\left\{c^S_{ijkl}\right\}^{\mathrm{R,M}}$	Reuss mechanical stiffness tensor in S system
$\left\{c^L_{ijkl}\right\}^{\mathrm{R,M}}_{\psi}$	Reuss mechanical stiffness tensor in L system
$\left\{c^S_{ijkl}\right\}^{\mathrm{V}}$	Voigt stiffness tensor in S system
$\left\{c^L_{ijkl}\right\}^{\mathrm{V}}_{\psi}$	Voigt stiffness tensor in L system
$\left\{c^S_{ijkl}\right\}^{\mathrm{H,M}}$	Hill mechanical stiffness tensor in S system
$\left\{c^L_{ijkl}\right\}^{\mathrm{H,M}}_{\psi}$	Hill mechanical stiffness tensor in L system
$\left\{c^S_{ijkl}\right\}^{hkl}$	X-ray stiffness tensor in S system
$\left\{c^L_{ijkl}\right\}^{hkl}_{\psi}$	X-ray stiffness tensor in L system
$\left\{c^S_{ijkl}\right\}^{\mathrm{R},hkl}$	Reuss X-ray stiffness tensor in S system
$\left\{c^L_{ijkl}\right\}^{\mathrm{R},hkl}_{\psi}$	Reuss X-ray stiffness tensor in L system
$\left\{c^S_{ijkl}\right\}^{\mathrm{H},hkl}$	Hill X-ray stiffness tensor in S system
$\left\{c^L_{ijkl}\right\}^{\mathrm{H},hkl}_{\psi}$	Hill X-ray stiffness tensor in L system
$\{s_1\}^{hkl}$	X-ray elastic constant
$\left\{\frac{1}{2}s_2\right\}^{hkl}$	X-ray elastic constant
$3\Gamma_{hkl}$	X-ray anisotropy factor
$3\Gamma^*_{hkl}$	X-ray anisotropy factor for a definite ψ_{FWHM}, ISO and $3\Gamma_{uvw}$
$3\Gamma_{uvw}$	Fiber texture orientation parameter
ψ_{FWHM}	Texture sharpness parameter
ISO	Fraction of randomly oriented crystallites
$\left\{E^L_{3333}\right\}^{\mathrm{M}}_{\psi}$	Mechanical Young's modulus in $\vec{L}_3$ direction.
$\left\{E^L_{3333}\right\}^{100}_{\psi}$	X-ray Young's modulus of (100) reflex in $\vec{L}_3$ direction.
$\left\{E^L_{3333}\right\}^{110}_{\psi}$	X-ray Young's modulus of (110) reflex in $\vec{L}_3$ direction.
$\left\{E^L_{3333}\right\}^{311}_{\psi}$	X-ray Young's modulus of (311) reflex in $\vec{L}_3$ direction.
$\left\{E^L_{3333}\right\}^{111}_{\psi}$	X-ray Young's modulus of (111) reflex in $\vec{L}_3$ direction.
$\left\{E^{100}\right\}^{\mathrm{M}}$	Mechanical Young's modulus in $\langle 100\rangle$ direction
$\left\{E^{111}\right\}^{\mathrm{M}}$	Mechanical Young's modulus in $\langle 111\rangle$ direction

Contents

1 Introduction

In the last decades thin films became tremendously important in science and technology. They are either used as passive structural elements to improve physical and chemical parameters of engineering components [1, 2] or as active devices in optics and in microelectronics [3].

In engineering, bulk materials are often coated with thin films to protect them from abrasion [4, 5]. The first choice to protect bulk materials are nitride, carbide and boride thin films [6, 7]. They have useful properties because of their high hardnesses and wear resistance and are commonly used as coatings for cutting and drilling tools.

Mechanical properties and residual stress state influence decisively the structural integrity and the performance of thin films [8–10]. Great endeavor has been made to characterize the residual stresses within thin films due to their crucial importance regarding reliability [11–16]. There are manifold origins for residual stresses [17–21]. Residual stresses can be formed during the growth process when islands are formed [22, 23] or coalesce. The lattice mismatch between the substrate and the thin film causes misfit strains which result in stresses in the thin film [24]. The stresses also can be a result of the mismatch between the thermal expansion coefficient of the film and the substrate [20] or of ion implantation [21] during a PVD process. The residual stresses directly influence the behaviour of the thin film either positively or negatively. In protective nitride, boride and carbide thin films high compressive stresses are demanded at the surface to improve the resistance against crack initiation whereas moderate stresses at the thin film substrate interface can assure the adhesion.

Stresses and strains are described by field tensors, mathematical objects which can uniquely identify the physical stress or strain state of the material [25]. The stress and strain tensors are related by *property tensors*. The material's properties described through property tensors are fixed to the physical properties of the material for a given temperature and pressure.

All tensor components describing physical properties are expressed in an orthogonal coordinate system. This coordinate system is called *physical coordinate system*. The tensor relating the strain tensor components to the stress tensor components is called stiffness tensor. The stiffness tensor is a 3 dimensional rank 4 tensor [26, 27]. Its tensor components can be transformed using tensor transformation rules. There is a matrix notation first introduced by Voigt which can be used to calculate the inverse of the stiffness tensor. The compliance and stiffness tensors are the mathematical descriptions of the physical property of stiffness which is a result of the atom's binding structure. Although the stiffness of pure single crystals can easily be described [24, 25] or even calculated with theoretical physics [28–30], the engineering aspect of stiffness is much more complicate. Engineers rarely have to deal with single crystals unless they work in semiconductor industry. The most common case are polycrystals. Polycrystals, however, have got an averaged stiffness tensor and their elastic behaviour must be described through grain interaction models [31–36].

It was the work of Voigt [31] which described the first grain interaction model of polycrystals. Voigt assumed the strain tensor components to be equal for all grains. This leads to discontinuities of the stress state between two grains when grain boundary interactions are neglected. Nevertheless the Voigt model is of tremendous importance for theoretical considerations. It is the only grain interaction model where mechanical strain and diffraction strain are equal.

The second grain interaction model was introduced by Reuss [32]. Reuss assumed the stress tensor components to be equal in all grains. This directly implicates that the grain agglomerate can not meet strain boundary conditions between all grains.

In the year 1952, Hill proposed a grain interaction model which is a mean average of the Reuss and Hill model [33]. Beside many other grain interaction models developed in the past decades the Hill model is still of great importance for thin films and can be calculated rather easily.

Eshelby [34] was the first who considered the morphology of particles inside an indefinite matrix to calculate the averaged compliance tensor of a material. This concept can also be used to calculate the averaged compliance tensor of a single phase polycrystalline material. In this model one grain is considered to be the particle and the surrounding grains are the infinite matrix. Although the Eshelby model was a great step in grain interaction modeling it is rarely applied to thin films. Thin films are typically thinner than 5µm and the condition of an indefinite matrix does not hold anymore for all directions.

Intensive research effort has been made in the field of grain interaction models [36–38] in the last years. Nevertheless, the research of grain interaction models continues due to the fact that the behaviour of multi phase materials, grain boundaries, inclusions *etc.* is still not understood.

X-ray strain analysis is performed through X-rays or neutrons [26, 39–41]. Neutrons are extremely useful for analysing bulk materials due to the fact that their penetration depth is much larger than the X-ray's penetration depth. However, neutron scattering can only be performed at neutron sources which are not as accessible as X-ray sources. The principles of X-ray strain measurement were defined in the first decades of the

20^{th} century [42] when X-rays were used to determine and analyse single crystalline and polycrystalline structures. It is still common to use different coordinate systems to express physical properties in terms of their tensor properties. Diffraction techniques are sensitive only in the direction of the scattering vector. This disadvantage makes it absolutely necessary to find a correlation between the information obtained by scattering techniques and the volume-avegared physical properties of the material. The averaged strain value in direction of the scattering vector is, in general, not equal to the averaged mechanical strain of the material. The averaged stress state of a material must correlate with the mechanical strain as well as with the diffraction strain. The general description of the stress-strain relation is a tensor equation which can be simplified if the stress state in the thin film is equibiaxial. Although there is great interest in determining the X-Ray elastic constants of materials in the X-ray diffraction community, the mechanical elastic constants (MECs) are of common interest for engineers. The MECs are the parameters which correlate the averaged mechanical strain with the averaged mechanical stress. There are many techniques available to determine the mechanical elastic constants. Elastic properties of thin films are usually determined by nanoindentation [43], by surface acoustic wave technique [44], by straining or bending of thin film structures [45] or by resonance ultrasound [46]. However, many of these techniques can only be applied to bulk materials or are time consuming. The most crucial aspect of determining MECs of thin films is the anisotropy. Although anisotropy is a common fact in nearly all materials, it is of tremendous importance in thin films. In most cases the formation of thin films is preceded by island growth. The islands grow from nuclei which are orientated in respect to the substrate they form on. In the case of single crystal Si(100) substrate the texture can be assumed to be very sharp. The macroscopic anisotropy of the averaged MECs is a direct result of the crystal anisotropy and the anisotropic distribution of grains in the polycrystal material. Therefore the macroscopic anisotropy can be influenced regarding to the crystal anisotropy, the fraction of crystallites randomly oriented and the texture sharpness. These three parameters can easily be used to characterize the whole single phase grain agglomerate. However, in many cases the single crystal compliances are not accessible. Either they have not been measured or they are not accurate enough. Singe crystal compliances can be determined from the mechanical behaviour of polycrystalline materials. For this purpose, polycrystals are in-situ deformed whereby stress and strain are usually monitored [47–50]. The techniques to determine the single crystal elastic constants from polycrystals [51, 52] can be applied to isotropic bulks but rarely to textured thin films.

This thesis will show up a new method to calculate the X-ray elastic constants and mechanical elastic constants of thin films using only diffraction techniques. The experiments were performed in laboratory as well as on synchrotron radiation facilities.

Thin films deposited on substrates at high temperatures and with a difference in coefficient of thermal expansion (CTE) will experience a thermal stress when cooled down to room temperature. This thermal stress is responsible for the bending of the thin film - substrate composite. In 1909 Stoney [53] developed a mathematical formalism which can be used to determine the curvature, and therefore the stress within the

thin film, of the bended system. Many different techniques were developed to determine the curvature of such systems. This thesis will use a method which is well known in industry for determining the waviness of single crystal substrates [54]. However, the combination of this technique together with the theoretical methods developed to determine the X-ray strain will show up a totally new, powerful and easy method to determine the XECs and MECs for one phase materials with cubic crystal symmetry.

In Cha. 2, the simulation of the mechanical behaviour of thin films is explained. The three grain interaction models of Reuss [32], Voigt [31] and Hill [33] will be summarized. The mathematical background which has extensively been discussed in literature will be explained to give an insight into the topic of grain interaction models. The λ-trail at different ψ angles is displayed for the Reuss model which delivers the reader an insight into possible errors which can come along when calculating the X-ray elastic compliances. The generation of the ODF data, the analysis of the ODF's symmetry, its implementation into software and the mathematical definition of the ODF are presented in Sec. 2.4.

In Cha. 3 the experimental methods will be introduced which have been applied to determine the data for the thesis. This chapter is focused on sample preparation, diffraction techniques, the X-ray curvature technique and the texture analysis. The X-ray curvature method will be explained. The method is used to determine the curvature of a thin film - substrate composite. The determination of the curvature leads to the calculation of the averaged macroscopical equibiaxial stress state in the thin film. Although there are many techniques available to determine the curvature of a thin film - substrate composite, the X-ray curvature method is introduced as an indispensable part of the technique used to determine the MECs and XECs.

In Cha. 4 the empirical data will be shown for three different materials. The calculated X-ray strains determined from the measured lattice parameters as a function of $\sin^2\psi$ are plotted and the $3\Gamma_{hkl}$-plots for different crystallographic reflections are shown.

Finally, Cha. 5 gives a summary and an outlook for further possible experiments.

The appendix lists all first author papers concerning the topic of residual stresses and determination of mechanical elastic constants which were published or submitted within the time of the PhD thesis to peer-reviewed journals and as conference proceedings.

The novel, scientific aspect of this thesis is to show up and prove a new method for the determination of XECs and MECs. This work is dedicated to the determination of mechanical elastic constants in polycrystalline, textured cubic materials using X-ray diffraction.

2 Simulations

2.1 General considerations

Within this chapter it will be shown that it is possible to determine the *mechanical out-of-plane* Young's modulus, a Poisson's ratio and the *mechanical in-plane* biaxial modulus of a thin film using diffraction techniques. Due to the fact that the measured X-ray strain depends on the texture of the thin film, the anisotropy of the thin film must be considered first. The influence of the anisotropy on the mechanical properties of the thin films is studied with simulations performed with software Mathematica™ [55]. The three most important grain interaction models of Reuss [32], Voigt [31] and Hill [33] were used to calculate the anisotropy of X-ray strain as a function of polar angle ψ [56, 57] for an equibiaxial stress state of 100 MPa. Moreover, this chapter will highlight the simulation of mechanical and X-ray elastic constants as a function of texture, texture sharpness (ψ_{FWHM}) and fraction of randomly oriented crystallites (ISO) of the grain agglomerate. Finally, the simulations will result in a new method which can be used to determine the mechanical elastic constants of textured thin films.

2.2 Tensors

Mechanical elastic constants can be expressed using tensors. Briefly, a tensor is a mathematical object which has got invariant properties under coordinate system transformations. A tensor of rank 0 is called scalar and its invariant property is the scalar value itself [58]. A tensor of rank 1 is called vector and its invariant property is the euclidic norm, *i.e.* its length. The first degree invariant properties of rank 2 tensors are the trace and the determinant of the tensor. Beside first degree invariant properties, a rank 2 tensor has got second degree invariant properties. These are the squared trace and the sum of all squared tensor elements [59]. In euclidic

space, the only mathematical transformations which obtain the invariant properties mentioned are represented through orthogonal matrices, *i.e.* the column and row space elements of the matrices are orthogonal to each other [25]. It can be shown that the only allowed mathematical operations are rotation, inversion and mirroring [25]. These operations can be identified by the determinant of the matrix. Rotation matrices always have $det = +1$ whereas mirroring and inversion matrices have $det = -1$. Each tensor is described through its tensor components. The tensor itself is invariant regarding to coordinate system transformation but its components are, in general, variant. However, there are exceptions such as the identity tensor [60], the epsilon tensor [60] or all scalars which conserve their only tensor component regarding to coordinate system transformation. Following convention is used for naming tensors. All tensors are surrounded with {} brackets to apply different sub- and superscripts to them. Tensors indexed with the letters S, L, C and Ω written as superscript index define the tensor properties in terms of the sample, laboratory, crystal and intermediate coordinate system, *e.g.* $\left\{S^L_{ijkl}\right\}$ are the tensor components in respect to the laboratory system L. The rotation of the L system in respect to the S system is described with a subscript ψ outside the {} brackets, *e.g.* $\left\{S^L_{ijkl}\right\}_\psi$. If ψ is written as subscript outside the {} brackets, the L letter can (but need not) be omitted. The tensors which have to be distinguished regarding the grain interaction models are marked with R(Reuss),V(Voigt) or H(Hill) as additional superscript outside the brackets {}. For example, $\left\{S^L_{ijkl}\right\}^{\mathrm{H}}_\psi$ are the tensor components according to the Hill model. The difference between tensors expressing X-ray and mechanical properties is denoted with *hkl* (X-Ray) or M(mechanical) outside the {} brackets, *e.g.* $\left\{S^L_{ijkl}\right\}^{\mathrm{H},hkl}_\psi$ or $\left\{S^L_{ijkl}\right\}^{\mathrm{H,M}}_\psi$. The tensor components of a rank n tensor are transformed according to Eq. 2.1.

$$\left\{s'_{i'j'..n'}\right\} = a_{i'i}a_{j'j}..a_{n'n}\left\{S_{ij..n}\right\} \tag{2.1}$$

where a is either a matrix of rotation, inversion or mirroring and a_{ij} are its matrix components. Within this thesis only rotation matrices will be used. Second rank tensors can be inverted if their determinant does not equal zero. Higher rank tensors are inverted using the Voigt notation [26, 27]. The Voigt notation is the description of a higher rank tensor in matrix form. It must be emphasized that the law of tensor transformation does not hold for a matrix in Voigt notation. However, the Voigt matrix can easily be inverted and its inverse is transformed back to the desired tensor. Following rules must be applied to transform tensor components to matrix components and vice versa [26]

Table 2.1: Transformation between tensor indices and Voigt matrix indices [26].

tensor notation	11	22	33	23,32	31,13	12,21
matrix notation	1	2	3	4	5	6

$$\begin{aligned} S_{ijkl} &= S_{mn} && \text{When m and n are 1,2 or 3} \\ S_{ijkl} &= \frac{1}{2} S_{mn} && \text{When either m and n are 4,5 or 6} \\ S_{ijkl} &= \frac{1}{4} S_{mn} && \text{When both m and n are 4,5 or 6} \end{aligned} \tag{2.2}$$

When transforming compliance tensor components to their corresponding Voigt matrix components and vice versa, prefactors have to be used [26]. The prefactors are listed in Eqs. 2.2. The transformation between tensor and Voigt notation for all stiffness tensors can be performed without considering about prefactors. The indices of the Voigt matrix or tensor are directly replaced according to Tab. 2.1.

2.3 Systems of reference

2.3.1 Transformation matrices

Physical properties are described through tensors. The tensor components depend, in general, on the coordinate system. When tensors are used to qualify physical properties it is indispensable to define coordinate systems. Within this thesis four coordinate systems, commonly used in literature [26, 38, 57], will be applied.

- The sample system (S) with its $\vec{S}_1$ and $\vec{S}_2$ axis in-plane and the $\vec{S}_3$ normal to the sample surface.
- The laboratory coordinate system (L) with its $\vec{L}_3$ axis parallel to the scattering vector.
- The intermediate coordinate system (Ω) with its $\vec{\Omega}_3$ axis parallel to the [hkl] direction of a plane (hkl) [1].
- The crystal coordinate system (C) with its $\vec{C}_1$, $\vec{C}_2$ and $\vec{C}_3$ axis parallel to the [100] directions of the crystal system.

The Euler angles can be used to describe the rotational position of a coordinate system in respect to the sample coordinate system. Fig. 2.1 shows the three rotations expressed through Eqs. 2.3, 2.4 and 2.5. Within this thesis Euler angles will be used

[1] In general, the normal vector on a (hkl) plane has got the covariant indices hkl [58]. However, in respect to a cubic crystal system (orthonormal coordinate system), where covariant and contravariant indices are equal, the normal to a (hkl) plane can directly be expressed as [hkl].

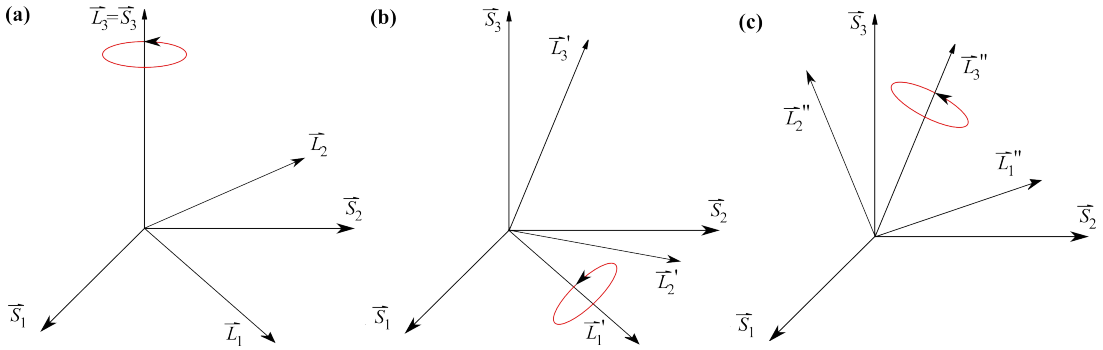

Figure 2.1: The three consecutive rotations of a coordinate system according to Bunge notation. First the coordinate system is rotated around the $\vec{S}_3$ axis which is parallel to $\vec{L}_3$ (a). The new coordinate axes $\vec{L'}_1$,$\vec{L'}_2$ and $\vec{L'}_3$ are primed (b). Then the primed coordinate system (b) is rotated around the $\vec{L'}_1$ axis. Finally, the double primed coordinate system (c) is rotated around the $\vec{L''}_3$ (c).

in Bunge notation. In Bunge notation the coordinate system is first rotated around the $\vec{S}_3$ axis which is parallel to $\vec{L}_3$ (Fig. 2.1a). The new coordinate axes $\vec{L'}_1$,$\vec{L'}_2$ and $\vec{L'}_3$ are primed (Fig. 2.1b). Then the primed coordinate system is rotated around the $\vec{L'}_1$ axis (Fig. 2.1b). Finally, the double primed coordinate system is rotated around the $\vec{L''}_3$ (Fig. 2.1c).

$$a_{ij}^{\Phi_1} = \begin{pmatrix} \cos\Phi_1 & \sin\Phi_1 & 0 \\ -\sin\Phi_1 & \cos\Phi_1 & 0 \\ 0 & 0 & 1 \end{pmatrix} \tag{2.3}$$

$$a_{ij}^{\Phi} = \begin{pmatrix} 1 & 0 & 0 \\ 0 & \cos\Phi & \sin\Phi \\ 0 & -\sin\Phi & \cos\Phi \end{pmatrix} \tag{2.4}$$

$$a_{ij}^{\Phi_2} = \begin{pmatrix} \cos\Phi_2 & \sin\Phi_2 & 0 \\ -\sin\Phi_2 & \cos\Phi_2 & 0 \\ 0 & 0 & 1 \end{pmatrix} \tag{2.5}$$

Moreover, tensor components are transformed between the S, L, Ω and C coordinate system using the matrices (Eqs. 2.6, 2.7, 2.8 and 2.9). The ϕ-matrix (Eq. 2.6) is equivalent to the Φ_1-matrix expressed in Eq. 2.3.

$$a_{ij}^{\phi} = \begin{pmatrix} \cos\phi & \sin\phi & 0 \\ -\sin\phi & \cos\phi & 0 \\ 0 & 0 & 1 \end{pmatrix} \tag{2.6}$$

The ψ-matrix performs a rotation around the $\vec{L}_2$ axis. The ϕ and ψ-matrices are defined in [26].

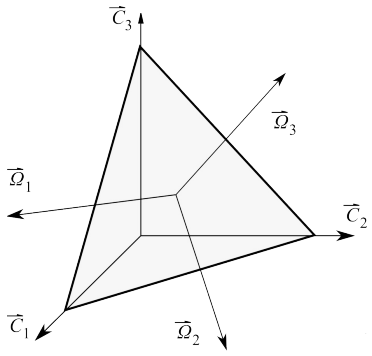

Figure 2.2: The figure shows the crystal coordinate system C, the intermediate coordinate system Ω and a (111) crystallographic plane as an example for an arbitrary plane (hkl). The $\vec{\Omega}_3$ axis of the Ω coordinate system is always normal to the plane (hkl). The $\vec{\Omega}_1$ and $\vec{\Omega}_2$ axis are situated in-plane of the (hkl) plane.

$$a_{ij}^{\psi} = \begin{pmatrix} \cos\psi & 0 & -\sin\psi \\ 0 & 1 & 0 \\ \sin\psi & 0 & \cos\psi \end{pmatrix} \tag{2.7}$$

The scattering vector $\vec{g}$ is always parallel to the $\vec{L}_3$ axis of the L system. The crystallographic planes normal to $\vec{g}$ have one degree of freedom left around $\vec{g}$. This makes it necessary to define a transformation matrix which rotates the tensor components around $\vec{g}$. The matrix used to transform tensor components around the scattering vector $\vec{g}$ is the λ matrix [61] (Eq. 2.8)

$$a_{ij}^{\lambda} = \begin{pmatrix} \cos\lambda & \sin\lambda & 0 \\ -\sin\lambda & \cos\lambda & 0 \\ 0 & 0 & 1 \end{pmatrix} \tag{2.8}$$

The matrix which transforms tensor components from the C system to the intermediate system Ω (Fig. 2.2) will be called Ω matrix (Eq. 2.9). This matrix can be described purely through the miller indices hkl describing the (hkl) plane or the $\langle hkl \rangle$ direction which is normal to the (hkl) plane (in cubic crystal systems).

$$a_{ij}^{\Omega} = \begin{pmatrix} \frac{hl}{\sqrt{h^2+k^2}\sqrt{h^2+k^2+l^2}} & \frac{kl}{\sqrt{h^2+k^2}\sqrt{h^2+k^2+l^2}} & \frac{-k^2+h^2}{\sqrt{h^2+k^2}\sqrt{h^2+k^2+l^2}} \\ \frac{-k}{\sqrt{h^2+k^2}} & \frac{h}{\sqrt{h^2+k^2}} & 0 \\ \frac{h}{\sqrt{h^2+k^2+l^2}} & \frac{k}{\sqrt{h^2+k^2+l^2}} & \frac{l}{\sqrt{h^2+k^2+l^2}} \end{pmatrix} \tag{2.9}$$

The validity of Eq. 2.9 can be proofed considering following example. The tensor components $\left(\frac{1}{\sqrt{3}}, \frac{1}{\sqrt{3}}, \frac{1}{\sqrt{3}}\right)$ of a rank 1 tensor are transformed to (001) for a (111) plane. Thinking in terms of crystallographic directions rather than in terms of tensor components one can imagine that for a Ω matrix created for a (111) plane the $\langle 111 \rangle$ direction in the C system is a $\langle 001 \rangle$ direction in the Ω system.

2.3.2 Tensor transformations

The connection between the transformation matrices can be found in [62]. In comparison to [62], the transformation matrices in this thesis are defined to transform tensor components directly, rather than the axes of the coordinate systems.

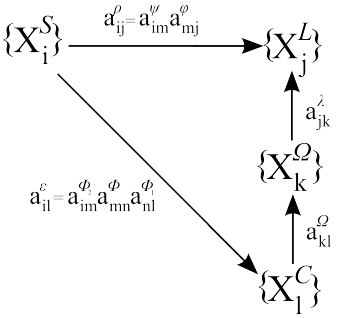

Figure 2.3: The picture shows the relation between the tensor components of a rank one tensor $\{X_i\}$ in respect to all used coordinate systems. The transformation of tensor components between the S and L system is performed with the matrix a^{ρ}_{ij}. The matrices a^{Ω}_{ij} and a^{λ}_{ij} transform the tensor components from C to Ω and from Ω to L, respectively. The tensor transformation from S to C can directly be performed using the Euler angle matrix a^{ϵ}_{ij}. The tensor equation $a^{\gamma}_{ik}a^{\rho}_{kj} = a^{\epsilon}_{ij}$ can be used to find the corresponding Euler angles Φ_1, Φ and Φ_2 for a definite parameter set $(\phi, \psi, \lambda, hkl)$. A similar picture can be found in [62].

The transformation of tensor components from $S \rightarrow L$ is performed using Eqs. 2.6 and 2.7, *i.e.*

$$\left\{X_i^L\right\} = a^{\psi}_{ij}a^{\phi}_{jk}\left\{X_k^S\right\} \tag{2.10}$$

According to [62] the tensor components can be transformed from $C \rightarrow \Omega$ using

$$\left\{X_i^{\Omega}\right\} = a^{\Omega}_{ij}\left\{X_j^C\right\} \tag{2.11}$$

The transformation rule between $\Omega \rightarrow L$ can be written as

$$\left\{X_i^L\right\} = a^{\lambda}_{ij}\left\{X_j^{\Omega}\right\} \tag{2.12}$$

The direct tensor component transformation $S \rightarrow C$ is

$$\left\{X_i^C\right\} = a_{ij}\left\{X_j^S\right\} \tag{2.13}$$

where a_{ij} can be expressed as

$$\begin{aligned} a_{ij} &= (a^{\Omega})^{-1}_{im}(a^{\lambda})^{-1}_{ml}a^{\psi}_{lk}a^{\phi}_{kj} && (2.14)\\ &= (a^{\Omega})^{-1}_{il}(a^{\lambda})^{-1}_{lk}a^{\rho}_{kj} && (2.15)\\ &= a^{\gamma}_{ik}a^{\rho}_{kj} && (2.16) \end{aligned}$$

The transformation from $S \rightarrow C$ can also be performed using Euler angles, *i.e.*

$$a_{il}^{\epsilon} = a_{il}^{\Phi_2} a_{lk}^{\Phi} a_{kj}^{\Phi_1} \tag{2.17}$$

Eqs. 2.11 and 2.12 can be joined to

$$\left\{X_i^L\right\} = a_{ij}^{\lambda} a_{jk}^{\Omega} \left\{X_k^C\right\} = \left(a^{\gamma}\right)_{ik}^{-1} \left\{X_k^C\right\} \tag{2.18}$$

2.3.3 The fundamental equations of stress analysis

X-ray analysis is a tool to determine the lattice spacing of crystal planes in direction of the scattering vector $\vec{g}$. In Sec. 2.3.1 the scattering vector $\vec{g}$ was assigned with the $\vec{L}_3$ axis of the L system. The mathematical equation relating the strain tensor components of the S coordinate system with the strain tensor components of the L coordinate system [26], is therefore

$$\left\{\epsilon_{ij}^L\right\}_{\psi}^{hkl} = a_{im}^{\rho} a_{jn}^{\rho} \left\{\epsilon_{mn}^S\right\}^{hkl} \tag{2.19}$$

The X-ray strain $\left\{\epsilon_{ij}^L\right\}_{\psi}^{hkl}$ can be expressed as a function of the strain tensor components in respect to the sample coordinate system $\left\{\epsilon_{mn}^S\right\}^{hkl}$ [26] applying Eq. 2.20 to Eq. 2.19

$$a_{ij}^{\rho} = \begin{pmatrix} \cos\phi\cos\psi & \sin\phi\cos\psi & -\sin\psi \\ -\sin\phi & \cos\phi & 0 \\ \cos\phi\sin\psi & \sin\phi\sin\psi & \cos\psi \end{pmatrix} \tag{2.20}$$

which leads to

$$\begin{aligned} \left\{\epsilon_{33}^L\right\}_{\psi}^{hkl} = \left\{\epsilon_{11}^S\right\}^{hkl} \cos^2\phi \sin^2\psi + \left\{\epsilon_{12}^S\right\}^{hkl} \sin 2\phi \sin^2\psi + \left\{\epsilon_{13}^S\right\}^{hkl} \cos\phi \sin 2\psi \\ + \left\{\epsilon_{22}^S\right\}^{hkl} \sin^2\phi \sin^2\psi + \left\{\epsilon_{23}^S\right\}^{hkl} \sin\phi \sin 2\psi \\ + \left\{\epsilon_{33}^S\right\}^{hkl} \cos^2\psi \end{aligned} \tag{2.21}$$

The boundary condition of the strain state can simplify Eq. 2.21 even further. If all shear strains are zero, *i.e.*

$$\begin{aligned} \left\{\epsilon_{12}^S\right\}^{hkl} &= \left\{\epsilon_{21}^S\right\}^{hkl} = 0 \\ \left\{\epsilon_{13}^S\right\}^{hkl} &= \left\{\epsilon_{31}^S\right\}^{hkl} = 0 \\ \left\{\epsilon_{23}^S\right\}^{hkl} &= \left\{\epsilon_{32}^S\right\}^{hkl} = 0 \end{aligned} \tag{2.22}$$

Eq. 2.21 is simplified to

$$\left\{\epsilon_{33}^{L}\right\}_{\psi}^{hkl} = \left\{\epsilon_{11}^{S}\right\}^{hkl}\cos^2\phi\sin^2\psi + \left\{\epsilon_{22}^{S}\right\}^{hkl}\sin^2\phi\sin^2\psi + \left\{\epsilon_{33}^{S}\right\}^{hkl}(1-\sin^2\psi) \quad (2.23)$$

If $\left\{\epsilon_{11}^{S}\right\}^{hkl} = \left\{\epsilon_{22}^{S}\right\}^{hkl}$ Eq. 2.23 leads to

$$\left\{\epsilon_{33}^{L}\right\}_{\psi}^{hkl} = (\left\{\epsilon_{11}^{S}\right\}^{hkl} - \left\{\epsilon_{33}^{S}\right\}^{hkl})\sin^2\psi + \left\{\epsilon_{33}^{S}\right\}^{hkl} \quad (2.24)$$

Eq. 2.24 shows the linear correlation between $\left\{\epsilon_{33}^{L}\right\}_{\psi}^{hkl}$ and $\sin^2\psi$. In [26] strain distributions of $\left\{\epsilon_{33}^{L}\right\}_{\psi}^{hkl}$ for different boundary conditions are discussed. However, within this thesis shear strains and shear stresses are always assumed to be zero and ψ-splitting or oscillatory [26, 63] in $\left\{\epsilon_{33}^{L}\right\}_{\psi}^{hkl}$ due to complex stress-strain states or plastic anisotropy will not be considered.

2.3.4 The stress-strain relation

The correlation between stress and strain is described through Hook's law. Generally speaking, Hook's law can be expressed in tensor notation

$$\{\sigma_{ij}\} = \{C_{ijkl}\}\{\epsilon_{kl}\} \quad (2.25)$$

$$\{\epsilon_{ij}\} = \{S_{ijkl}\}\{\sigma_{kl}\} \quad (2.26)$$

where $\{C_{ijkl}\}$ and $\{S_{ijkl}\}$ are the stiffness and compliance tensors, respectively. Tensors are always defined in respect to a coordinate system. In X-ray diffraction it is common to define the tensor components in respect to the laboratory system L (Eq. 2.27)

$$\left\{\epsilon_{ij}^{L}\right\}_{\psi}^{hkl} = \left\{S_{ijkl}^{L}\right\}_{\psi}^{hkl}\left\{\sigma_{kl}^{L}\right\} \quad (2.27)$$

Due to the fact that the boundary conditions for the stress state are defined in respect to the sample coordinate system S, $\left\{\sigma_{kl}^{L}\right\}$ is expressed as a function of $\left\{\sigma_{mn}^{S}\right\}$. Applying the tensor transformation rule (Eq. 2.1) to Eq. 2.27 leads to

$$\left\{\epsilon_{ij}^{L}\right\}_{\psi}^{hkl} = \left\{S_{ijkl}^{L}\right\}_{\psi}^{hkl} a_{km}a_{ln}\left\{\sigma_{mn}^{S}\right\} \quad (2.28)$$

or if the scattering vector sensitivity in $\vec{L}_3$ direction is used

$$\left\{\epsilon_{33}^{L}\right\}_{\psi}^{hkl} = \left\{S_{33kl}^{L}\right\}_{\psi}^{hkl} a_{km}a_{ln}\left\{\sigma_{mn}^{S}\right\} \quad (2.29)$$

Eq. 2.29 is the general notation which correlates the X-ray strain $\left\{\epsilon_{33}^{L}\right\}_{\psi}^{hkl}$ in the laboratory coordinate system L to the macroscopic stress $\left\{\sigma_{mn}^{S}\right\}$ in the sample coordinate system S. The compliance tensor is always expressed in respect to the L system.

2.4 Orientation distribution function

The mathematical description of textured materials demands the usage of an orientation distribution function (ODF) [64]. The ODF describes the probability to find a grain at the orientation (Φ_1, Φ, Φ_2). The three Euler angles Φ_1, Φ and Φ_2 are the rotation angles used to rotate the S system into the C system. There are many different conventions used in literature how to rotate the S system to the C system. The Bunge and Roe conventions are the most established ones. In this thesis only the Bunge convention will be used. The Bunge notation performs a consecutive rotation around the axes $\vec{L}_3$, $\vec{L'}_1$ and L''_3 in mathematical positive manner (see sec 2.3.1).

Figs. 2.4 and 2.5 show a Φ_1 cross section of the ODF space for a (111) fiber textured material with $\psi_{\mathrm{FWHM}} = 10^\circ$ and 10% ISO with cubic crystal symmetry. Fig. 2.4 shows the reduced ODF space of Fig. 2.5. In order to analyse experimental data and simulate various fibre textures, a software Labotex [65] was used within this thesis. Although LaboTex is not able to save the ODF in triclinic sample symmetry for non triclinic crystal symmetries, it is possible to perform a work around. First, the ODF for any crystal symmetry is produced and exported as SOR file. Then the SOR file is opened in a text editor and the structure code value is changed to 1 (triclinic sample symmetry). The manipulated SOR file is saved and can be imported into LabTex. LaboTex performs all symmetry operations automatically and the ODF can be saved in Bunge notation. This procedure has got the advantage that no symmetry operations have to be programmed into the software. The disadvantage is the increasing effort of building the correct ODF.

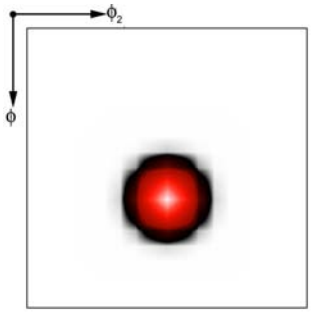

Figure 2.4: The figure shows a representative Φ_1 cross section of the reduced ODF space for a (111) fiber textured materials with $\psi_{\mathrm{FWHM}} = 10^\circ$ and 10% ISO with cubic crystal symmetry. The ODF was rendered to improve image quality. The ODF was produced with software LaboTEX [65].

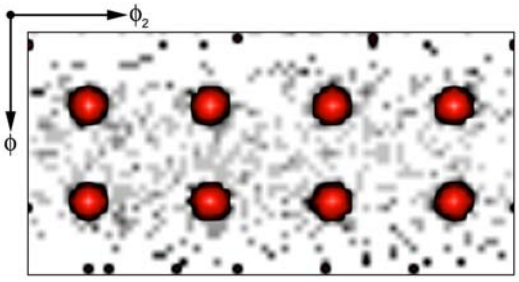

Figure 2.5: The figure shows a representative Φ_1 cross section of the full ODF space for a (111) fiber textured materials with $\psi_{\mathrm{FWHM}} = 10^\circ$ and 10% ISO with cubic crystal symmetry. The ODF was rendered to improve image quality. In comparison to Fig. 2.4 it is evident that there are two symmetry elements availaible. The first is a four fold symmetry along the Φ_2-axis. The second symmetry element is a mirror operation at $\Phi = 90^\circ$. The ODF should always be saved in triclinic sample symmetry. This is the most general case and it is not necessary to program symmetry operations in the simulation software used to calculate the compliance tensors according the Reuss grain interaction model. The software is therefore more flexible and can be used in future versions to calculate compliance tensors for any crystal and/or sample symmetry. The ODF was produced with software LaboTEX [65].

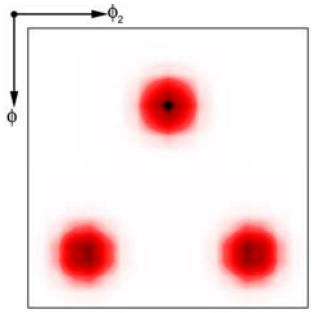

Figure 2.6: The figure shows a representative Φ_1 cross section of the reduced ODF space for a (311) fiber textured materials with $\psi_{\mathrm{FWHM}} = 10^\circ$ and 10% ISO with cubic crystal symmetry. The ODF was rendered to improve image quality. The ODF was produced with software LaboTEX [65]. The number of fibers per reduced ODF space is equal to the number of possible permutations of absolute values (*hkl*).

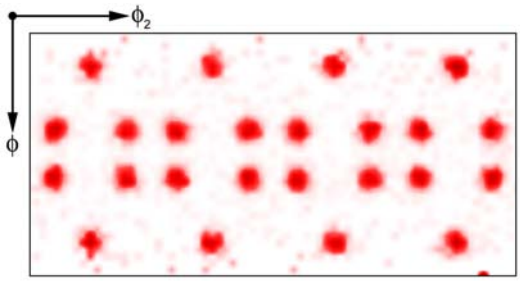

Figure 2.7: The figure shows a representative Φ_1 cross section of the full ODF space for a (311) fiber textured materials with $\psi_{\mathrm{FWHM}} = 10^\circ$ and 10% ISO with cubic crystal symmetry. The ODF was rendered to improve image quality. In comparison to Fig. 2.6 it is evident that there are two symmetry elements availaible. The first is a four fold symmetry along the Φ_2-axis. The second symmetry element is a mirror operation at $\Phi = 90^\circ$. The ODF should always be saved in triclinic sample symmetry. This is the most general case and it is not necessary to program symmetry operations in the simulation software used to calculate the compliance tensors according the Reuss grain interaction model. The software is therefore more flexible and can be used in future versions to calculate compliance tensors for any crystal and/or sample symmetry. The ODF was produced with software LaboTEX [65].

2.5 X-ray grain interaction models

The single crystal elastic constants (SECs) and the unstressed lattice parameter a_0 used within this thesis for simulations are listed in Tab. 2.2

Table 2.2: List of single crystal elastic constants and the unstressed lattice parameters used for the simulations. The single crystal elastic constants are written in tensor compliance form. The unstressed lattice parameters for Cu,CrN and TiN can be found in [8, 66, 67].

Material	S_{1111}	S_{1122}	S_{1212}		ZAR	a_0
	$(10^{-11}Pa^{-1})$	$(10^{-11}Pa^{-1})$	$(10^{-11}Pa^{-1})$			(Å)
Cu	1.500	-0.630	0.332	[24]	3.203	3.6150[66]
CrN	0.185	-0.009	0.284	[68]	0.342	4.1650[67]
TiN	0.180	-0.038	0.154	[69]	0.710	4.2430[8]

2.5.1 The Reuss Model

With diffraction techniques strain can only be measured in the direction of the scattering vector $\vec{g}$. The measured strain $\left\{\epsilon_{33}^{L}\right\}_{\psi}^{hkl}$ represents an average strain of all diffracting crystallites along the diffraction vector $\vec{g}$. All diffracting crystallographic lattice planes (hkl) which are situated normal to the scattering vector contribute to this average strain component expressed through $\left\{\epsilon_{33}^{L}\right\}_{\psi}^{hkl}$. The only degree of freedom for these crystallographic lattice planes is the rotation around $\vec{g}$. This degree of freedom is characterized by the rotation angle λ. The mathematical expression for $\left\{\epsilon_{33}^{L}\right\}_{\psi}^{\mathrm{R},hkl}$ according to [61] is

$$\left\{\epsilon_{33}^{L}\right\}_{\psi}^{\mathrm{R},hkl} = \frac{\int_0^{2\pi} \left\{\epsilon_{33}^{L}\right\}_{\psi}^{hkl} (g_{\psi\phi}(\lambda)) f(g_{\psi\phi}(\lambda)) d\lambda}{\int_0^{2\pi} f(g_{\psi\phi}(\lambda)) d\lambda} \tag{2.30}$$

where $\left\{\epsilon_{33}^{L}\right\}_{\psi}^{hkl}$ is the strain parallel to $\vec{g}$ in the grain with the crystallite orientation $g_{\psi\phi}(\lambda)$. The function f is the ODF. It is used as weight function in Eq. 2.30. Hook's law in the L system is

$$\left\{\epsilon_{ij}^{L}\right\}_{\psi}^{\mathrm{R},hkl} = \left\{S_{ijkl}^{L}\right\}_{\psi}^{\mathrm{R},hkl} \left\{\sigma_{kl}^{L}\right\}_{\psi} \tag{2.31}$$

or applying the rules of the scattering vector sensitivity to Eq. 2.31

$$\left\{\epsilon_{33}^{L}\right\}_{\psi}^{\mathrm{R},hkl} = \left\{S_{33kl}^{L}\right\}_{\psi}^{\mathrm{R},hkl} \left\{\sigma_{kl}^{L}\right\}_{\psi} \tag{2.32}$$

According to [61] $\left\{S_{33ij}^{L}\right\}_{\psi}^{\mathrm{R},hkl}$ can then be calculated using Eq. 2.33

$$\left\{S_{33ij}^{L}\right\}_{\psi}^{\mathrm{R},hkl} = \frac{\int_0^{2\pi} \left\{S_{33ij}^{L}\right\}_{\psi}^{hkl} (\lambda) f(g_{\psi\phi}(\lambda)) d\lambda}{\int_0^{2\pi} f(g_{\psi\phi}(\lambda)) d\lambda} \tag{2.33}$$

The compliance components $\left\{S^L_{33ij}\right\}^{hkl}_{\psi}$ of the L system are related to the compliance components $\{S^C_{klmn}\}$ of the C coordinate system using the law of tensor transformation (Eq. 2.1).

$$\{S^L_{33ij}\}^{\mathrm{R},hkl}_{\psi} = \frac{\int_0^{2\pi} (a^\gamma)^{-1}_{3k}(a^\gamma)^{-1}_{3l}(a^\gamma)^{-1}_{im}(a^\gamma)^{-1}_{jn}\{S^C_{klmn}\} f(g_{\psi\phi}(\lambda))d\lambda}{\int_0^{2\pi} f(g_{\psi\phi}(\lambda))d\lambda} \tag{2.34}$$

Eq. 2.34 can then be used to calculate the X-ray elastic compliance tensor components $\left\{S^L_{33ij}\right\}^{\mathrm{R},hkl}_{\psi}$ for the L system. The integration of Eq. 2.34 can be performed numerically. However, the determination of the ODF values as a function of the integration parameter λ is not that trivial. The procedure of determining the correct ODF values can be found in [62].

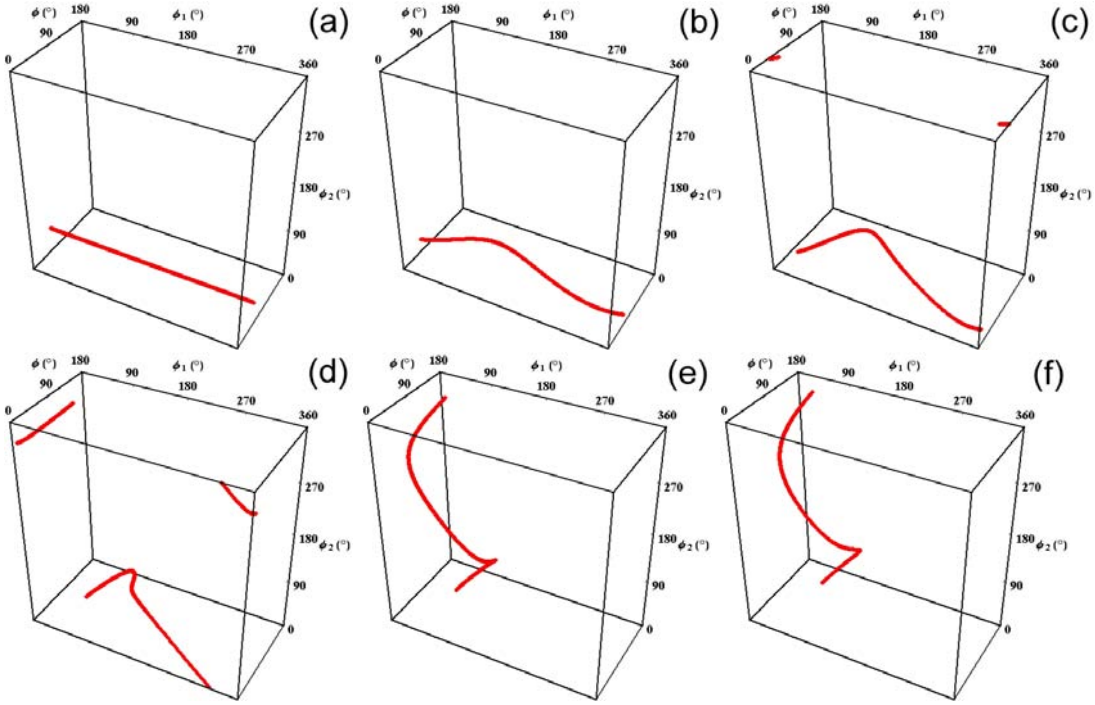

Figure 2.8: The six figures show the λ-trails for a (111) reflex in the Reuss model at $\psi = 0°$ (a),18° (b),36° (c),54° (d),72° (e) and 90° (f), respectively. At $\psi = 0°$ (a) the λ-trail is a straight line through the ODF space due to the laboratory system is not tilted in respect to the sample coordinate system, $\vec{L}_3$ is parallel to $\vec{S}_3$ and λ is equal to the Euler angle Φ_1. The other two Euler angles are constant over the whole λ range. Although the sample symmetry is axial for a fiber textured sample, the ODF is always saved with triclinic sample symmetry (see Sec. 2.4). If the whole ODF space is saved, the appropriate ODF values can directly be evaluated without concerning about the ODF symmetries in the software. At approximately $\psi = 36°$ (c) the λ-trail appears at $\Phi_2 = 360°$ because the Φ_2 angle is smaller than 0° and has to be taken modulo 360°.

2.5.2 The Voigt Model

In 1910 the physicist Voigt was the first scientist who developed a grain interaction model for polycrystals [31]. He assumed the strain tensor to be equal in all grains. According to [61] the averaged stiffness tensor components can be calculated using Eq. 2.35

$$\left\{C_{ijkl}^{S}\right\}^{\mathrm{V}} = \frac{\int \left\{C_{ijkl}^{S}\right\} f(g) dg}{\int f(g) dg} \tag{2.35}$$

where $\left\{C_{ijkl}^{S}\right\}^{\mathrm{V}}$ is the averaged compliance tensor in the S system. The $\left\{C_{ijkl}^{S}\right\}$ are the stiffness SECs in respect to the sample coordinate system S [61] and $f(g)$ is the ODF value at position g in ODF space. The Voigt model is an average over the whole grain agglomerate. In comparison to the calculation of the Reuss X-ray compliance tensor (see Sec. 2.5.1), the Voigt X-ray compliance tensor is not scattering vector sensitive. In fact, the calculated Voigt X-ray compliance tensor is equal to the Voigt mechanical compliance tensor. The rule of tensor transformation (Eq. 2.1) can be used to transform the Voigt X-ray compliance tensor components from the S system to the L system. Only in the isotropic case, the Voigt X-ray compliance tensor components would be equal towards all coordinate systems and tensor transformation would not be necessary. The averaged X-ray stiffness tensor in Eq 2.35 can be transformed to the corresponding compliance tensor, applying Voigt notation (see Sec. 2.2), *i.e.*

$$\left\{S_{ijkl}^{S}\right\}^{\mathrm{V}} = (\left\{C_{ijkl}^{S}\right\}^{\mathrm{V}})^{-1} \tag{2.36}$$

2.5.3 The Hill Model

In 1952, Hill [33] proposed an arithmetic mean of the Reuss and Voigt compliance tensors to describe the elastic behaviour of materials. When the Reuss X-ray compliance tensor is calculated according to [61] the tensor components are already expressed in respect to the L system. However, the Voigt X-ray compliance tensor components are calculated in respect to the S system and have to be transformed to the L system to perform the Hill average

$$\left\{S_{ijkl}^{L}\right\}_{\psi}^{\mathrm{H},hkl} = x \left\{S_{ijkl}^{L}\right\}_{\psi}^{\mathrm{R},hkl} + (1-x) \left\{S_{ijkl}^{L}\right\}_{\psi}^{\mathrm{V}} \tag{2.37}$$

where x is the Hill factor. It has to be emphasized that there is a whole set of Hill compliance tensors, one tensor for each (ϕ, ψ) position. This is a result of the fact, that a Reuss compliance tensor has to be calculated for each (ϕ, ψ) position. The Voigt compliance tensor part in Eq. 2.37 is calculated in respect to the sample coordinate system S (Eq. 2.35) but can easily be transformed to the L system at position (ϕ, ψ) using law of tensor transformation (Eq. 2.1). Therefore, calculation of Hill X-ray elastic strains can be simplified by calculating the Voigt compliance tensor once, and perform the tensor transformation to L for each angular position ψ. Of course, the X-ray Reuss compliance tensor still has to be calculated for each angular position ψ.

2.6 Calculation of X-ray elastic constants

A compliance tensor fully describes the elastic behaviour of a grain agglomerate. However, X-ray compliance tensors normally depend on information parallel to the scattering vector $\vec{g}$. For most grain interaction models, this dependence on $\vec{g}$ results in a full set of compliance tensors for each angle combination (ϕ, ψ). Moreover, a simplified stress state, as well as high sample symmetry of the texture, can dramatically reduce the amount of compliances in Eq. 2.29. In the case of thin films, an equibiaxial stress state and axial sample symmetry can be assumed. According to these boundary conditions Eq. 2.29 can be simplified to [57, 70]

$$\begin{aligned}\left\{\epsilon_{33}^{L}\right\}_{\psi}^{hkl} = \sigma((\left\{S_{3311}^{L}\right\}_{\psi}^{hkl} + \left\{S_{3322}^{L}\right\}_{\psi}^{hkl}) + (\left\{S_{3333}^{L}\right\}_{\psi}^{hkl} - \left\{S_{3311}^{L}\right\}_{\psi}^{hkl}) \sin^2\psi \\ + \left\{S_{3313}^{L}\right\}_{\psi}^{hkl} \sin 2\psi)\end{aligned} \tag{2.38}$$

In comparison to [61] $\left\{\epsilon_{33}^{L}\right\}_{\psi}^{hkl}$ is not shortened to

$$\left\{\epsilon_{33}^{L}\right\}_{\psi}^{hkl} = \sigma(2\left\{s_1\right\}^{hkl} + \frac{1}{2}\left\{s_2\right\}^{hkl} \sin^2\psi) \tag{2.39}$$

which only holds for isotropic materials. Eq. 2.38 is analysed at angular positions $\psi = 0°$ and $\psi = 90°$.

- At $\psi = 0°$, $\left\{S_{3311}^{L}\right\}_{\psi=0°}^{hkl} = \left\{S_{3322}^{L}\right\}_{\psi=0°}^{hkl}$ and Eq. 2.38 can be written as

$$\begin{aligned}\left\{\epsilon_{33}^{L}\right\}_{\psi=0°}^{hkl} = \sigma(\left\{S_{3311}^{L}\right\}_{\psi=0°}^{hkl} + \left\{S_{3322}^{L}\right\}_{\psi=0°}^{hkl}) = 2\sigma\left\{S_{3311}^{L}\right\}_{\psi=0°}^{hkl} \\ = 2\sigma\left\{s_1\right\}_{\psi=0°}^{hkl}\end{aligned} \tag{2.40}$$

  If the intersection $\left\{\epsilon_{33}^{L}\right\}_{\psi=0°}^{hkl}$ of the $\left\{\epsilon_{33}^{L}\right\}_{\psi}^{hkl} - \sin^2\psi$ plot and the equibiaxial stress σ (see Sec. 3.3) are known, $\left\{S_{3311}^{L}\right\}_{\psi=0°}^{hkl}$ can be calculated.
  Moreover, the slope of $\left\{\epsilon_{33}^{L}\right\}_{\psi}^{hkl} - \sin^2\psi$ at $\psi = 0°$ can be determined. The slope is the derivative $\left\{\epsilon_{33}^{L}\right\}_{\psi}^{hkl}$ in respect to $\sin^2\psi$, *i.e.*

$$\left\{\frac{\partial\left\{\epsilon_{33}^{L}\right\}_{\psi}^{hkl}}{\partial \sin^2\psi}\right\}_{\psi=0°}^{hkl} = \sigma(\left\{S_{3333}^{L}\right\}_{\psi=0°}^{hkl} - \left\{S_{3311}^{L}\right\}_{\psi=0°}^{hkl}) \tag{2.41}$$

  Eq. 2.41 can be calculated using following procedure. The substitution $\sin^2\psi \rightarrow u$ and $\sin 2\psi \rightarrow 2\sqrt{u}\sqrt{1-u}$ is performed in Eq. 2.38. The derivative with respect to u is

$$\left\{ \frac{\partial \left\{\epsilon_{33}^{L}\right\}_{u}^{hkl}}{\partial u} \right\}_{u=0}^{hkl} = \sigma(\left\{S_{3333}^{L}\right\}_{u=0}^{hkl} - \left\{S_{3311}^{L}\right\}_{u=0}^{hkl} + \frac{\left\{S_{3313}^{L}\right\}_{u=0}^{hkl}(1-2u)}{\sqrt{u-u^2}}) \quad (2.42)$$

The third term in Eq. 2.42 is an undefined expression $0/0$ for $u = 0$ because of $\left\{S_{3313}^{L}\right\}_{u=0}^{hkl} = 0$ (The compliance tensor has got hexagonal symmetry in respect to the S coordinate system [25], *i.e.* $\left\{S_{3313}^{L}\right\}_{u=0}^{hkl} = \left\{S_{3313}^{S}\right\}^{hkl} = 0$). Using l'Hôpital's rule [71], it can be shown that the third term in Eq. 2.42 is zero for $u = 0$.
Substitution of $\left\{S_{3311}^{L}\right\}_{\psi=0^\circ}^{hkl}$ from Eq. 2.40 in Eq. 2.41 allows the determination of $\left\{S_{3333}^{L}\right\}_{\psi=0^\circ}^{hkl}$ if the equibiaxial stress σ (see Sec. 3.3) is known. The *out-of-plane* X-ray elastic modulus and the Poisson's ratio $\left\{\nu_{3311}^{L}\right\}_{\psi=0^\circ}^{hkl}$ are

$$\left\{E_{3333}^{L}\right\}_{\psi=0^\circ}^{hkl} = \frac{1}{\left\{S_{3333}^{L}\right\}_{\psi=0^\circ}^{hkl}} \quad (2.43)$$

$$\left\{\nu_{3311}^{L}\right\}_{\psi=0^\circ}^{hkl} = -\frac{\left\{S_{3311}^{L}\right\}_{\psi=0^\circ}^{hkl}}{\left\{S_{3333}^{L}\right\}_{\psi=0^\circ}^{hkl}} \quad (2.44)$$

- At $\psi = 90^\circ$ Eq. 2.38 can be expressed as

$$\left\{\epsilon_{33}^{L}\right\}_{\psi=90^\circ}^{hkl} = \sigma(\left\{S_{3322}^{L}\right\}_{\psi=90^\circ}^{hkl} + \left\{S_{3333}^{L}\right\}_{\psi=90^\circ}^{hkl}) \quad (2.45)$$

Eq. 2.45 has got two unknowns. Therefore it is not possible to determine the compliance components separately, in comparison to Eqs. 2.40 and 2.41. However, the sum of $\left\{S_{3322}^{L}\right\}_{\psi=90^\circ}^{hkl}$ and $\left\{S_{3333}^{L}\right\}_{\psi=90^\circ}^{hkl}$ in Eq. 2.45 can easily be determined. The value $\left\{S_{3322}^{L}\right\}_{\psi=90^\circ}^{hkl} + \left\{S_{3333}^{L}\right\}_{\psi=90^\circ}^{hkl}$ will be used to determine the *mechanical in-plane* biaxial modulus (see Sec. 2.13).

Most X-ray grain interaction models significantly differ to mechanical grain interaction models in case of tensor calculation. A mechanical compliance tensor is always calculated once, in respect to any coordinate system[2]. Then its tensor components can directly be transformed according to the law of tensor transformation (Eq. 2.1). This also holds for the Voigt X-ray compliance tensor. However, according to many other grain interaction models (*e.g.* Reuss, Hill *etc.*), there is a whole set of X-ray compliance tensors, one for each (ϕ, ψ) position[3]. This means that

$$\begin{aligned} \left\{S_{3322}^{L}\right\}_{\psi=90^\circ}^{hkl} &\neq \left\{S_{1122}^{L}\right\}_{\psi=0^\circ}^{hkl} \\ \left\{S_{3333}^{L}\right\}_{\psi=90^\circ}^{hkl} &\neq \left\{S_{1111}^{L}\right\}_{\psi=0^\circ}^{hkl} \end{aligned} \quad (2.46)$$

[2] In most cases this is the sample coordinate system
[3] In the case of fiber textured materials, only for each ψ position

for nearly all X-ray grain interaction models.

2.7 Mechanical grain interaction models

In comparison to the X-ray elastic compliance tensors the mechanical elastic compliance tensors are always calculated applying the grain interaction model to the whole grain agglomerate in respect to the sample coordinate system [72]. The physical considerations for Reuss and Voigt still hold. The compliance tensor components in respect to any other coordinate system can he calculated using law of tensor transformation (Eq. 2.1).

2.7.1 The Reuss model

The mechanical Reuss compliance tensor is calculated applying the Reuss grain interaction model to all grains, *i.e.* the integration is performed over the whole ODF space. In comparison to the X-ray Reuss compliance tensor it is not necessary to find the λ-trail in ODF space. This dramatically simplifies the calculation of the mechanical Reuss compliance tensor. The tensor can be calculated using Eq. 2.47

$$\left\{S^S_{ijkl}\right\}^{\mathrm{R,M}} = \frac{\int_{\Phi_1=0}^{2\pi}\int_{\Phi=0}^{\pi}\int_{\Phi_2=0}^{2\pi} f(\Phi_1,\Phi,\Phi_2)a^{\epsilon}_{im}a^{\epsilon}_{jn}a^{\epsilon}_{ko}a^{\epsilon}_{lp}\left\{S^C_{mnop}\right\}\sin\Phi d\Phi_1 d\Phi d\Phi_2}{\int_{\Phi_1=0}^{2\pi}\int_{\Phi=0}^{\pi}\int_{\Phi_2=0}^{2\pi} f(\Phi_1,\Phi,\Phi_2)\sin\Phi d\Phi_1 d\Phi d\Phi_2} \tag{2.47}$$

where $f(\Phi_1,\Phi,\Phi_2)$ is the ODF value at (Φ_1,Φ,Φ_2) and $\left\{S^C_{mnop}\right\}$ is the single crystal compliance tensor.

2.7.2 The Voigt model

The mechanical Voigt compliance tensor is equal to the X-ray Voigt compliance tensor and can be calculated using Eq. 2.35

$$\left\{C^S_{ijkl}\right\}^{\mathrm{V,M}} = \frac{\int_{\Phi_1=0}^{2\pi}\int_{\Phi=0}^{\pi}\int_{\Phi_2=0}^{2\pi} f(\Phi_1,\Phi,\Phi_2)a^{\epsilon}_{im}a^{\epsilon}_{jn}a^{\epsilon}_{ko}a^{\epsilon}_{lp}\left\{C^C_{mnop}\right\}\sin\Phi d\Phi_1 d\Phi d\Phi_2}{\int_{\Phi_1=0}^{2\pi}\int_{\Phi=0}^{\pi}\int_{\Phi_2=0}^{2\pi} f(\Phi_1,\Phi,\Phi_2)\sin\Phi d\Phi_1 d\Phi d\Phi_2} \tag{2.48}$$

where $f(\Phi_1,\Phi,\Phi_2)$ is the ODF value at (Φ_1,Φ,Φ_2) and $\left\{C^C_{mnop}\right\}$ is the single crystal stiffness tensor. The Voigt compliance tensor is calculated according to the transformation rules in Sec. 2.2.

$$\left\{S^S_{ijkl}\right\}^{\mathrm{V}} = (\left\{C^S_{ijkl}\right\}^{\mathrm{V}})^{-1} \tag{2.49}$$

2.7.3 The Hill model

The mechanical Hill compliance tensor is the arithmetic mean of the mechanical Reuss and Voigt compliance tensors (Eqs. 2.47, 2.48).

$$\left\{S^S_{ijkl}\right\}^{\mathrm{H,M}} = x\left\{S^S_{ijkl}\right\}^{\mathrm{R,M}} + (1-x)\left\{S^S_{ijkl}\right\}^{\mathrm{V}} \tag{2.50}$$

where x is the Hill factor.

2.8 Calculation of mechanical elastic constants

2.8.1 Using ODF

Sec. 2.7 explained how to calculate the mechanical elastic compliances. Although the calculation of mechanical elastic compliances is easier than the calculation of X-ray elastic compliances, an ODF is indispensable. The calculation is always performed in respect to the S system. Whenever mechanical properties in respect to any other coordinate system, *e.g.* the L system, are needed, it is necessary to transform the tensor components from $S \rightarrow L$. The procedure could be described in the following way

- Calculate (simulation) / determine (experiment) the ODF of the sample.
- Choose the grain interaction model.
- Calculate the averaged mechanical elastic compliance tensor components $\left\{S^S_{ijkl}\right\}^{\mathrm{M}}$ according to the grain interaction model in respect to the sample coordinate system S.
- Transform the averaged mechanical compliance tensor components to the laboratory system L at position (ϕ,ψ) using tensor transformation rule (Eq. 2.1) ($\left\{S^S_{ijkl}\right\}^{\mathrm{M}} \rightarrow \left\{S^L_{mnop}\right\}^{\mathrm{M}}_{\psi}$).
- Extract the desired mechanical elastic constant from the transformed averaged mechanical compliance tensor $\left\{S^L_{ijkl}\right\}^{\mathrm{M}}_{\psi}$, *e.g.* the Young's modulus in $\vec{L}_3$ direction $\left\{E^L_{3333}\right\}^{\mathrm{M}}_{\psi} = 1/\left\{S^L_{3333}\right\}^{\mathrm{M}}_{\psi}$.

This procedure can always be used to calculate the mechanical elastic constants for any direction, as long as the SECs, the ODF and the grain interaction model are known.

2.8.2 Using analytical formulas

For simple, symmetric textures it is possible to derive an analytical formula which fully and identically describes the mechanical behaviour of a thin film. The mechanical data calculated using this formula will be compared with the data directly calculated using commercial software products [65, 73].

The ODF can be simulated for different fiber textures using a software program like BearTEX [73] or LaboTex [65]. A fiber textured sample with the fiber axis parallel to $\vec{S}_3$ can easily be described through an analytical formula. In the case of a fiber texture with $\psi_{\mathrm{FWHM}} = 0°$, the mechanical elastic constants can be calculated according to [74]

$$\left\{S^S_{ijkl}\right\}^{\mathrm{R,M}} = \frac{1}{2\pi}\int_0^{2\pi}\left\{S^S_{ijkl}\right\}d\phi_1 \tag{2.51}$$

$$\left\{C^S_{ijkl}\right\}^{\mathrm{V}} = \frac{1}{2\pi}\int_0^{2\pi}\left\{C^S_{ijkl}\right\}d\phi_1 \tag{2.52}$$

where $\left\{S^S_{ijkl}\right\}$ and $\left\{C^S_{ijkl}\right\}$ are the single crystal compliance and stiffness tensors in the S system. For a (hkl) fiber texture $\left\{S^S_{ijkl}\right\}$ and $\left\{C^S_{ijkl}\right\}$ in Eqs. 2.51 and 2.52 can be obtained using

$$\left\{S^S_{ijkl}\right\} = a^{\phi}_{im}a^{\phi}_{jn}a^{\phi}_{ko}a^{\phi}_{lp}a^{\Omega}_{mq}a^{\Omega}_{nr}a^{\Omega}_{os}a^{\Omega}_{pt}\left\{S^C_{qrst}\right\} \tag{2.53}$$

$$\left\{C^S_{ijkl}\right\} = a^{\phi}_{im}a^{\phi}_{jn}a^{\phi}_{ko}a^{\phi}_{lp}a^{\Omega}_{mq}a^{\Omega}_{nr}a^{\Omega}_{os}a^{\Omega}_{pt}\left\{C^C_{qrst}\right\} \tag{2.54}$$

The integration of Eqs. 2.51 and 2.52 can then be performed for all tensor components as a function of ϕ for any (hkl) value. However, Eqs. 2.51 and 2.52 demand an infinitely sharp fiber texture. Therefore grains can only be randomly distributed around $\vec{S}_3$ but oriented with the (hkl) plane parallel to the sample surface. Eqs. 2.51 and 2.52 can be adapted to a Gaussian or Lorentzian distribution of grains in the out of plane direction. The Gauss- or Lorentzian distributions are characterized through the texture sharpness parameter ψ_{FWHM}. In the case of an infinitely sharp fiber texture, ψ_{FWHM} would be zero. As an example an analytical formula for a Gaussian shaped fiber texture is presented.

$$\left\{S^S_{ijkl}\right\}^{\mathrm{R,M}} = \frac{1}{2\pi N}\int_0^{2\pi}\int_0^{\pi}\int_0^{2\pi} e^{-5.545\frac{1}{2}(\frac{\psi}{\psi_{\mathrm{FWHM}}})^2}\left\{S^S_{ijkl}\right\}(\phi,\psi)\sin\psi d\phi d\psi d\lambda \tag{2.55}$$

$$\left\{C^S_{ijkl}\right\}^{\mathrm{V}} = \frac{1}{2\pi N}\int_0^{2\pi}\int_0^{\pi}\int_0^{2\pi} e^{-5.545\frac{1}{2}(\frac{\psi}{\psi_{\mathrm{FWHM}}})^2}\left\{C^S_{ijkl}\right\}(\phi,\psi)\sin\psi d\phi d\psi d\lambda \tag{2.56}$$

$$N = \int_0^{2\pi}\int_0^{\pi}\int_0^{2\pi} e^{-5.545\frac{1}{2}(\frac{\psi}{\psi_{\mathrm{FWHM}}})^2}\sin\psi d\phi d\psi d\lambda \tag{2.57}$$

Eqs. 2.55-2.57 can be used to calculate averaged mechanical compliance and stiffness tensor components of a Gaussian fiber texture with ψ_{FWHM}, using Eqs. 2.53 and 2.54 for $\left\{S^S_{ijkl}\right\}$ and $\left\{C^S_{ijkl}\right\}$. The factor -5.545 can be calculated as following

$$\begin{aligned} f(\psi) &= Ae^{-B\frac{1}{2}(\frac{\psi}{\psi_{\mathrm{FWHM}}})^2} \\ f(\psi = 0) &= 1 \rightarrow A = 1 \\ f(\psi = \frac{\psi_{\mathrm{FWHM}}}{2}) &= 0.5 \rightarrow B = 5.545 \end{aligned} \tag{2.58}$$

Eqs. 2.55, 2.56 and 2.50 can be used to calculate the averaged Reuss, Voigt and Hill compliance tensor components for any fiber textured material with cubic crystal symmetry and a specific ψ_{FWHM}. Fig. 2.9 shows the calculated *in-plane mechanical* Young's modulus $\left\{E^S_{1111}\right\}^{\mathrm{M}} = 1/\left\{S^S_{1111}\right\}^{\mathrm{M}}$ as a function of ψ_{FWHM} for a (111) fiber textured Cu sample. The circled data were calculated with Mathematica™ [55] using LaboTex [65] generated ODFs. The squared data were directly calculated from BearTEX software [73]. Export of ODFs was not necessary due to BearTEX can calculate the *mechanical* compliances directly. The triangle data were calculated using Eqs. 2.55,2.56 and 2.50. The data nearly show perfect correlation for all three calculations which demonstrates the validity of Eq. 2.55.

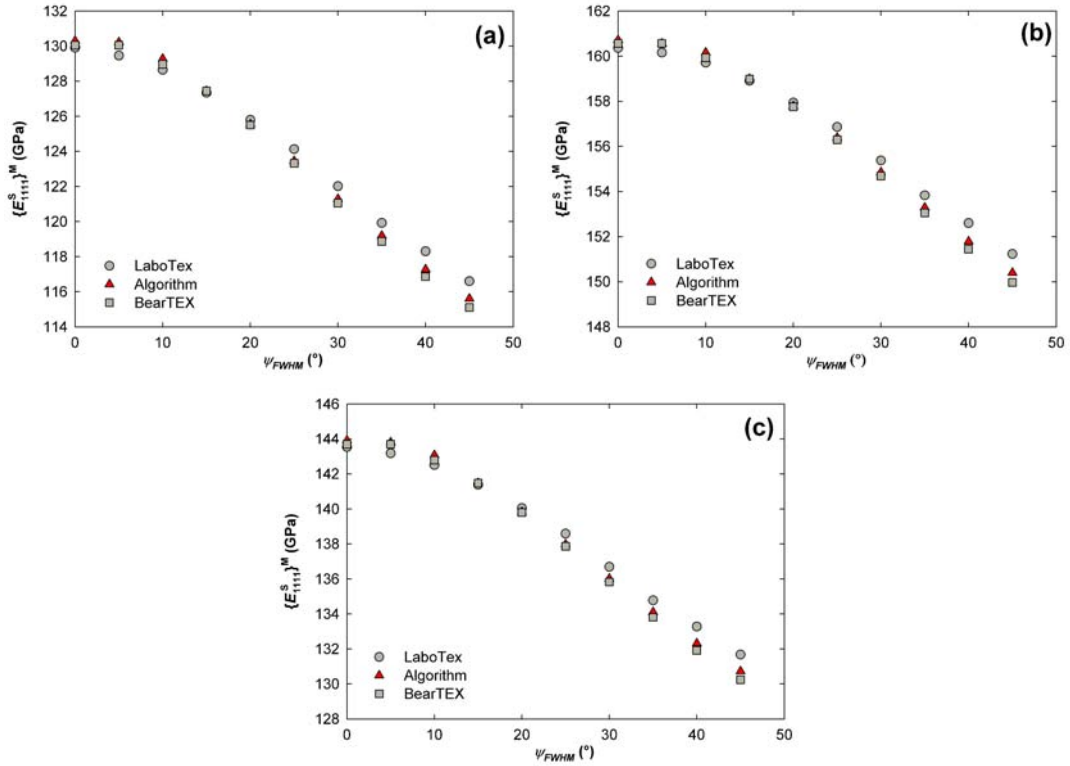

Figure 2.9: The plots represent calculated *mechanical in-plane* Young's moduli for (111) fiber textured Cu versus ψ_{FWHM} of the fiber texture. The circled data were calculated with Mathematica™ [55] using LaboTex [65] generated ODFs. The squared data were directly calculated from BearTEX software [73]. Export of ODFs was not necessary due to BearTEX can calculate the *mechanical* compliances directly. The triangle data were calculated using Eqs. 2.55, 2.56 and 2.50. The data nearly show perfect correlation for all three calculations which demonstrates the validity of Eq. 2.55. (a) Reuss, (b) Voigt (c) Hill model.

2.9 Anisotropy of X-ray strain

In polycrystalline materials, one can speak of three types of strain [61]. The strain of the first type is a macroscopic strain which corresponds to an average strain across many grains. The strain of the second type is an average strain in one grain. The strain of the third kind represents a local strain within a grain and originates from local lattice imperfections like inclusions, vacancies and dislocations. Any kind of strain can be related to stress when corresponding compliance tensor is known on the appropriate dimensional level.

Using X-ray diffraction, it is possible to characterize X-ray elastic strain or X-ray strain. In laboratory conditions when the beam size is much larger than the grain size, the shift of Bragg peaks corresponds to the strain of first type, macroscopic strain. The peak broadening is caused by the strain distribution in grains, *i.e.* by the strain

of second and third order. The application of synchrotron beams with the diameter below one micron opens a possibility to quantify strains of second and third order.
The X-ray strain can be determined from measured lattice spacing provided the unstressed lattice parameter is known. The lattice spacing measurement is performed by scanning *hkl* reflections. Since cubic crystals exhibit elastic anisotropy, X-ray strains obtained by the measurement of various (*hkl*) crystallographic planes are not equal. One speaks therefore of the anisotropy of X-ray strain.
Within this thesis macroscopic stresses characterized using X-ray diffraction substrate curvature method will be correlated with the macroscopic strain (strain of the first type) obtained by the measurement of *hkl* reflections. Provided there is no elastic anisotropy, X-ray strains obtained from various *hkl* reflections would be equal and would also correspond to the mechanical macroscopic strain. This special case occurs in tungsten. For the majority of other materials, the X-ray strains obtained by the measurement of various *hkl* reflections differ.
The knowledge of X-ray strains gives a possibility to extrapolate mechanical strain. According to the Hill grain interaction model, the X-ray strain measured on a *hkl* reflection with $3\Gamma_{hkl}$=0.6 correspond to the mechanical strain [75]. For textured materials, however, the $3\Gamma_{hkl}$ value can vary in the interval [0,1]. To demonstrate the anisotropic nature of the X-ray strain, X-ray strains were calculated for the three grain interaction models of Reuss, Voigt and Hill and for six materials KCl, CrN, W, Au, Cu. KCl and Na have got a Zener anisotropy factor (ZAR) [76] between 0.36 and 9.95, respectively [24] and can be considered as extreme examples for crystal elastic anisotropy. The corresponding SECs and unstressed lattice parameter can be found in Tab. 2.2. For the calculations, an equibiaxial stress of 100 MPa [57] was supposed and the X-ray strains were calculated as a function of $\sin^2\psi$.
The numerical data in Figs. 2.10-2.18 document that X-ray strains depend on the fibre texture type and sharpness (macroscopic elastic anisotropy), crystal elastic anisotropy and amount of randomly oriented crystallites. The $\left\{\epsilon_{33}^{L}\right\}_{\psi}^{hkl}$ dependencies from Figs. 2.10-2.18 were fitted in order to obtain intercepts on $\left\{\epsilon_{33}^{L}\right\}_{\psi}^{hkl}$ axis and slopes which are summarized in Tabs. 2.3-2.6.

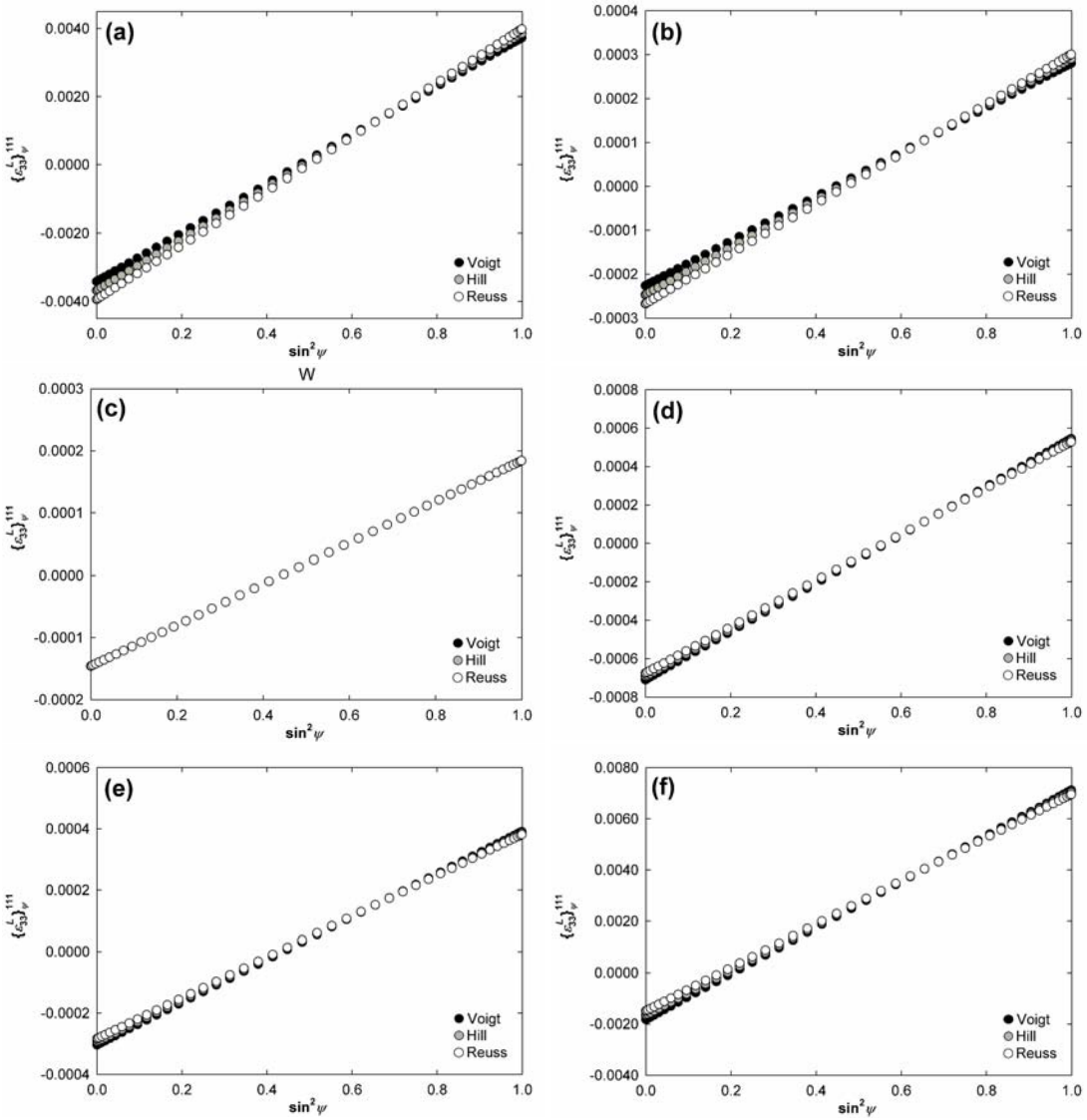

Figure 2.10: The calculated X-ray strains of a 111 crystallographic reflex for the 6 materials KCl (a), CrN (b), W (c), Au (d), Cu (e) and Na (f) are plotted for the three grain interaction models of Reuss, Voigt and Hill (Gaussian (111) fiber texture, $\psi_{\mathrm{FWHM}} = 10°$, 10% ISO). An equibiaxial stress of 100 MPa [57] was used in the model. The X-ray strain of a 111 reflex for any texture is always linear.

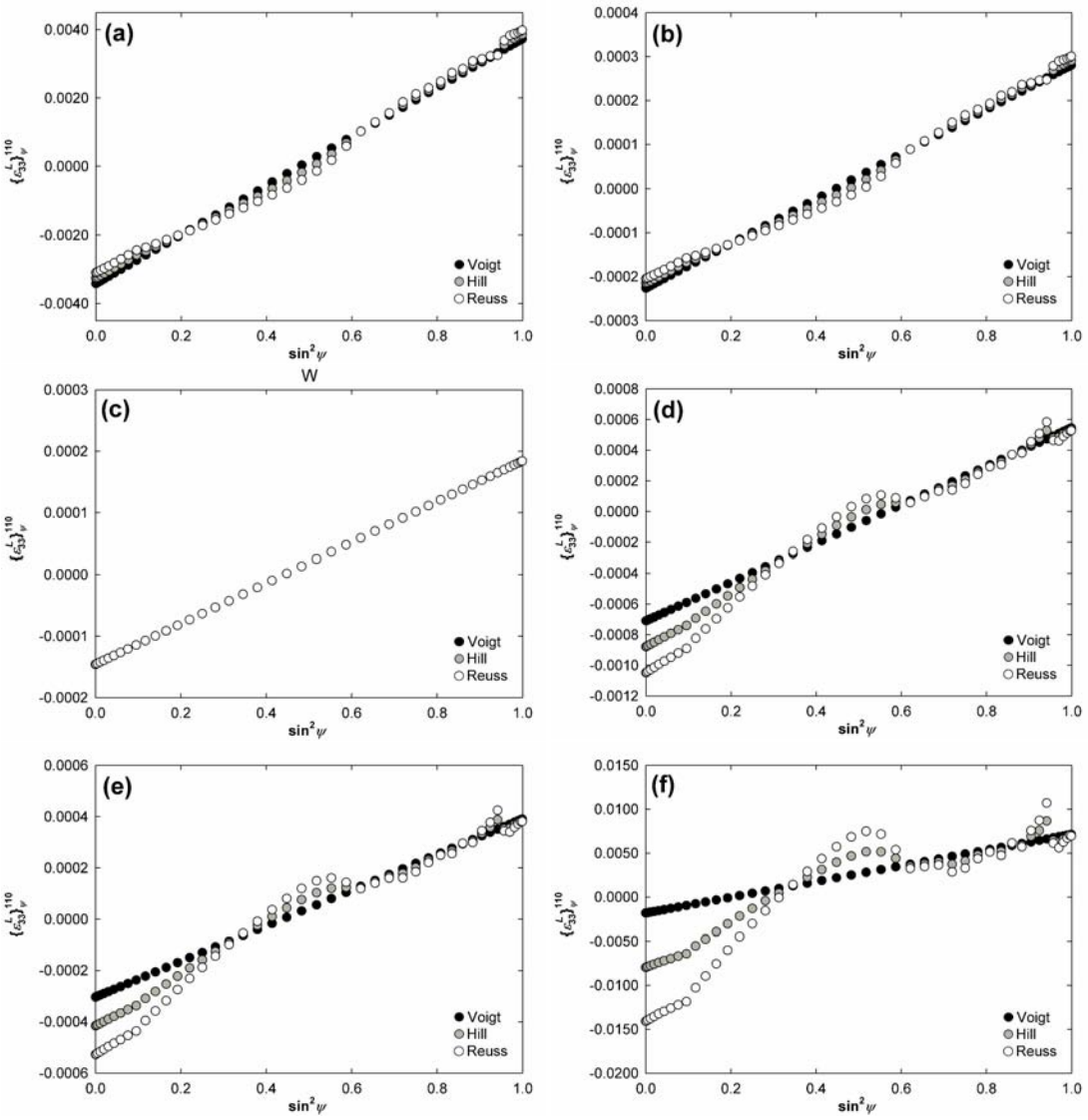

Figure 2.11: The calculated X-ray strains of a 110 crystallographic reflex for the 6 materials KCl (a), CrN (b), W (c), Au (d), Cu (e) and Na (f) are plotted for the three grain interaction models of Reuss, Voigt and Hill (Gaussian (111) fiber texture, $\psi_{\mathrm{FWHM}} = 10°$, 10% ISO). An equibiaxial stress of 100 MPa [57] was used in the model.

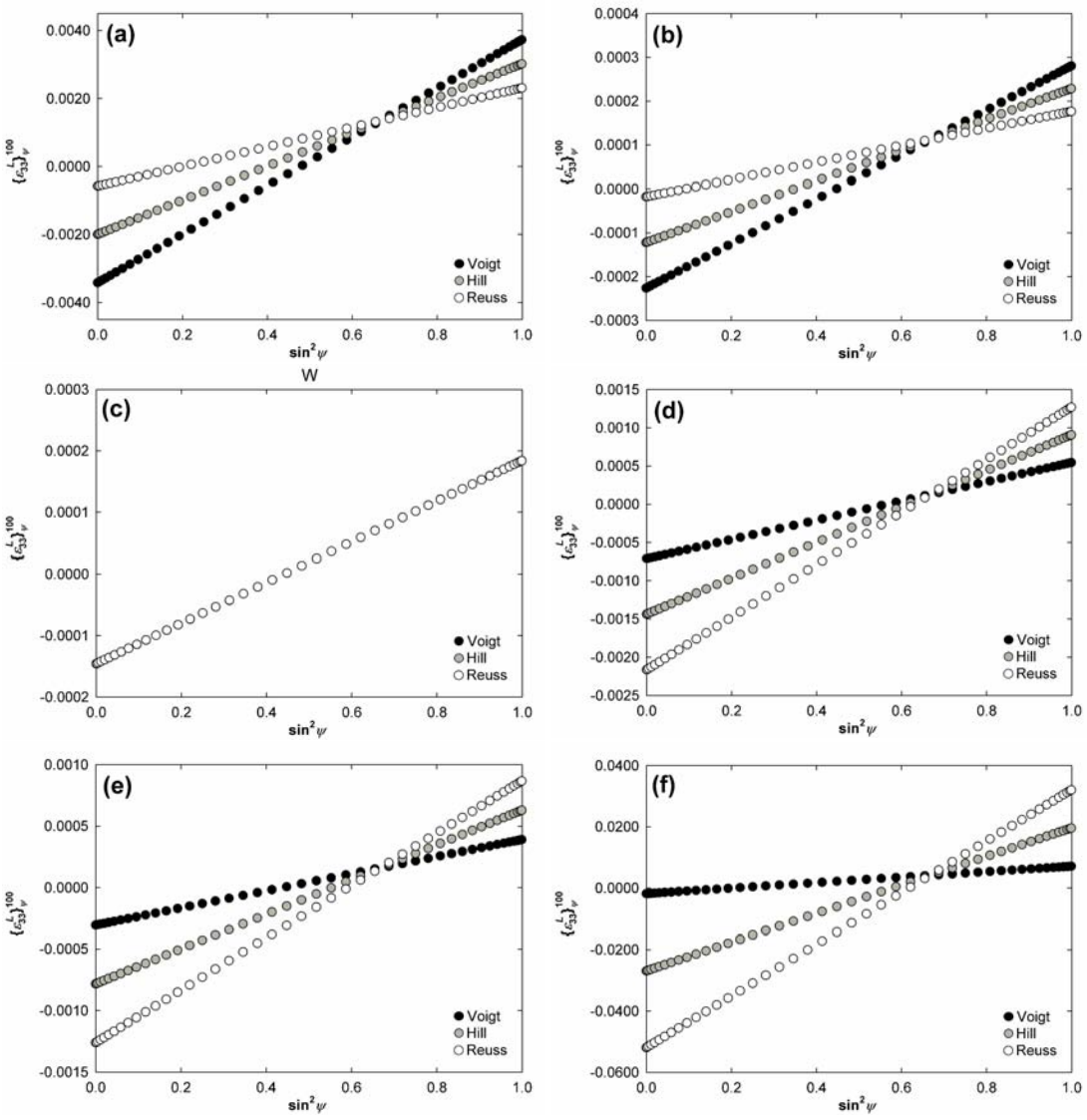

Figure 2.12: The calculated X-ray strains of a 100 crystallographic reflex for the 6 materials KCl (a), CrN (b), W (c), Au (d), Cu (e) and Na (f) are plotted for the three grain interaction models of Reuss, Voigt and Hill (Gaussian (111) fiber texture, $\psi_{\mathrm{FWHM}} = 10°$, 10% ISO). An equibiaxial stress of 100 MPa [57] was used in the model. The X-ray strain of a 100 reflex for any texture is always linear.

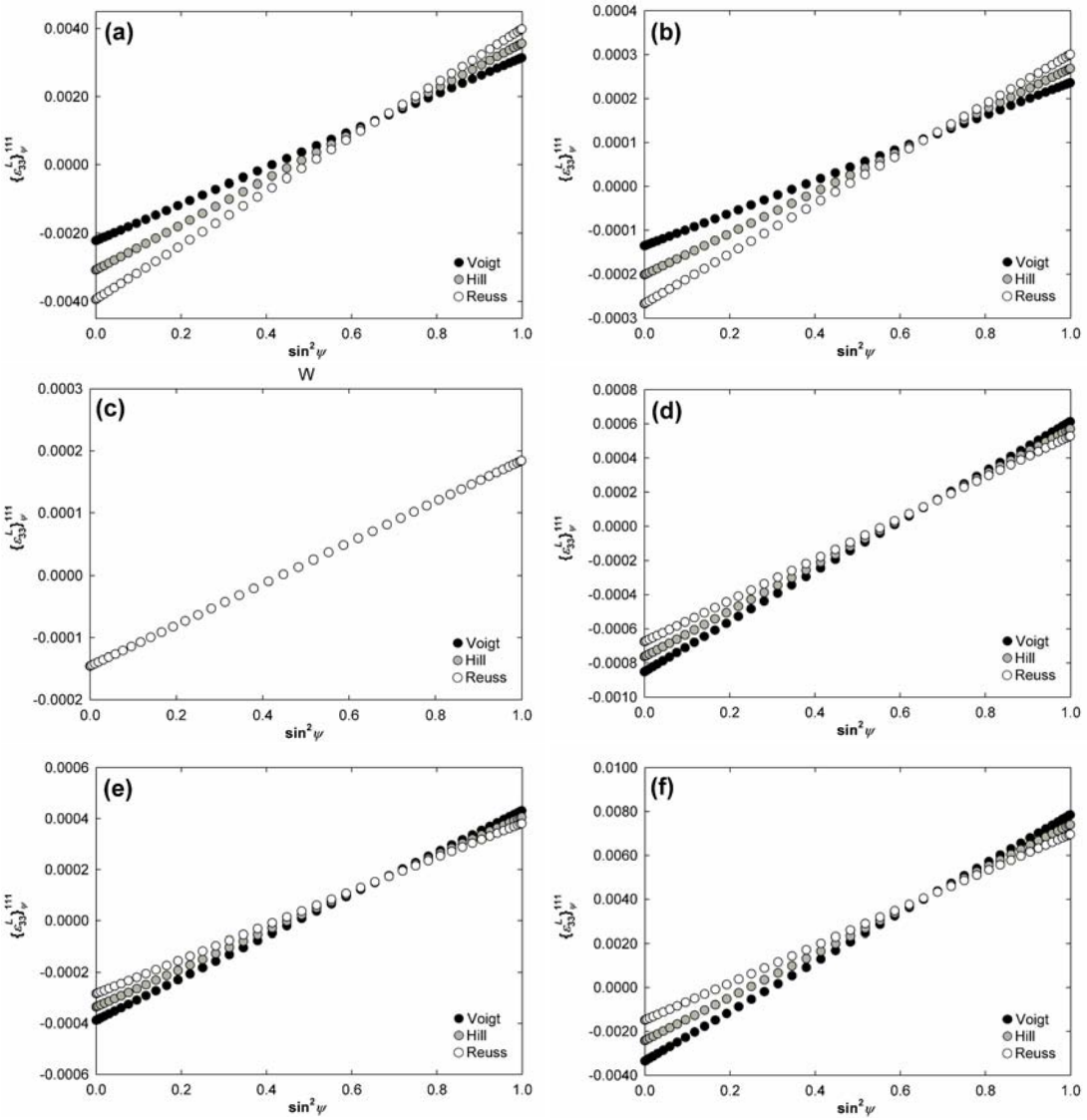

Figure 2.13: The calculated X-ray strains of a 111 crystallographic reflex for the 6 materials KCl (a), CrN (b), W (c), Au (d), Cu (e) and Na (f) are plotted for the three grain interaction models of Reuss, Voigt and Hill (Gaussian (110) fiber texture, $\psi_{\mathrm{FWHM}} = 10°$, 10% ISO). An equibiaxial stress of 100 MPa [57] was used in the model. The X-ray strain of a 111 reflex for any texture is always linear.

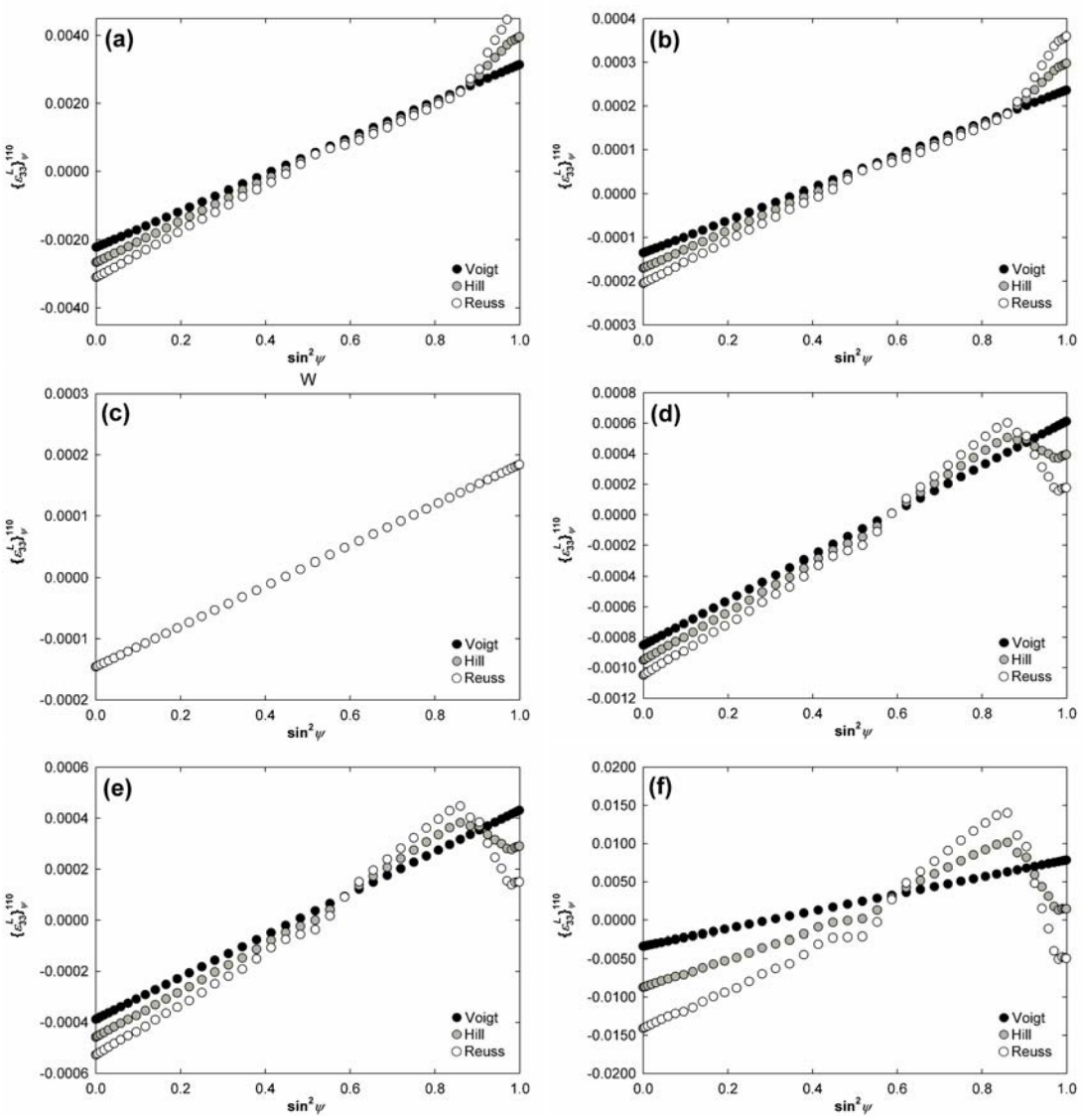

Figure 2.14: The calculated X-ray strains of a 110 crystallographic reflex for the 6 materials KCl (a), CrN (b), W (c), Au (d), Cu (e) and Na (f) are plotted for the three grain interaction models of Reuss, Voigt and Hill (Gaussian (110) fiber texture, $\psi_{\mathrm{FWHM}} = 10^{\circ}$, 10% ISO). An equibiaxial stress of 100 MPa [57] was used in the model.

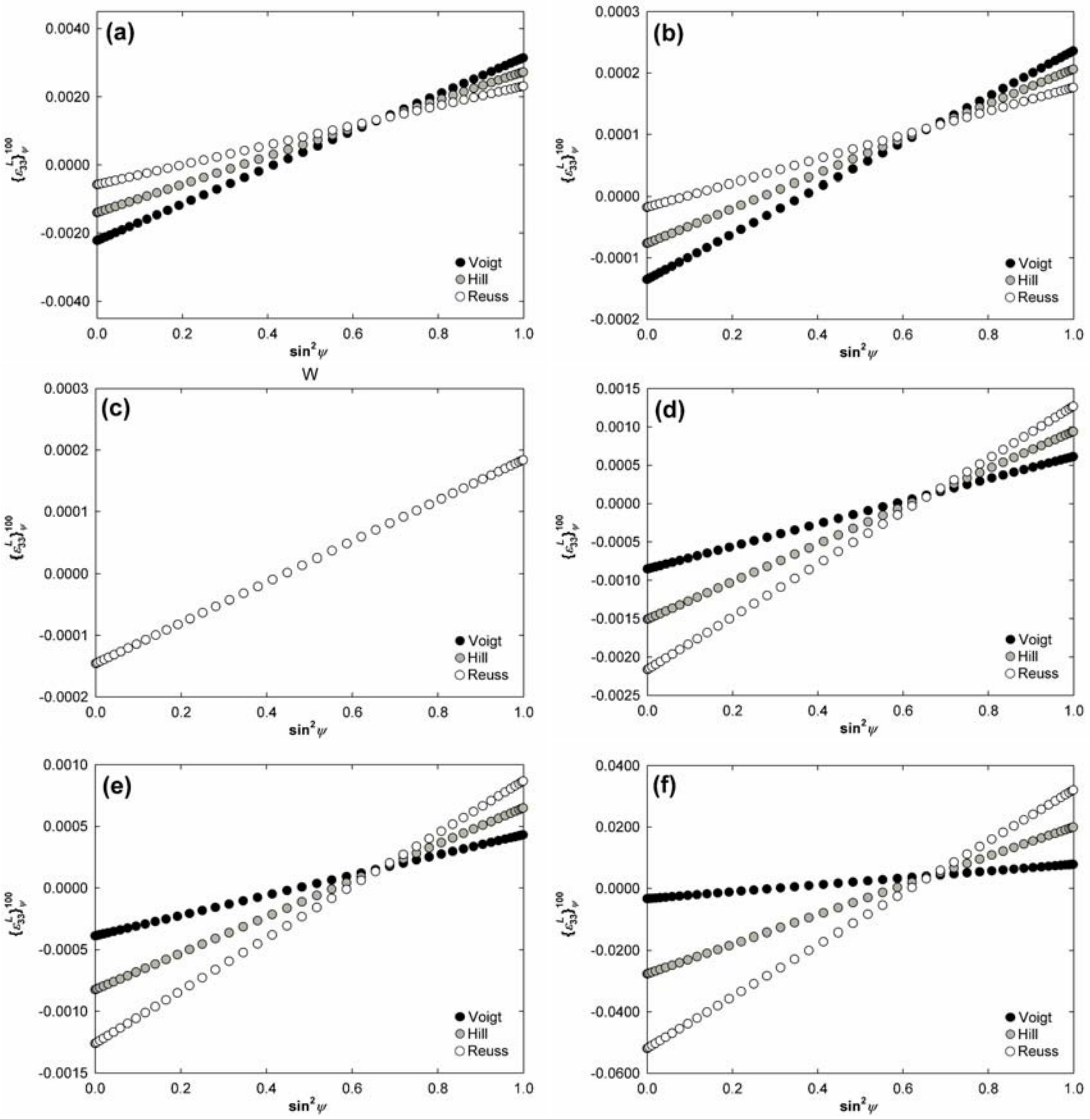

Figure 2.15: The calculated X-ray strains of a 100 crystallographic reflex for the 6 materials KCl (a), CrN (b), W (c), Au (d), Cu (e) and Na (f) are plotted for the three grain interaction models of Reuss, Voigt and Hill (Gaussian (110) fiber texture, $\psi_{\mathrm{FWHM}} = 10°$, 10% ISO). An equibiaxial stress of 100 MPa [57] was used in the model. The X-ray strain of a 100 reflex for any texture is always linear.

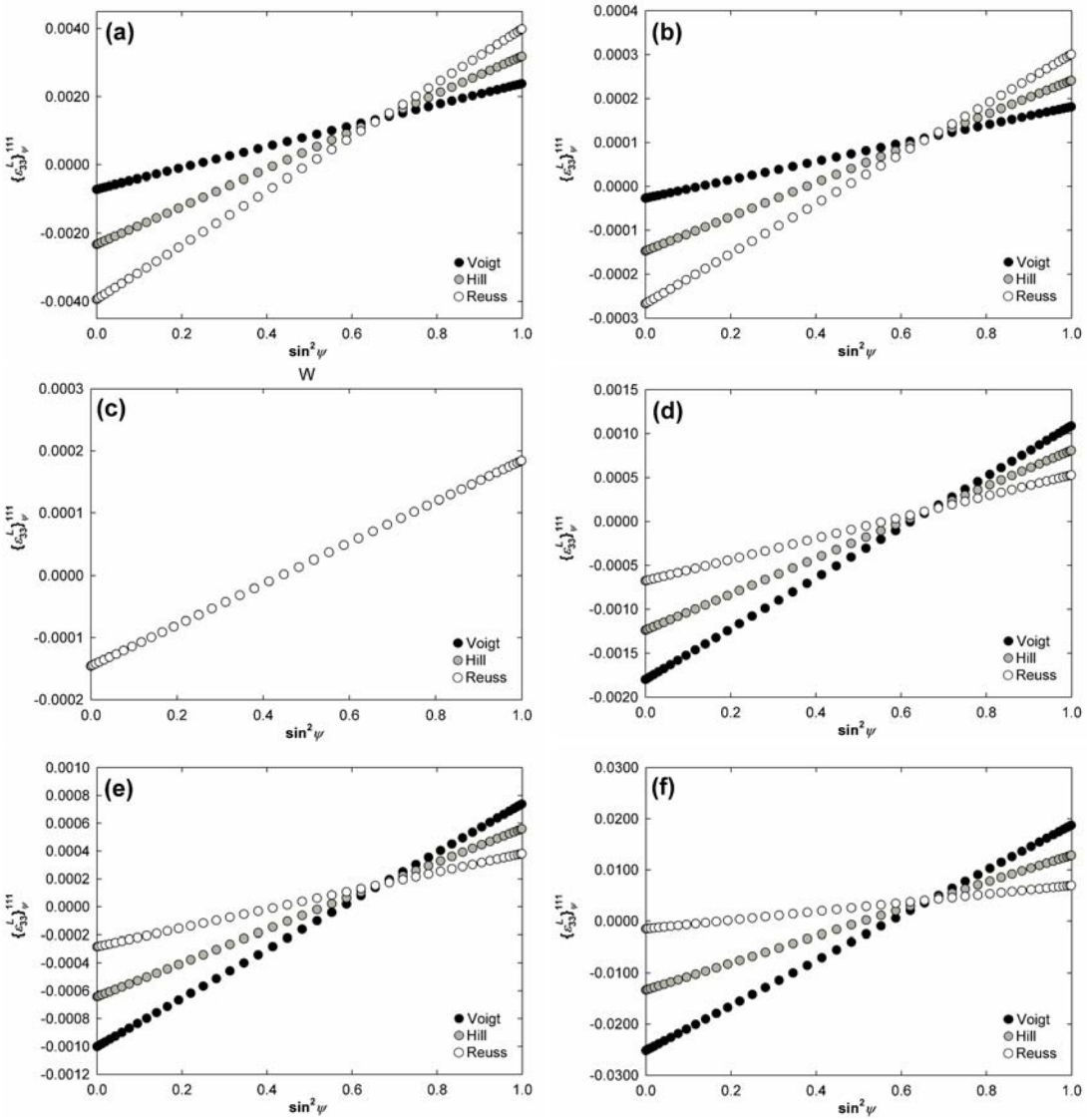

Figure 2.16: The calculated X-ray strains of a 111 crystallographic reflex for the 6 materials KCl (a), CrN (b), W (c), Au (d), Cu (e) and Na (f) are plotted for the three grain interaction models of Reuss, Voigt and Hill (Gaussian (100) fiber texture, $\psi_{\mathrm{FWHM}} = 10°$, 10% ISO). An equibiaxial stress of 100 MPa [57] was used in the model. The X-ray strain of a 111 reflex for any texture is always linear.

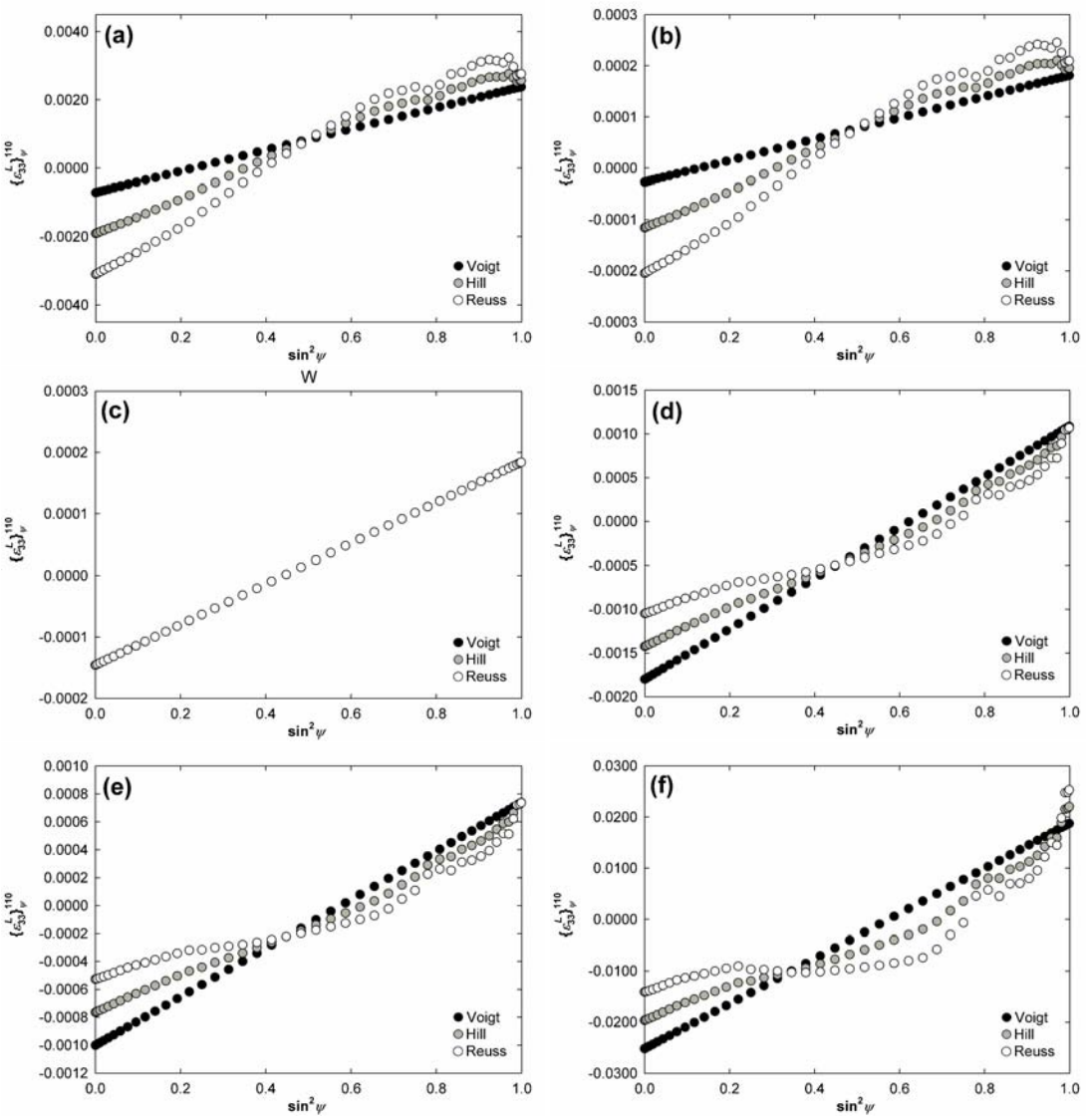

Figure 2.17: The calculated X-ray strains of a 110 crystallographic reflex for the 6 materials CrN,KCl,W,Au,Cu and Na are plotted for the three grain interaction models of Reuss, Voigt and Hill (Gaussian (100) fiber texture, $\psi_{\mathrm{FWHM}} = 10^{\circ}$, 10% ISO). An equibiaxial stress of 100 MPa [57] was used in the model.

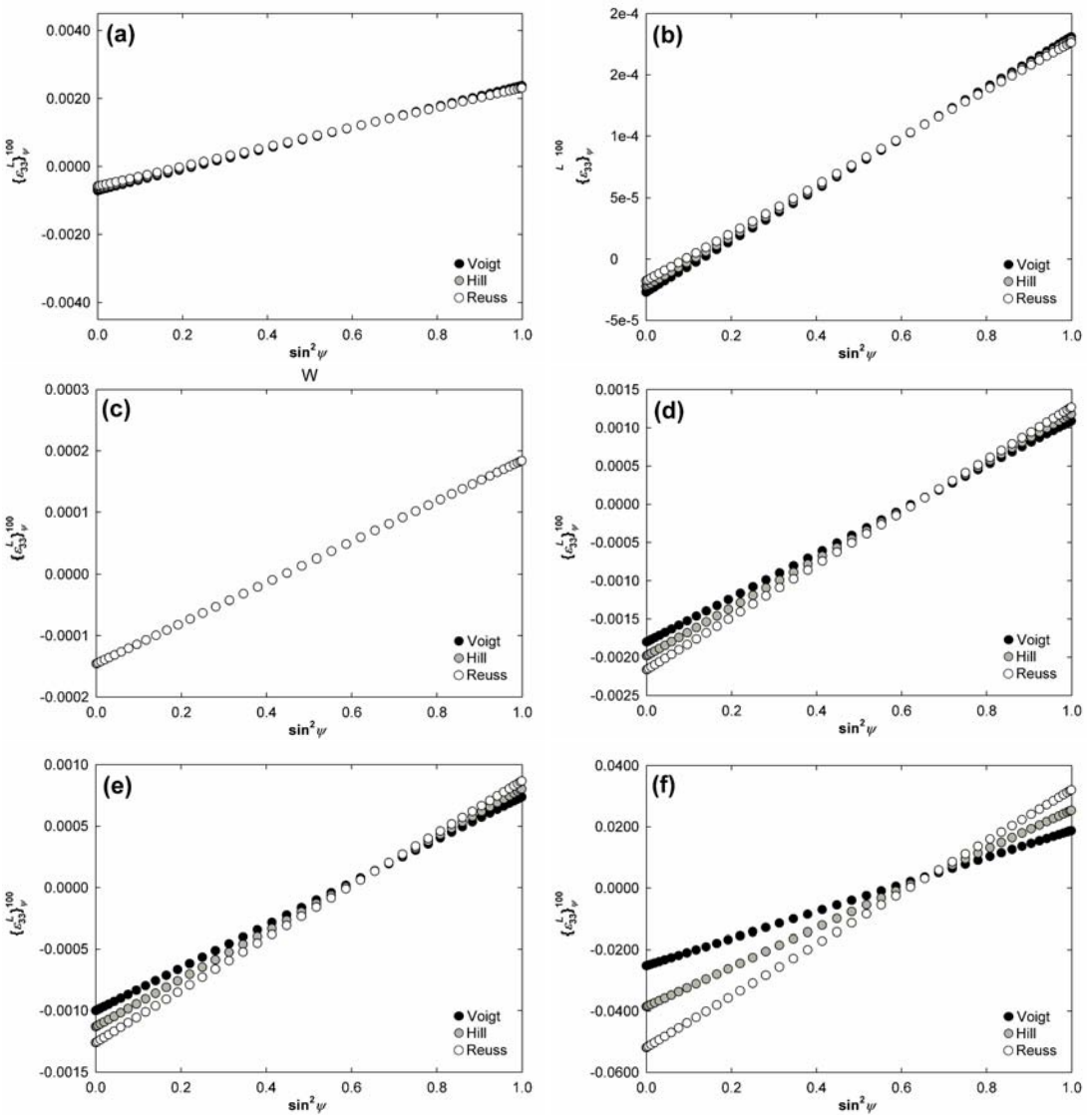

Figure 2.18: The calculated X-ray strains of a 100 crystallographic reflex for the 6 materials KCl (a), CrN (b), W (c), Au (d), Cu (e) and Na (f) are plotted for the three grain interaction models of Reuss, Voigt and Hill (Gaussian (100) fiber texture, $\psi_{\mathrm{FWHM}} = 10°$, 10% ISO). An equibiaxial stress of 100 MPa [57] was used in the model. The X-ray strain of a 100 reflex for any texture is always linear.

Table 2.3: Fitted intersections $\left\{\epsilon_{33}^{L}\right\}_{\psi=0^\circ}^{hkl}$ of X-ray strain plots in Figs. 2.10-2.18 at $\psi = 0^\circ$.

			KCl	CrN	W	Au	Cu	Na
			10^{-4}	10^{-4}	10^{-4}	10^{-4}	10^{-4}	10^{-4}
100 Fiber	100	Reflex	Reuss	-5.7452	-0.1759	-1.4570	-21.6287	-12.6000	-518.7389
			Voigt	-7.0504	-0.2668	-1.4571	-18.0046	-10.0054	-251.8532
			Hill	-6.3978	-0.2214	-1.4571	-19.8167	-11.3027	-385.2961
	110	Reflex	Reuss	-28.8855	-1.8910	-1.4580	-11.3955	-5.8821	-172.1262
			Voigt	-7.0504	-0.2668	-1.4571	-18.0046	-10.0054	-251.8532
			Hill	-17.9680	-1.0789	-1.4576	-14.7001	-7.9438	-211.9897
	111	Reflex	Reuss	-39.3874	-2.6693	-1.4585	-6.7513	-2.8333	-14.8211
			Voigt	-7.0504	-0.2668	-1.4571	-18.0046	-10.0054	-251.8532
			Hill	-23.2189	-1.4681	-1.4578	-12.3780	-6.4193	-133.3372
110 Fiber	100	Reflex	Reuss	-5.7452	-0.1759	-1.4570	-21.6287	-12.6000	-518.7389
			Voigt	-22.1680	-1.3535	-1.4581	-8.5057	-3.8723	-33.4128
			Hill	-13.9566	-0.7647	-1.4575	-15.0672	-8.2362	-276.0759
	110	Reflex	Reuss	-32.2511	-2.1404	-1.4581	-9.9072	-4.9051	-121.7141
			Voigt	-22.1680	-1.3535	-1.4581	-8.5057	-3.8723	-33.4128
			Hill	-27.2095	-1.7470	-1.4581	-9.2065	-4.3887	-77.5635
	111	Reflex	Reuss	-39.3874	-2.6693	-1.4585	-6.7513	-2.8333	-14.8211
			Voigt	-22.1680	-1.3535	-1.4581	-8.5057	-3.8723	-33.4128
			Hill	-30.7777	-2.0114	-1.4583	-7.6285	-3.3528	-24.1170
111 Fiber	100	Reflex	Reuss	-5.7452	-0.1759	-1.4570	-21.6287	-12.6000	-518.7389
			Voigt	-34.1564	-2.2603	-1.4584	-7.0923	-3.0332	-18.1844
			Hill	-19.9508	-1.2181	-1.4577	-14.3605	-7.8166	-268.4617
	110	Reflex	Reuss	-33.2168	-2.2120	-1.4582	-9.4801	-4.6247	-107.2493
			Voigt	-34.1564	-2.2603	-1.4584	-7.0923	-3.0332	-18.1844
			Hill	-33.6866	-2.2362	-1.4583	-8.2862	-3.8290	-62.7168
	111	Reflex	Reuss	-39.3874	-2.6693	-1.4585	-6.7513	-2.8333	-14.8211
			Voigt	-34.1564	-2.2603	-1.4584	-7.0923	-3.0332	-18.1844
			Hill	-36.7719	-2.4648	-1.4584	-6.9218	-2.9333	-16.5028

Table 2.4: Calculated intersections' standard deviations $\Delta\left\{\varepsilon_{33}^{L}\right\}_{\psi=0^\circ}^{hkl}$ of X-ray strain slopes in Figs. 2.10-2.18.

			KCl 10^{-4}	CrN 10^{-4}	W 10^{-4}	Au 10^{-4}	Cu 10^{-4}	Na 10^{-4}
100 Fiber	100 Reflex	Reuss	0.0000	0.0000	0.0000	0.0000	0.0000	0.0000
		Voigt	0.0000	0.0000	0.0000	0.0000	0.0000	0.0000
		Hill	0.0000	0.0000	0.0000	0.0000	0.0000	0.0000
	110 Reflex	Reuss	0.9660	0.0000	0.0000	0.4272	0.2804	14.4689
		Voigt	0.0000	0.0000	0.0000	0.0000	0.0000	0.0000
		Hill	0.4846	0.0000	0.0000	0.2142	0.1406	7.2483
	111 Reflex	Reuss	0.0000	0.0000	0.0000	0.0000	0.0000	0.0000
		Voigt	0.0000	0.0000	0.0000	0.0000	0.0000	0.0000
		Hill	0.0000	0.0000	0.0000	0.0000	0.0000	0.0000
110 Fiber	100 Reflex	Reuss	0.0000	0.0000	0.0000	0.0000	0.0000	0.0000
		Voigt	0.0000	0.0000	0.0000	0.0000	0.0000	0.0000
		Hill	0.0000	0.0000	0.0000	0.0000	0.0000	0.0000
	110 Reflex	Reuss	0.9807	0.0000	0.0000	0.4337	0.2847	14.6894
		Voigt	0.0000	0.0000	0.0000	0.0000	0.0000	0.0000
		Hill	0.4915	0.0000	0.0000	0.2172	0.1425	7.3488
	111 Reflex	Reuss	0.0000	0.0000	0.0000	0.0000	0.0000	0.0000
		Voigt	0.0000	0.0000	0.0000	0.0000	0.0000	0.0000
		Hill	0.0000	0.0000	0.0000	0.0000	0.0000	0.0000
111 Fiber	100 Reflex	Reuss	0.0000	0.0000	0.0000	0.0000	0.0000	0.0000
		Voigt	0.0000	0.0000	0.0000	0.0000	0.0000	0.0000
		Hill	0.0000	0.0000	0.0000	0.0000	0.0000	0.0000
	110 Reflex	Reuss	0.6070	0.0000	0.0000	0.2684	0.1762	9.0920
		Voigt	0.0000	0.0000	0.0000	0.0000	0.0000	0.0000
		Hill	0.3037	0.0000	0.0000	0.1343	0.0000	4.5467
	111 Reflex	Reuss	0.0000	0.0000	0.0000	0.0000	0.0000	0.0000
		Voigt	0.0000	0.0000	0.0000	0.0000	0.0000	0.0000
		Hill	0.0000	0.0000	0.0000	0.0000	0.0000	0.0000

Table 2.5: Fitted averaged slopes of X-ray strain plots in Figs. 2.10-2.18.

			KCl	CrN	W	Au	Cu	Na
			10^{-4}	10^{-4}	10^{-4}	10^{-4}	10^{-4}	10^{-4}
100 Fiber	100 Reflex	Reuss	28.9017	1.9417	3.3003	34.3643	21.3000	840.3361
		Voigt	30.9078	2.0816	3.3006	28.9075	17.3948	439.5560
		Hill	29.9047	2.0117	3.3004	31.6359	19.3474	639.9461
	110 Reflex	Reuss	65.4166	4.6480	3.3019	18.2165	10.6994	293.3899
		Voigt	30.9078	2.0816	3.3006	28.9075	17.3948	439.5560
		Hill	48.1622	3.3648	3.3012	23.5620	14.0471	366.4730
	111 Reflex	Reuss	79.3651	5.6818	3.3025	12.0482	6.6500	84.4595
		Voigt	30.9078	2.0816	3.3006	28.9075	17.3948	439.5560
		Hill	55.1364	3.8817	3.3015	20.4779	12.0224	262.0077
110 Fiber	100 Reflex	Reuss	28.9017	1.9417	3.3003	34.3643	21.3000	840.3361
		Voigt	53.6401	3.7158	3.3019	14.6587	8.1958	112.0996
		Hill	41.2709	2.8288	3.3011	24.5115	14.7479	476.2178
	110 Reflex	Reuss	72.2681	5.1558	3.3022	15.1867	8.7103	190.7637
		Voigt	53.6401	3.7158	3.3019	14.6587	8.1958	112.0996
		Hill	62.9541	4.4358	3.3021	14.9227	8.4530	151.4316
	111 Reflex	Reuss	79.3651	5.6818	3.3025	12.0482	6.6500	84.4595
		Voigt	53.6401	3.7158	3.3019	14.6587	8.1958	112.0996
		Hill	66.5026	4.6988	3.3022	13.3534	7.4229	98.2795
111 Fiber	100 Reflex	Reuss	28.9017	1.9417	3.3003	34.3643	21.3000	840.3361
		Voigt	71.5289	5.0692	3.3024	12.5590	6.9493	89.4996
		Hill	50.2153	3.5055	3.3014	23.4616	14.1247	464.9179
	110 Reflex	Reuss	71.0977	5.0691	3.3022	15.7042	9.0501	208.2947
		Voigt	71.5289	5.0692	3.3024	12.5590	6.9493	89.4996
		Hill	71.3133	5.0691	3.3023	14.1316	7.9997	148.8972
	111 Reflex	Reuss	79.3651	5.6818	3.3025	12.0482	6.6500	84.4595
		Voigt	71.5289	5.0692	3.3024	12.5590	6.9493	89.4996
		Hill	75.4470	5.3755	3.3024	12.3036	6.7997	86.9795

Table 2.6: Calculated averegd slopes' standard deviations of X-ray strain plots in Figs. 2.10-2.18.

			KCl 10^{-4}	CrN 10^{-4}	W 10^{-4}	Au 10^{-4}	Cu 10^{-4}	Na 10^{-4}
100 Fiber	100 Reflex	Reuss	0.0000	0.0000	0.0000	0.0000	0.0000	0.0000
		Voigt	0.0000	0.0000	0.0000	0.0000	0.0000	0.0000
		Hill	0.0000	0.0000	0.0000	0.0000	0.0000	0.0000
	110 Reflex	Reuss	1.6013	0.1187	0.0000	0.7081	0.4649	23.9857
		Voigt	0.0000	0.0000	0.0000	0.0000	0.0000	0.0000
		Hill	0.8033	0.0000	0.0000	0.3551	0.2331	12.0157
	111 Reflex	Reuss	0.0000	0.0000	0.0000	0.0000	0.0000	0.0000
		Voigt	0.0000	0.0000	0.0000	0.0000	0.0000	0.0000
		Hill	0.0000	0.0000	0.0000	0.0000	0.0000	0.0000
110 Fiber	100 Reflex	Reuss	0.0000	0.0000	0.0000	0.0000	0.0000	0.0000
		Voigt	0.0000	0.0000	0.0000	0.0000	0.0000	0.0000
		Hill	0.0000	0.0000	0.0000	0.0000	0.0000	0.0000
	110 Reflex	Reuss	1.6257	0.1205	0.0000	0.7189	0.4720	24.3512
		Voigt	0.0000	0.0000	0.0000	0.0000	0.0000	0.0000
		Hill	0.8148	0.0000	0.0000	0.3600	0.2363	12.1824
	111 Reflex	Reuss	0.0000	0.0000	0.0000	0.0000	0.0000	0.0000
		Voigt	0.0000	0.0000	0.0000	0.0000	0.0000	0.0000
		Hill	0.0000	0.0000	0.0000	0.0000	0.0000	0.0000
111 Fiber	100 Reflex	Reuss	0.0000	0.0000	0.0000	0.0000	0.0000	0.0000
		Voigt	0.0000	0.0000	0.0000	0.0000	0.0000	0.0000
		Hill	0.0000	0.0000	0.0000	0.0000	0.0000	0.0000
	110 Reflex	Reuss	1.0062	0.0000	0.0000	0.4450	0.2921	15.0722
		Voigt	0.0000	0.0000	0.0000	0.0000	0.0000	0.0000
		Hill	0.5035	0.0000	0.0000	0.2226	0.1461	7.5373
	111 Reflex	Reuss	0.0000	0.0000	0.0000	0.0000	0.0000	0.0000
		Voigt	0.0000	0.0000	0.0000	0.0000	0.0000	0.0000
		Hill	0.0000	0.0000	0.0000	0.0000	0.0000	0.0000

2.10 $3\Gamma_{hkl}$ plot

According to [75] it is possible to express the X-ray elastic compliances of a cubic material as a function of the parameter Γ_{hkl} which holds

$$\Gamma_{hkl} = \frac{h^2k^2 + k^2l^2 + l^2h^2}{(h^2 + k^2 + l^2)^2} \tag{2.59}$$

Γ_{hkl} is a pure function of the crystallographic reflex *hkl* and is called the X-ray anisotropy factor [62]. Commonly, X-ray elastic compliances are unequal for different crystallographic planes. Therefore, the X-ray elastic compliances differ as a function of Γ_{hkl}. All possible X-ray elastic compliances are constrained by the X-ray elastic compliances at $3\Gamma_{hkl} = 0.0$ and $3\Gamma_{hkl} = 1.0$. Moreover, it will be necessary not just to plot particular compliance components as a function of $3\Gamma_{hkl}$ but also algebraic expressions of compliances. The phrase *compliance term* will be used in following sections either as synonym for a particular compliance tensor component (*e.g.* $\left\{S^L_{3333}\right\}_\psi$) or an algebraic expression (*e.g.* $\left\{S^L_{3333}\right\}_\psi - \left\{S^L_{3311}\right\}_\psi$) of compliance components. *Experimentally* the *compliance terms* $\left\{S^L_{3311}\right\}_\psi + \left\{S^L_{3322}\right\}_\psi$ and $\left\{S^L_{3333}\right\}_\psi - \left\{S^L_{3311}\right\}_\psi$ can be determined from the averaged slopes and intersections of the $\left\{\epsilon^L_{33}\right\}^{hkl}_\psi - \sin^2\psi$ plots (see Sec. 2.6). As an example, the averaged slopes and intersections of the *calculated* $\left\{\epsilon^L_{33}\right\}^{hkl}_\psi - \sin^2\psi$ plots for the six materials KCl, CrN, W, Au, Cu and Na in Figs. 2.10-2.18 were determined and written to Tabs. 2.3-2.6. The intersection of the $\left\{\epsilon^L_{33}\right\}^{hkl}_\psi - \sin^2\psi$ plot at $\psi = 0°$ was used to calculate the compliance term $\left\{S^L_{3311}\right\}_\psi + \left\{S^L_{3322}\right\}_\psi$ (Eq. 2.40) according to an equibiaxial stress state of 100 MPa. Moreover, the averaged slope of the $\left\{\epsilon^L_{33}\right\}^{hkl}_\psi - \sin^2\psi$ plot and the equibiaxial stress were used to calculate the compliance term $\left\{S^L_{3333}\right\}_\psi - \left\{S^L_{3311}\right\}_\psi$ (Eq. 2.41). The *compliance term* $\left\{S^L_{3322}\right\}_{\psi=90°} + \left\{S^L_{3333}\right\}_{\psi=90°}$ was not determined from the $\left\{\epsilon^L_{33}\right\}^{hkl}_\psi - \sin^2\psi$ plots. The value $\left\{\epsilon^L_{33}\right\}^{hkl}_{\psi=90°}$ or the intersection of the linear fit at $\psi = 90°$ can be used to calculate $\left\{S^L_{3322}\right\}_{\psi=90°} + \left\{S^L_{3333}\right\}_{\psi=90°}$ using Eq. 2.45. The *compliance terms* were determined for four crystallographic reflexes *hkl* (with different values for $3\Gamma_{hkl}$) and plotted as a function of the corresponding $3\Gamma_{hkl}$ value (Figs. 2.19 and 2.20). The procedure to calculate a $3\Gamma_{hkl}$ plot is summarized in the following list

- Choose $n \geq 2$ crystallographic reflexes *hkl* with different $3\Gamma_{hkl}$.
- Calculate (simulation) / determine (experiment) n $\left\{\epsilon^L_{33}\right\}^{hkl}_\psi - \sin^2\psi$ plots.
- Determine the strain $\left\{\epsilon^L_{33}\right\}^{hkl}_{\psi=0°}$ at $\psi = 0°$ of all n $\left\{\epsilon^L_{33}\right\}^{hkl}_\psi - \sin^2\psi$ plots to calculate n $\left\{S^L_{3311}\right\}_{\psi=0°} + \left\{S^L_{3322}\right\}_{\psi=0°}$ *compliance terms* (Eq. 2.40)
- Determine the averaged slopes of all n $\left\{\epsilon^L_{33}\right\}^{hkl}_\psi - \sin^2\psi$ plots to calculate n $\left\{S^L_{3333}\right\}_{\psi=0°} - \left\{S^L_{3322}\right\}_{\psi=0°}$ *compliance terms* (Eq. 2.41).

- Determine the strain $\left\{\epsilon_{33}^{L}\right\}_{\psi=90^{\circ}}^{hkl}$ at $\psi = 90^{\circ}$ of all n $\left\{\epsilon_{33}^{L}\right\}_{\psi}^{hkl} - \sin^2\psi$ plots to calculate n $\left\{S_{3322}^{L}\right\}_{\psi=90^{\circ}} + \left\{S_{3333}^{L}\right\}_{\psi=90^{\circ}}$ *compliance terms* (Eq. 2.45).
- Plot the n *compliance terms* as a function of the corresponding $3\Gamma_{hkl}$.

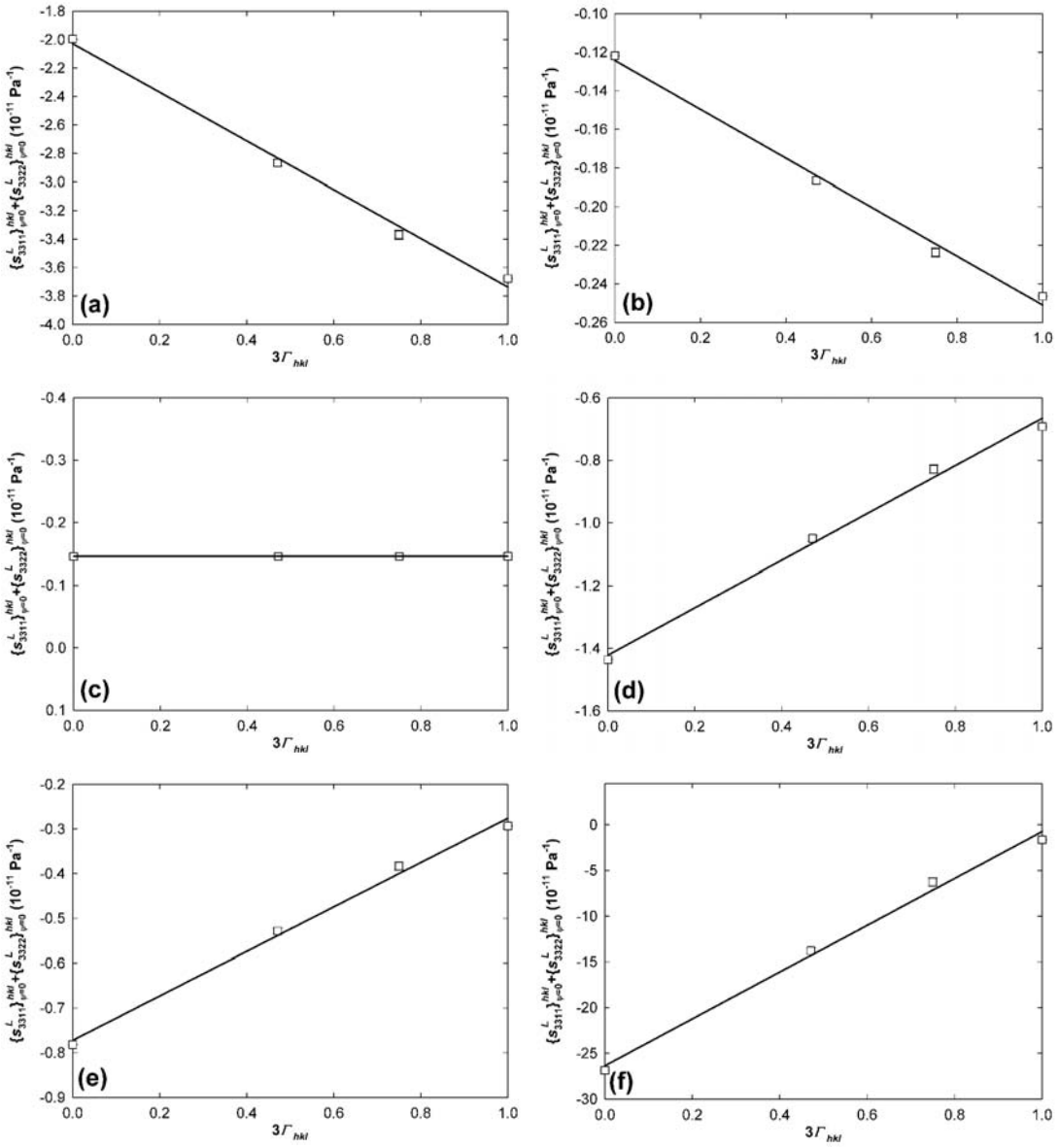

Figure 2.19: $3\Gamma_{hkl}$ plots for KCl (a), CrN (b), W (c), Au (d), Cu (e) and Na (f). The plots show the X-ray *compliance term* $\left\{S^L_{3311}\right\}^{hkl}_{\psi=0^\circ} + \left\{S^L_{3322}\right\}^{hkl}_{\psi=0^\circ}$ as a function of the corresponding X-ray anisotropy factor $3\Gamma_{hkl}$. The *compliance term* $\left\{S^L_{3311}\right\}^{hkl}_{\psi=0^\circ} + \left\{S^L_{3322}\right\}^{hkl}_{\psi=0^\circ}$ is determined from the intersections $\left\{\epsilon^L_{33}\right\}^{hkl}_{\psi=0^\circ}$ of the $\left\{\epsilon^L_{33}\right\}^{hkl}_{\psi} - \sin^2\psi$ plots (Figs. 2.10-2.18) at $\psi = 0^\circ$ according to Eq. 2.40. The intersections and there standard deviations are listed in tables 2.3 and 2.4. The standard deviations of the intersections are negligible (Hill model, Gaussian (111) fiber texture, $\psi_{\mathrm{FWHM}} = 10^\circ$, 10% ISO, 100 MPa equibiaxial stress, 311 reflex is not listed in Tables 2.5-2.4).

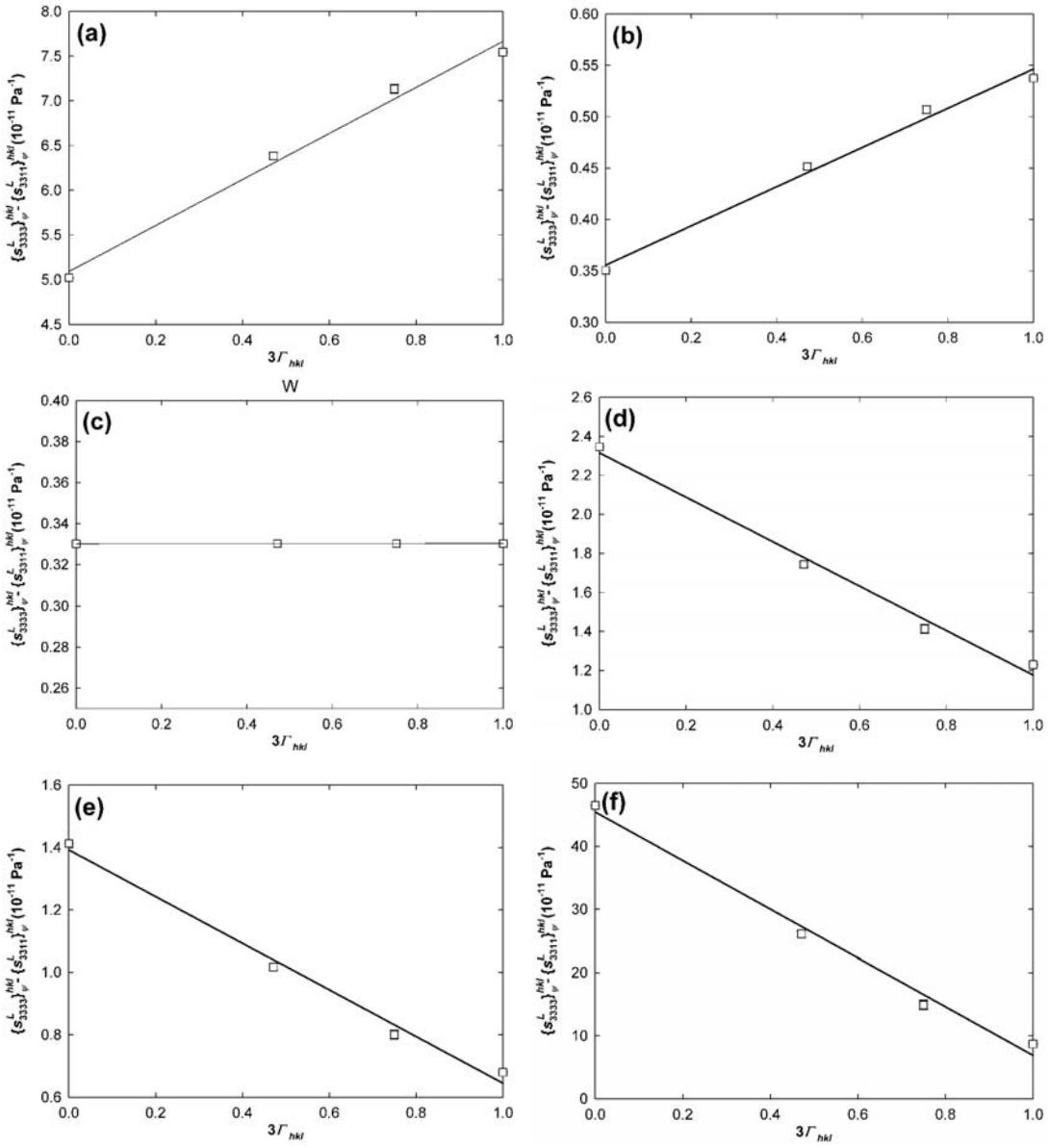

Figure 2.20: $3\Gamma_{hkl}$ plots for KCl (a), CrN (b), W (c), Au (d), Cu (e) and Na (f). The plots show the X-ray *compliance term* $\left\{S^L_{3333}\right\}^{hkl}_\psi - \left\{S^L_{3311}\right\}^{hkl}_\psi$ as a function of the corresponding X-ray anisotropy factor $3\Gamma_{hkl}$. The *compliance term* $\left\{S^L_{3333}\right\}^{hkl}_\psi - \left\{S^L_{3311}\right\}^{hkl}_\psi$ is determined from the averaged slopes of the $\left\{\epsilon^L_{33}\right\}^{hkl}_\psi - \sin^2\psi$ plots (Figs. 2.10-2.18) according to Eq. 2.41. The averaged slopes and there standard deviations are listed in tables 2.5 and 2.6. The standard deviations of the averaged slopes are negligible (Hill model, Gaussian (111) fiber texture, $\psi_{\mathrm{FWHM}} = 10°$, 10% ISO, 100 MPa equibiaxial stress, 311 reflex is not listed in Tables 2.5-2.4).

2.11 Correlation between X-ray elastic and mechanical elastic constants

This section shows that the calculated *mechanical* Young's modulus $\{E\}^{\mathrm{M}}$ always lies between the X-ray Young's moduli $\{E\}^{100}$ and $\{E\}^{111}$ even in the case of fiber textured materials. If the ZAR [76] is smaller than one, the Young's modulus in $\langle 100 \rangle$ direction is stronger than the Young's modulus in $\langle 111 \rangle$ direction. If the ZAR is greater than one, it is upside down.
The ODF of a (111) fiber textured material with $\psi_{\mathrm{FWHM}} = 10°$ and an ISO of 10% was calculated. The *mechanical* and X-ray elastic Young's moduli $\left\{E^L_{3333}\right\}^{\mathrm{M}}_{\psi}$, $\left\{E^L_{3333}\right\}^{100}_{\psi}$, $\left\{E^L_{3333}\right\}^{110}_{\psi}$, $\left\{E^L_{3333}\right\}^{311}_{\psi}$ and $\left\{E^L_{3333}\right\}^{111}_{\psi}$ are calculated according to Sec. 2.6 and 2.8 for the whole $\sin^2\psi$ range. The results cleary show that at $\psi = 0°$ for a (111) fiber textured material, the *mechanical* Young's modulus approaches the X-ray elastic modulus of the $\langle 111 \rangle$ reflex. At $\psi = 90°$ the *mechanical* Young's modulus equates to the X-ray elastic modulus of the (110) reflex. This result is evident due to the fact that all (111) crystallographic planes are in-plane isotropic. The in-plane isotropy of the (111) planes immidiately states that the Young's modulus of the planes normal to (111) must be independant of any anisotropy. Therefore the *mechanical* Young's modulus must approach the X-ray Young's modulus of the $(1\bar{1}0)$ planes.

It is predictable that for hexagonal systems possessing a (0001) fiber texture the *mechanical* Young's modulus at $\psi = 90°$ must equates the X-ray elastic Young's modulus of the $(10\bar{1}0)$ crystallographic reflex.

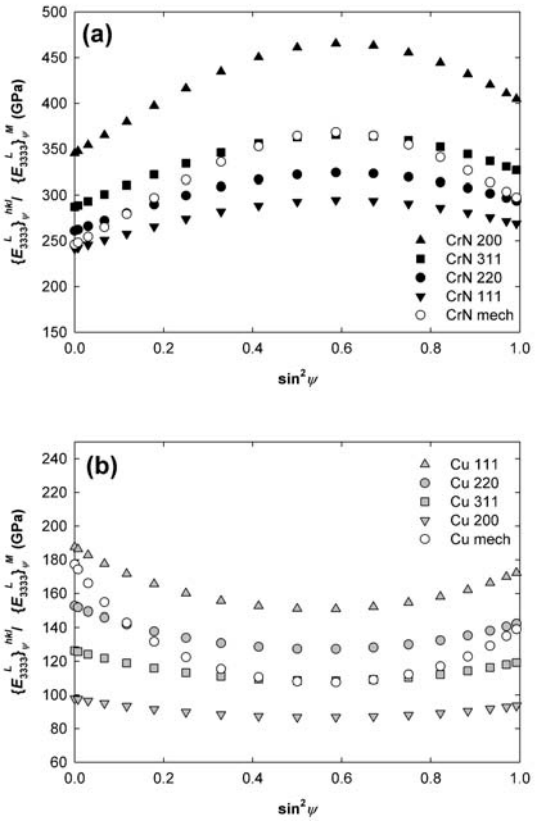

Figure 2.21: The figure shows the *mechanical* Young's moduls $\left\{E^L_{3333}\right\}^{\mathrm{M}}_{\psi}$ and the X-ray elastic moduli $\left\{E^L_{3333}\right\}^{hkl}_{\psi}$ over the whole $\sin^2\psi$ range of the two materials CrN (a) and Cu (b) for a (111) fiber texture with $\psi_{\mathrm{FWHM}} = 10^\circ$ and 10% ISO. The results cleary show that at $\psi = 0^\circ$ for a (111) fiber textured material, the *mechanical* Young's modulus approaches the X-ray elastic modulus of the (111) reflex. At $\psi = 90^\circ$ the *mechanical* Young's modulus equates to the X-ray elastic modulus of the (110) reflex. This result is evident due to the fact that all (111) crystallographic planes are in-plane isotropic. The in-plane isotropy of the (111) planes immidiately states that the *mechanical* Young's modulus of the planes normal to (111) must be independant of any anisotropy. Therefore the *mechanical* Young's modulus must approach the X-ray Young's modulus of the $(1\bar{1}0)$ planes.

2.12 The $3\Gamma^*_{hkl} - 3\Gamma_{uvw}$ plot

In Sec. 2.10 it was shown that the X-ray elastic *compliance terms* can be plotted as a function of the X-ray anisotropy factor $3\Gamma_{hkl}$. Due to the fact that for a single crystal the X-ray and mechanical *compliance terms* are equal within the $3\Gamma_{hkl}$ domain $[0, 1]$ (see Sec. 2.10) the averaged mechanical *compliance term* of a polycrystal must also lie in between the $3\Gamma_{hkl}$ domain $[0, 1]$. On the one hand, the mechanical elastic *compliance term* can be extracted from the ordinate of the $3\Gamma_{hkl}$ plot (see Sec. 2.10) if, and only if, the correct value on the abscissa, which will further be denoted as $3\Gamma^*_{hkl}$, is known. According to the Reuss grain interaction model, $3\Gamma^*_{hkl}$ depends on the texture parameter

$$\Gamma_{uvw} = \frac{u^2v^2 + v^2w^2 + w^2u^2}{(u^2 + v^2 + w^2)^2} \tag{2.60}$$

on ψ_{FWHM} and on ISO. On the other hand it is possible to determine $3\Gamma^*_{hkl}$ if the mechanical *compliance term* for a texture $3\Gamma_{uvw}$ with ψ_{FWHM} and ISO can be calculated. A parallel line to the abscissa of the corresponding $3\Gamma_{hkl}$ plot (see Sec. 2.10) at the magnitude of the calculated mechanical *compliance term* is subtended with the corresponding $3\Gamma_{hkl}$ plot. The $3\Gamma_{hkl}$ of the intersection point is then the correct $3\Gamma^*_{hkl}$ value. This procedure can be performed for multiple textures $3\Gamma_{uvw}$ of different ψ_{FWHM} and ISOs. Figs. 2.22 and 2.23 show the calculated $3\Gamma^*_{hkl} - 3\Gamma_{uvw}$ plots for the $\left\{S^L_{3333}\right\}_{\psi=0^\circ}$ *compliance term* with varying ISO and ψ_{FWHM}, respectively. Interestingly, the $3\Gamma^*_{hkl} - 3\Gamma_{uvw}$ plots do not depend on the ZAR [76] or the material for the $\left\{S^L_{3333}\right\}_{\psi=0^\circ}$ *compliance term*. Therefore the plots in Figs. 2.22 and 2.23 represent a kind of *universal plot* for cubic materials. The procedure to calculate any $3\Gamma^*_{hkl} - 3\Gamma_{uvw}$ plot is summarized in the following list

- Calculate (simulation) / determine (experiment) the ODF of the sample.
- Calculate $3\Gamma_{uvw}$.
- Choose the grain interaction model.
- Choose a ψ angle.
- Choose any *compliance term* (see Sec. 2.10).
- Calculate the mechanical elastic compliance tensor components $\left\{S^L_{mnop}\right\}^{\mathrm{M}}_{\psi}$ according to the grain interaction model.
- Extract the *compliance term* from the transformed tensor components $\left\{S^L_{mnop}\right\}^{\mathrm{M}}_{\psi}$ in the L coordinate system.
- Calculate the X-ray elastic compliance tensor components $\left\{S^L_{mnop}\right\}^{hkl}_{\psi}$ for at least two reflexes (hkl) with different values of $3\Gamma_{hkl}$ according to the grain interaction model in respect to the laboratory coordinate system L.

- Plot the $3\Gamma_{hkl}$ plot for the chosen *compliance term*.
- Fit the data in the $3\Gamma_{hkl}$ plot.
- Find the $3\Gamma^*_{hkl}$ value in the $3\Gamma_{hkl}$ plot which correlates with the *compliance term* from the mechanical compliance tensor.
- Repeat the procedure for n ODFs with different fiber textures (uvw), ψ_{FWHM} and ISOs and plot the corresponding $3\Gamma^*_{uvw,i}$ vs. $3\Gamma_{hkl,i}$ for i=1..n.

In order to express the dependence of $3\Gamma^*_{hkl}$ plot on the $3\Gamma_{uvw}$, on ψ_{FWHM} and on ISO generally and in a "user-friendly way", the following empirical equation was derived [77]

$$3\Gamma^*_{hkl} = A + 3\Gamma_{uvw}(1 - \frac{A}{0.6}) \tag{2.61}$$

where $A = (\psi_{\mathrm{FWHM}} * 8.8 + \mathrm{ISO} * 5.8 - \psi_{\mathrm{FWHM}} * \mathrm{ISO} * 0.083)/1000$.

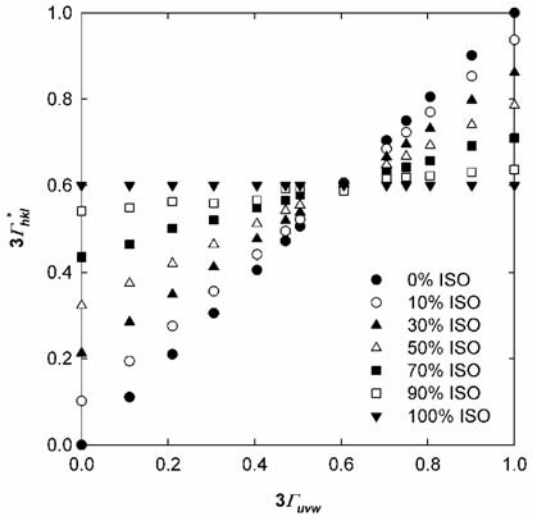

Figure 2.22: The picture shows the $3\Gamma^*_{hkl} - 3\Gamma_{uvw}$ plot of the $\left\{S^L_{3333}\right\}^{\mathrm{M}}_{\psi}$ tensor component. The plot was calculated using the Hill model, $\psi_{\mathrm{FWHM}} = 10^\circ$ and variational ISO. For ISO=100%, *i.e.* an isotropic sample, the $3\Gamma^*_{hkl}$ is equal to 0.6 for all $3\Gamma_{uvw}$ values. The graph for ISO=0% clearly shows that $3\Gamma^*_{hkl} = 3\Gamma_{uvw}$ for all fiber axes (uvw). This result states that for a perfect (uvw) fiber texture the mechanical elastic constant $\left\{S^L_{3333}\right\}^{\mathrm{M}}_{\psi}$ can directly be calculated from the X-ray elastic constants of the (hkl) reflex. Moreover all graphs intersect at a pivot point of $3\Gamma^*_{hkl} = 3\Gamma_{uvw} = 0.6$. It was shown by [75] that $3\Gamma^*_{hkl} = 0.6$ corresponds to the X-ray elastic constants of the crystallographic reflex (hkl) which directly correlate with the mechanical elastic constants in the isotropic case. The $3\Gamma^*_{hkl} - 3\Gamma_{uvw}$ is not a function of the ZAR [76] or the material.

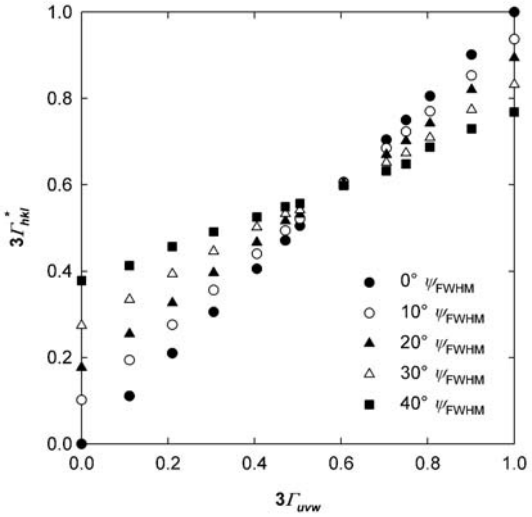

Figure 2.23: The picture shows the $3\Gamma^*_{hkl} - 3\Gamma_{uvw}$ plot of the $\left\{S^L_{3333}\right\}^{\mathrm{M}}_{\psi}$ tensor component. The plot was calculated using the Hill model, ISO 10% and variational ψ_{FWHM}. The graph for $\psi_{\mathrm{FWHM}} = 0^\circ$ clearly shows that $3\Gamma^*_{hkl} = 3\Gamma_{uvw}$ for all fiber axes (uvw). This result states that for a perfect (uvw) fiber texture the mechanical elastic constant $\left\{S^L_{3333}\right\}^{\mathrm{M}}_{\psi}$ can directly be calculated from the X-ray elastic constants of the (hkl) reflex. Moreover all graphs intersect at a pivot point of $3\Gamma^*_{hkl} = 3\Gamma_{uvw} = 0.6$. It was shown by [75] that $3\Gamma^*_{hkl} = 0.6$ corresponds to the X-ray elastic constants of the crystallographic reflex (hkl) which directly correlate with the mechanical elastic constants in the isotropic case. The $3\Gamma^*_{hkl} - 3\Gamma_{uvw}$ is not a function of the ZAR [76] or the material.

2.13 Determination of mechanical elastic constants

According to Sec. 2.10 and 2.12 it is possible to extract any *mechanical compliance term* from the $3\Gamma_{hkl}$ plot if the correct $3\Gamma^*_{hkl}$ is known. The value $3\Gamma^*_{hkl}$ can be determined from the $3\Gamma^*_{hkl} - 3\Gamma_{uvw}$ plot or from the analytical formula (Eq. 2.61). Although the three X-ray compliance tensor components $\left\{S^L_{3311}\right\}^{hkl}_{\psi}$, $\left\{S^L_{3322}\right\}^{hkl}_{\psi}$ and $\left\{S^L_{3333}\right\}^{hkl}_{\psi}$ are directly plotable as a function of $3\Gamma_{hkl}$ when performing simulations, not all of them can be determined experimentally from a single measurement. The reason is that the slope and intersection in Eq. 2.38 are *compliance terms* of these three X-ray compliance tensor components. First, the correct $3\Gamma^*_{hkl}$ value has to be extracted from the corresponding $3\Gamma^*_{hkl} - 3\Gamma_{uvw}$ plot or from Eq. 2.61. The calculation of the mechanical elastic constants will be described in detail.

- The $3\Gamma_{hkl}$ plot for the *compliance term* $\left\{S^L_{3311}\right\}^{hkl}_{\psi=0^\circ} + \left\{S^L_{3322}\right\}^{hkl}_{\psi=0^\circ}$ is calculated using the intersection data from the $\sin^2\psi$ plots at $\psi = 90^\circ$ (Eq. 2.40) at $\psi = 0^\circ$. Then the $3\Gamma^*_{hkl}$ value is used to extract $\left\{S^L_{3311}\right\}^{3\Gamma^*_{hkl}}_{\psi=0^\circ} + \left\{S^L_{3322}\right\}^{3\Gamma^*_{hkl}}_{\psi=0^\circ}$. Using Eq. 2.40 $\left\{S^L_{3311}\right\}^{3\Gamma^*_{hkl}}_{\psi=0^\circ}$ can be determined, which satisifies Eq. 2.62

$$\left\{S^L_{3311}\right\}^{3\Gamma^*_{hkl}}_{\psi=0^\circ} = \left\{S^S_{3311}\right\}^{\mathrm{M}} \tag{2.62}$$

- The $3\Gamma_{hkl}$ plot for the *compliance term* $\left\{S^L_{3333}\right\}^{hkl}_{\psi} - \left\{S^L_{3311}\right\}^{hkl}_{\psi}$ is calculated using the averaged slope data from the $\sin^2\psi$ plots (Eq. 2.41). Then the $3\Gamma^*_{hkl}$ value is used to obtain

$$\left\{S^L_{3333}\right\}^{3\Gamma^*_{hkl}}_{\psi} - \left\{S^L_{3311}\right\}^{3\Gamma^*_{hkl}}_{\psi} = \left\{S^S_{3333}\right\}^{\mathrm{M}} - \left\{S^S_{3311}\right\}^{\mathrm{M}} \tag{2.63}$$

  Substitution of Eq. 2.62 in Eq. 2.63 is used to determine

$$\left\{S^L_{3333}\right\}^{3\Gamma^*_{hkl}}_{\psi=0^\circ} = \left\{S^S_{3333}\right\}^{\mathrm{M}} \tag{2.64}$$

  Then Eq. 2.64 can be used to calculate

$$\left\{E^S_{3333}\right\}^{\mathrm{M}} = \frac{1}{\left\{S^S_{3333}\right\}^{\mathrm{M}}} \tag{2.65}$$

  which is the *mechanical out-of-plane* Young's modulus.

- The $3\Gamma_{hkl}$ plot for the *compliance term* $\left\{S^L_{3322}\right\}^{hkl}_{\psi=90^\circ} + \left\{S^L_{3333}\right\}^{hkl}_{\psi=90^\circ}$ is calculated using the intersection data from the $\sin^2\psi$ plots (Eq. 2.45) at $\psi = 0^\circ$. Then the $3\Gamma^*_{hkl}$ value is used to determine

$$\left\{S^L_{3322}\right\}^{3\Gamma^*_{hkl}}_{\psi=90^\circ} + \left\{S^L_{3333}\right\}^{3\Gamma^*_{hkl}}_{\psi=90^\circ} = \left\{S^L_{1122}\right\}^{\mathrm{M}}_{\psi=0^\circ} + \left\{S^L_{1111}\right\}^{\mathrm{M}}_{\psi=0^\circ} \tag{2.66}$$

Eq. 2.66 can be used to calculate the *mechanical in-plane* biaxial modulus

$$\left\{\mathrm{M}^{S}\right\}^{\mathrm{M}} = \frac{1}{\left\{S^{L}_{1111}\right\}^{\mathrm{M}}_{\psi=0^\circ} + \left\{S^{L}_{1122}\right\}^{\mathrm{M}}_{\psi=0^\circ}} \tag{2.67}$$

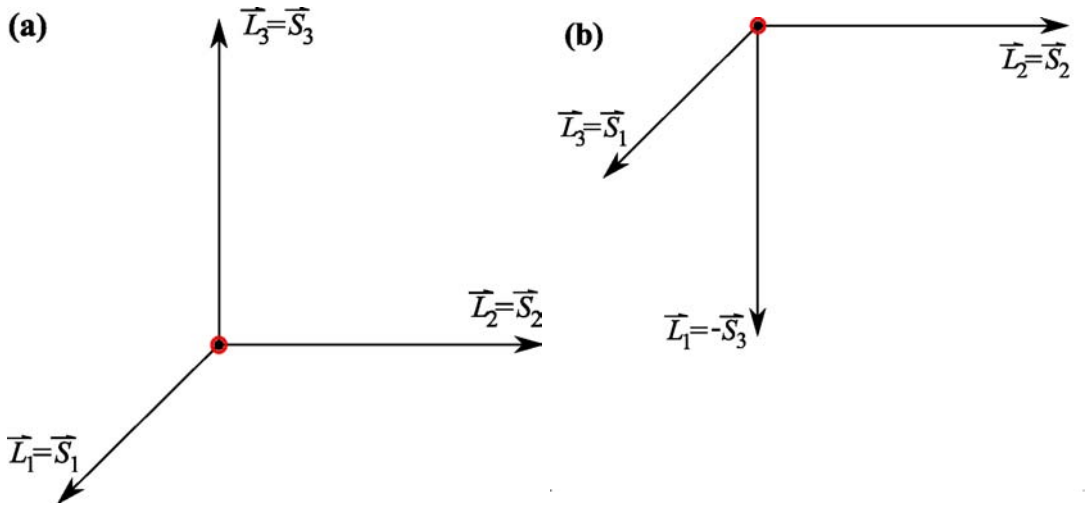

Figure 2.24: The figure shows the laboratory coordinate system L relative to the sample coordinate system S at $\psi = 0^\circ$ (a) and $\psi = 90^\circ$ (b), respectively. If the L and S systems are congruent, $\left\{S^{L}_{mnop}\right\} = \left\{S^{S}_{mnop}\right\}$ (a). If the L and S systems are not congruent (b), the tensor indices of the L system have to be substituted according to $1 \rightarrow 3$, $2 \rightarrow 2$ and $3 \rightarrow 1$ to get the compliance tensor notation in respect to S. The two coordinate systems are plotted side by side to improve comprehension of the two possible rotational positions. The mark at the centre of the two coordinate system defines the common point of rotation. In mind, the two coordinate systems should be aligned together at this point.

3 Experimental methods

3.1 Sample preparation

As a substrate for specimen preparation, rectangular Si(100) wafers with the dimension of 30x8 mm^2 and different thicknesses were used. The wavers were cleaned in an ultrasonic cleaner using isopropanol and acetone. All used materials were deposited with balanced magnetron sputtering in argon atmosphere. Moreover, ion etching was applied before the deposition to remove contaminates from the surface.

The CrN and TiN thin films were produced in Ar+N_2 atmosphere with a total pressure of 1 Pa and a partial pressure of 0.25 Pa for N_2. The power of the magnetron system was 6 kW for CrN and 0.4 kW for TiN. The BIAS voltage was -80 V and -50 V for CrN and TiN, respectively. The substrate temperature was 550 °C.

The Cu samples were deposited in Ar atmosphere at room temperature. After the deposition process the samples were annealed in N_2 atmosphere at 400 °C for 10 min in order to increase the residual stress magnitude in the films [78]. Main deposition parameters are listed in Tab. 3.1.

Table 3.1: List of materials used for determination of mechanical elastic constants. p_t is the total pressure. $p_p^{N_2}$ is the N_2 partial pressure for the nitride samples. V_{BIAS}, T_d, T_a and P are the BIAS voltage, the deposition temperature, the annealing temperature and the power of the magnetron system, respectively.

Material	p_t	$p_p^{N_2}$	V_{BIAS}	T_d	T_a	P
	(V)	(Pa)	(Pa)	(°C)	(°C)	(kW)
Cu	1	-	-80	RT	400	-
CrN	1	0.25	-80	350	-	6.0
TiN	1	0.25	-50	550	-	0.4

3.2 Elastic strain characterization using $\sin^2\psi$ technique

X-ray diffraction (XRD) is widely used to determine (X-ray) strains in crystalline materials. For this purpose, the $\sin^2\psi$ method is applied. According to [26] the X-ray elastic strain is direct proportional to the slope in the $\sin^2\psi$ dependence. The lattice spacing $d^{hkl}_{\phi,\psi}$ is determined at different polar angles ψ and azimuthal angles ϕ. If the unstressed lattice spacing d_0 is known it is possible to calculate the X-ray strain according to Eq. 3.1

$$\left\{\epsilon^L_{33}\right\}^{hkl}_{\phi,\psi} = \frac{d^{hkl}_{\phi,\psi} - d_0}{d_0} \tag{3.1}$$

where $\left\{\epsilon^L_{33}\right\}^{hkl}_{\phi,\psi}$ depends on the crystallographic reflex *hkl* [26]. The mathematical correlation between the lattice spacing $d^{hkl}_{\phi,\psi}$ and the lattice parameter a for cubic materials is [26]

$$a = d^{hkl}_{\phi,\psi}\sqrt{h^2+k^2+l^2} \tag{3.2}$$

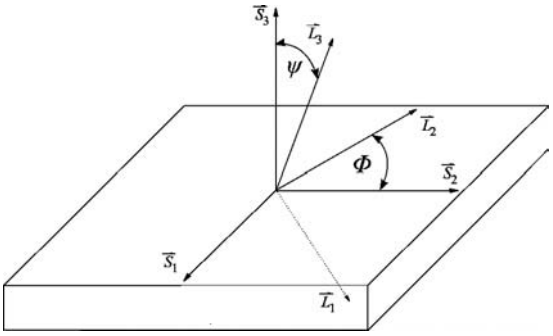

Figure 3.1: A definition of two coordinate systems used for the characterization of *mechanical in-plane* elastic strains using $\sin^2\psi$ method: sample system S, laboratory system L [26]. The X-ray elastic strain along the direction $\vec{L}_3$ (which is parallel to the diffraction vector $\vec{g}$) is characterized by measuring the reflection *hkl*. The orientation of the vector $\vec{g}$ with respect to $\vec{S}_i$ is defined by the angles ϕ and ψ.

However, the linear dependence between the X-ray strain $\left\{\epsilon^L_{33}\right\}^{hkl}_{\phi,\psi}$ and $\sin^2\psi$ strictly holds only for materials with crystal isotropy, macroscopical quasi isotropy, materials with Voigt grain-interaction [57] and simplified stress states. The X-ray strain $\left\{\epsilon^L_{33}\right\}^{hkl}_{\phi,\psi}$ for a fiber textured thin film obeying Hill grain interaction model and an equibiaxial stress state can be described using Eq. 2.38. This formula was first proposed by [70] to describe the X-ray strain of bulk materials possessing a strong surface anisotropy. There is an addition term $\sin 2\psi$ in Eq. 2.38. Therefore all methods which use Eq. 2.38 to characterize the X-ray strain are called *modified* $\sin^2\psi$ methods [70].
All measurements were performed in laboratory conditions using a Seifert 3000 PTS four-circle diffractometer. The setup comprised Cu K_α radiation, polycapillary optics on the primary side, Soller slits, a graphite monochromator and a scintillation detector

on the secondary side. The average beam diameter was about 3x3 mm^2 for strain measurements. The relatively large beam in the case of strain measurements enabled to assess volume-averaged properties. The limited pole figure characterization was performed using Schultz reflectivity technique with the beam of 3 mm in diameter whereby the ψ range was set to 0-80 degrees.

3.3 X-ray curvature method

The bending of the substrate can be measured capacitively, inductively, electromechanically, or optically by laser-beam deflection systems [79, 80]. In semiconductor industry X-rays were widely used to revise the waviness of the substrates [54]. The idea behind the X-ray curvature technique relies on the possibility to determine the curvature of a thin film-single crystal substrate directly by X-rays. Rocking curve scans of Si(400) reflexes are performed at different sample positions x_i. The detector is moved and fixed at the 2θ position of the Si(100) reflex. For each sample position x_i the sample is rotated around the ω^{x_i} axis to perform an ω-scan. The peak of the ω^{x_i}-scan is fitted to determine the exact $\omega_0^{x_i}$ position. This procedure is repeated for different sample positions x_i. The relative changes Δx_i and $\Delta\omega_i$ are calculated. According to [78] the curvature radius can be determined from the slope of $\Delta\omega_i$ vs. Δx_i

$$R = \left(\frac{\Delta\omega_i}{\Delta x_i}\right)^{-1} \tag{3.3}$$

Fig. 3.2 shows the principle of this method.

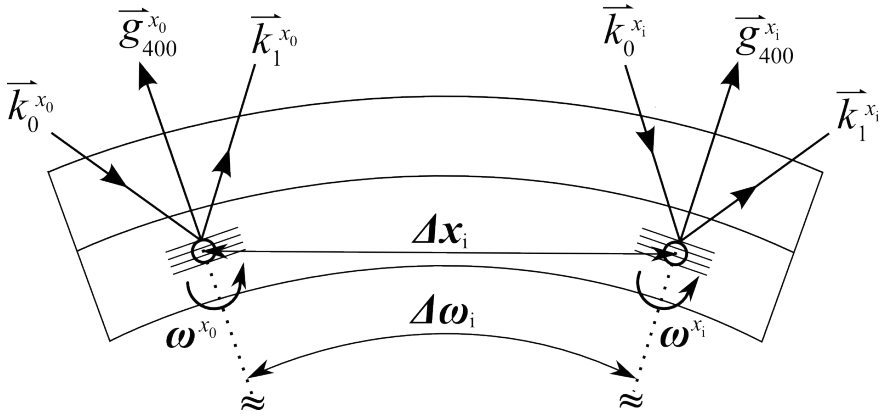

Figure 3.2: This schematic description shows the diffraction setup used to determine the curvature. $\vec{k}_0^{\,x_j}$ and $\vec{k}_1^{\,x_j}$ are the primary and secondary beam at a definite position x_j. The vector $\vec{g}_{400}^{\,x_j}$ is the scattering vector which is normal to the planes of diffraction.

The determined curvature radius R can then be used in the Stoney formula [24, 53] to calculate the absolute macroscopic equibiaxial stress.

$$\sigma = \frac{E}{6(1-\nu)}\frac{h_s^2}{h_f}\frac{1}{R} \tag{3.4}$$

The failure of the calculated stress depends on the standard deviations of the substrate thickness Δh_s^2, the film thickness $\Delta \frac{1}{h_f}$ and the curvature $\Delta \frac{1}{R}$. The film thicknesses of the samples used in this thesis were measured with scanning electron microscopes (SEM) and their standard deviations are assumed to be zero. Therefore the standard deviation of the stress in Eq. 3.4 can be written as

$$\Delta\sigma = \frac{E}{6(1-\nu)} \frac{h_s^2}{h_f} \frac{1}{R^2} \Delta R \tag{3.5}$$

3.4 Texture analysis

Texture analysis was performed in laboratory using a four circle Seifert PTS 3000 diffractometer. All measurements were performed with a parallel polycapillary on the primary side. The secondary side was equipped with Soller slits of a 2° divergence followed by a graphite monochromator. A scintillation detector was used to collect the diffracted intensity at the fixed 2θ position of the measured pole figure. The azimuthal ϕ angle and the polar ψ angle were named α and β, respectively. All texture measurements were performed with the detector fixed at 2θ position of the corresponding crystallographic reflex of the pole figure (Tab. 3.2). The step size of α and β was 5°. The measurements were performed in equal area mode.

Table 3.2: 2θ positions of Cu, CrN and TiN reflections calculated from the unstressed lattice parameters (Tab. 2.2) using CuK_α wavelength. All three materials belong to the same space group F4/m$\bar{3}$2/m with space group number 225. The 2θ values are calculated according to the unstressed lattice parameters found in Tab. 2.2.

Material	111	200	220	311
Cu	43.32	50.45	74.13	89.94
CrN	37.37	43.42	63.08	75.67
TiN	36.65	42.58	61.78	74.04

Annealed, unstressed Au and Cu powders were used to acquire defocusation data for Cu, CrN and TiN. The change in intensity for the first four crystallographic reflexes of Cu and Au was measured as a function of polar angle ψ. The resolution of the ψ scan was 5°. The intensity values were prepared for and saved in the format of LaboTex [65] defocusation file (file extension .COR). The defocusation file was used to correct the intensities of the measured pole figures. Cu pole figures were corrected with the Cu defocusation file. CrN and TiN pole figures were corrected with the Au defocusation file.

4 Results and discussion

4.1 Cu sample

The first sample is a 0.6 μm thick Cu thin film deposited onto a 140 μm thick Si(100) substrate. The procedure to determine the substrate curvature is described in Sec. 3.3. The curvature was 3.572 m, the corresponding stress value was about 275.9 MPa. A dominant (111) fiber texture was found (Fig. 4.2). The ISO and ψ_{FWHM} were 10% and 14°, respectively. Moreover, the X-ray strains $\left\{\epsilon_{33}^{L}\right\}_{\psi}^{hkl}$ as a function of $\sin^2\psi$ for multiple reflexes were measured. Altogether six crystallographic reflexes could be found in the 2θ range of the Cu sample. The X-ray strains of four representative crystallographic refelexes are plotted in Fig. 4.3a-d. The $\left\{\epsilon_{33}^{L}\right\}_{\psi}^{hkl} - \sin^2\psi$ relation is nearly linear for all reflexes *hkl*. The Cu sample possesses a (111) fiber texture, *i.e.* $3\Gamma_{uvw} = 1.0$. The corresponding $3\Gamma_{hkl}^{*}$ value is therefore 0.89 (Eq. 2.61). The $3\Gamma_{hkl}^{*}$ value is used to determine the *mechanical compliances* from Figs. 4.4a-c. The *mechanical out-of-plane* Young's modulus $\left\{E_{3333}^{S}\right\}^{\mathrm{M}}$, the Poisson's ratio $\left\{\nu_{3311}^{S}\right\}^{\mathrm{M}}$ and the *mechanical in-plane* biaxial modulus $\left\{M^{S}\right\}^{\mathrm{M}}$ are 169.40 GPa, 0.23 and 223.3 GPa, respectively. *Calculated* and *experimental* data are listed in Tab. 4.1.

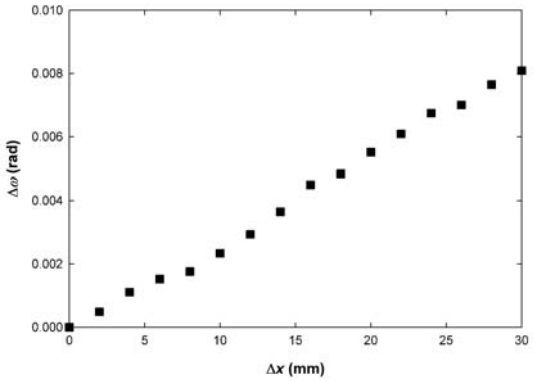

Figure 4.1: The plot of $\Delta\omega$ vs. Δx (Sec. 3.3). The curvature is 3.572 m. The Cu thickness and the Si(100) substrate thickness were 0.60 μm and 140 μm, respectively. The equibiaxial stress is 275.9 MPa and was calculated according to Eq. 3.4.

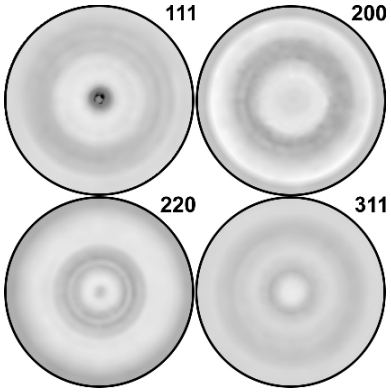

Figure 4.2: This figure shows the pole figures of the Cu sample. The detector of the diffractometer was fixed at the 2θ positions of the corresponding crystallographic reflexes listed in Tab. 3.2. The angular resolution in α and β space was 5°. The pole figures were measured in equal area mode with a counting time of 2 s. The background was automatically subtracted by the measurement software. The pole figures were measured with a Seifert PTS 3000.

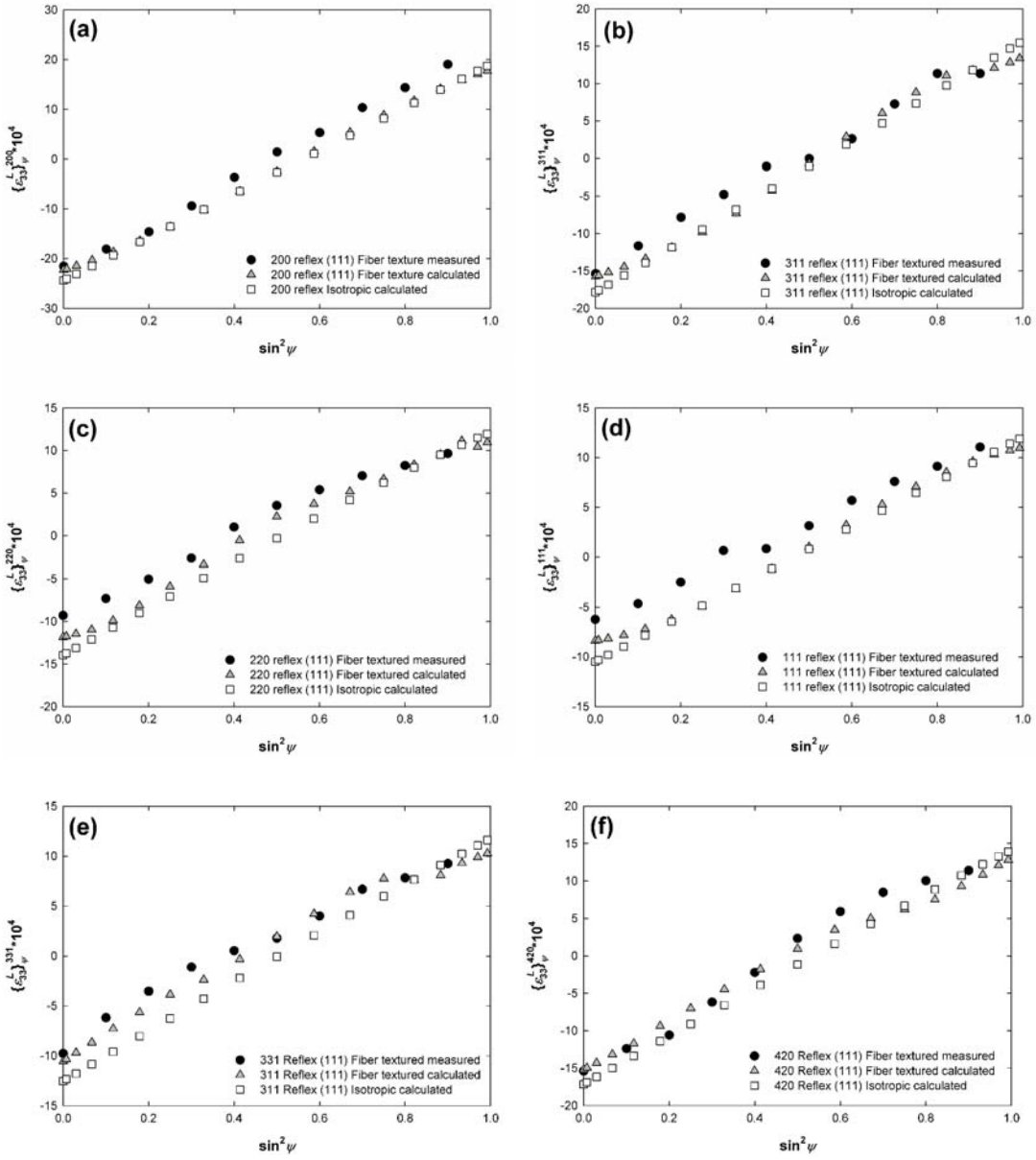

Figure 4.3: The figures (a)-(f) show the X-ray strain of six representative crystallographic reflexes of a (111) fiber textured Cu sample as a function of $\sin^2\psi$. The black circled data points represent the *experimental* data. The X-ray strain was determined from the $\{d\}_{\psi}^{hkl}$ values according to Eq. 3.1 using a lattice free parameter $a_0 = 3.6149$ [66]. The gray triangled (white squared) points represent the calculated X-ray strain for the fiber textured (isotropic) case. The *experimental* determined stress value of 275.9 MPa was used for the calculation. The equibiaxial stress of the Cu sample was determined using X-ray curvature method described in Cha. 3.3. A fiber textured (isotropic) ODF with an angular resolution of 5° was used. It is evident, that for the four crystallographic reflexes (200),(311),(220) and (111) the calculated fiber textured (isotropic) strain data does not match the measured strain data exactly but the calculated slopes of all data are comparable. Moreover, the intersections are comparable. It must be mentioned that an incorrect value of a_0 can shift the strain slopes to higher or lower strain values and can therefore change the correct intersection values.

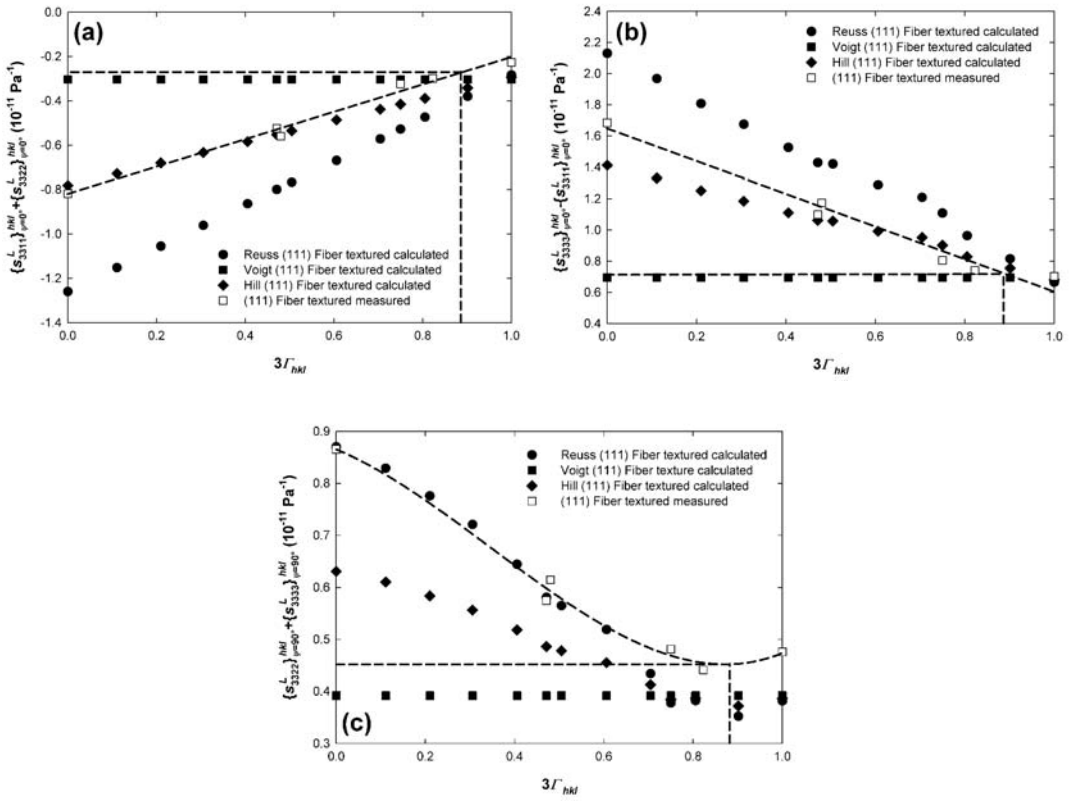

Figure 4.4: The figures (a)-(c) show calculated and measured *compliance terms* as a function of $3\Gamma_{hkl}$. The *compliance terms* for Reuss, Voigt and Hill were calculated for a (111) fiber textured Cu sample with ISO and ψ_{FWHM} of 10% and 14°, respectively. The resolution of the ODF was 5°. The white squared data points were calculated from the slopes and intersections of the $\left\{\epsilon_{33}^{L}\right\}_{\psi}^{hkl} - \sin^2\psi$ plots in Fig. 4.3a-d. At $\psi = 0°$, the X-ray elastic constant $2\{s_1\}_{\psi=0°}^{hkl}$ (Eq. 2.40) is equal to $\left\{S_{3311}^{L}\right\}_{\psi=0°}^{hkl} + \left\{S_{3322}^{L}\right\}_{\psi=0°}^{hkl}$ (a). For textured materials this relation only holds at $\psi = 0°$. $2\{s_1\}_{\psi=0°}^{hkl}$ can be calculated from the intersection of the corresponding $\left\{\epsilon_{33}^{L}\right\}_{\psi}^{hkl} - \sin^2\psi$ plot at $\psi = 0°$. The *compliance term* $\left\{S_{3333}^{L}\right\}_{\psi=0°}^{hkl} - \left\{S_{3311}^{L}\right\}_{\psi=0°}^{hkl}$ can be determined from the slope of the corresponding $\left\{\epsilon_{33}^{L}\right\}_{\psi}^{hkl} - \sin^2\psi$ plot. Due to the fact that the averaged slope of $\left\{\epsilon_{33}^{L}\right\}_{\psi}^{hkl} - \sin^2\psi$ plot is considered, this equation holds for the whole $\sin^2\psi$-range. At $\psi = 90°$, the *compliance term* $\left\{S_{3322}^{L}\right\}_{\psi=90°}^{hkl} + \left\{S_{3333}^{L}\right\}_{\psi=90°}^{hkl}$ correlates to the intersection of the corresponding $\left\{\epsilon_{33}^{L}\right\}_{\psi}^{hkl} - \sin^2\psi$ plot at $\psi = 90°$. The figures clearly show that the measured data points are in good agreement with the calculated Hill data. It is unclear why the *experimental* data equals the Reuss calculated data at $\psi = 90°$, instead of the Hill calculated data. The *mechanical out-of-plane* Young's modulus $\left\{E_{3333}^{S}\right\}^{\mathrm{M}}$, the Poisson's ratio $\left\{\nu_{3311}^{S}\right\}^{\mathrm{M}}$ and the *mechanical in-plane* biaxial modulus $\left\{M^{S}\right\}^{\mathrm{M}}$ are 169.40 GPa, 0.23 and 223.3 GPa, respectively. *Calculated* and *experimental* data are listed in Tab. 4.1.

4.2 CrN sample

The second sample is a 2.43 μm thick CrN thin film deposited onto a 500 μm thick Si(100) substrate. The curvature was -2.193 m, the corresponding stress value was about -1415 MPa. A dominant (311) fiber texture was found (Fig. 4.6). The ISO and ψ_{FWHM} were 13% and 12°, respectively. Moreover, the X-ray strains $\left\{\epsilon_{33}^{L}\right\}_{\psi}^{hkl}$ as a function of $\sin^2\psi$ for multiple reflexes were measured. Altogether four crystallographic reflexes could be found in the 2θ range of the CrN sample. The X-ray strains are plotted in Fig. 4.7a-d. The $\left\{\epsilon_{33}^{L}\right\}_{\psi}^{hkl} - \sin^2\psi$ relation is extremly non-linear for all reflexes *hkl*. This can be a result of stress gradients [12], complex stress states [26] or macroscopic elastic anisotropy (texture). The CrN sample possesses a (311) fiber texture, *i.e.* $3\Gamma_{uvw} = 0.47$. The corresponding $3\Gamma_{hkl}^{*}$ value is therefore 0.51 (Eq. 2.61). The $3\Gamma_{hkl}^{*}$ value is used to determine the *mechanical compliances* from Figs. 4.8a,b and c. The *mechanical out-of-plane* Young's modulus $\left\{E_{3333}^{S}\right\}^{\mathrm{M}}$, the Poisson's ratio $\left\{\nu_{3311}^{S}\right\}^{\mathrm{M}}$ and the *mechanical in-plane* biaxial modulus $\left\{M^{S}\right\}^{\mathrm{M}}$ are 240.79 GPa, 0.16 and 344.8 GPa, respectively. *Calculated* and *experimental* data are listed in Tab. 4.2.

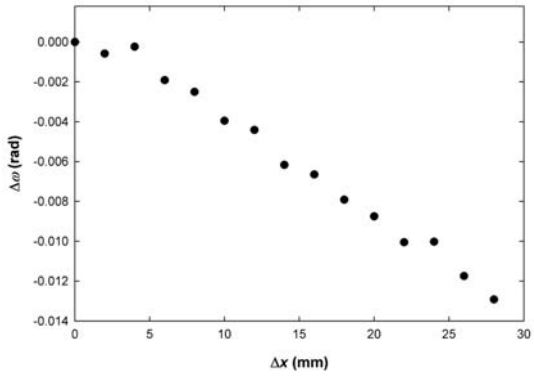

Figure 4.5: The plot of $\Delta\omega$ vs. Δx (Sec. 3.3). The curvature is -2.193 m. The CrN thickness and the Si(100) substrate thickness were 2.43 μm and 500 μm, respectively. The equibiaxial stress is -1415 MPa and was calculated according to Eq. 3.4.

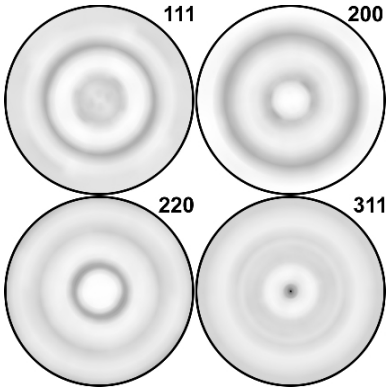

Figure 4.6: This figure shows the pole figures of the CrN sample. The detector of the diffractometer was fixed at the 2θ positions of the corresponding crystallographic reflexes listed in Tab. 3.2. The angular resolution in α and β space was 5°. The pole figures were measured in equal area mode with a counting time of 2 s. The background was automatically subtracted by the measurement software. The pole figures were measured with a Seifert PTS 3000. A (311) fiber was found and used for the calculation.

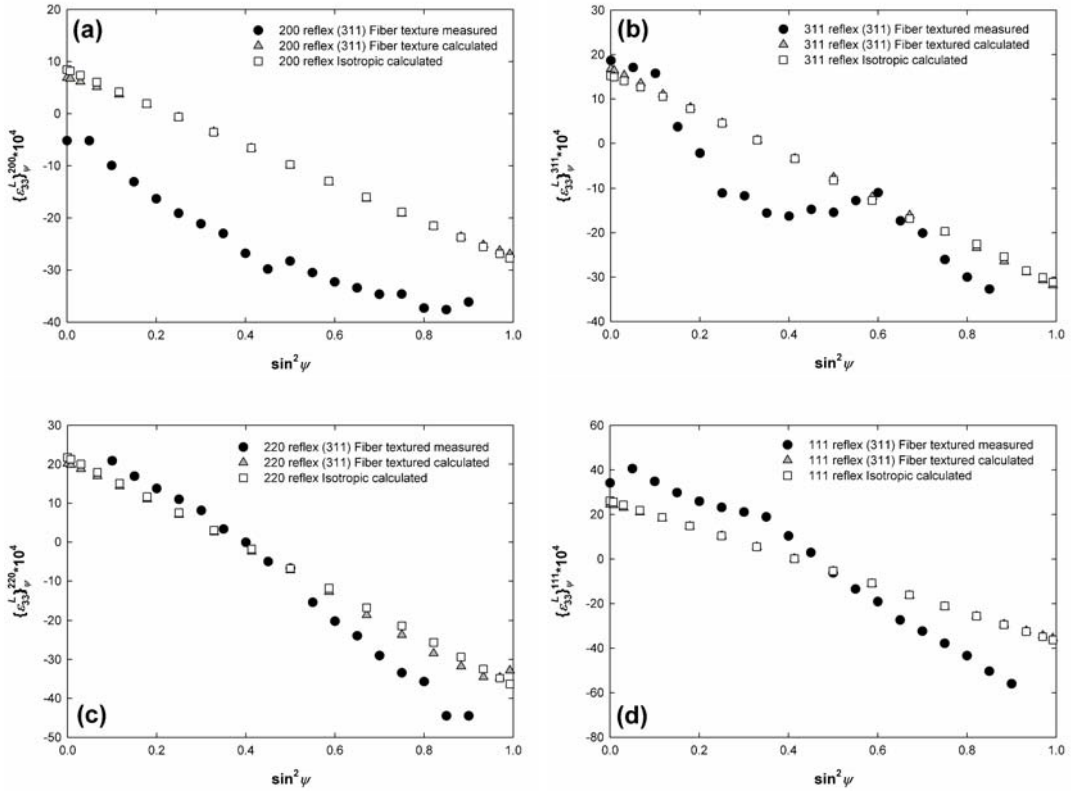

Figure 4.7: The figures (a)-(d) show the X-ray strain of four crystallographic reflexes of a (311) fiber textured CrN sample as a function of $\sin^2\psi$. The black circled data points represent the *experimental* data. The X-ray strain was determined from the $\{d\}_{\psi}^{hkl}$ values according to Eq. 3.1 using a lattice free parameter $a_0 = 4.1650$ [67]. The gray triangled (white squared) points represent the calculated X-ray strain for the fiber textured (isotropic) case. The *experimental* determined stress value of -1415 MPa was used for the calculation. The equibiaxial stress of the CrN sample was determined using X-ray curvature method described in Cha. 3.3. A fiber textured (isotropic) ODF with an angular resolution of 5° was used.

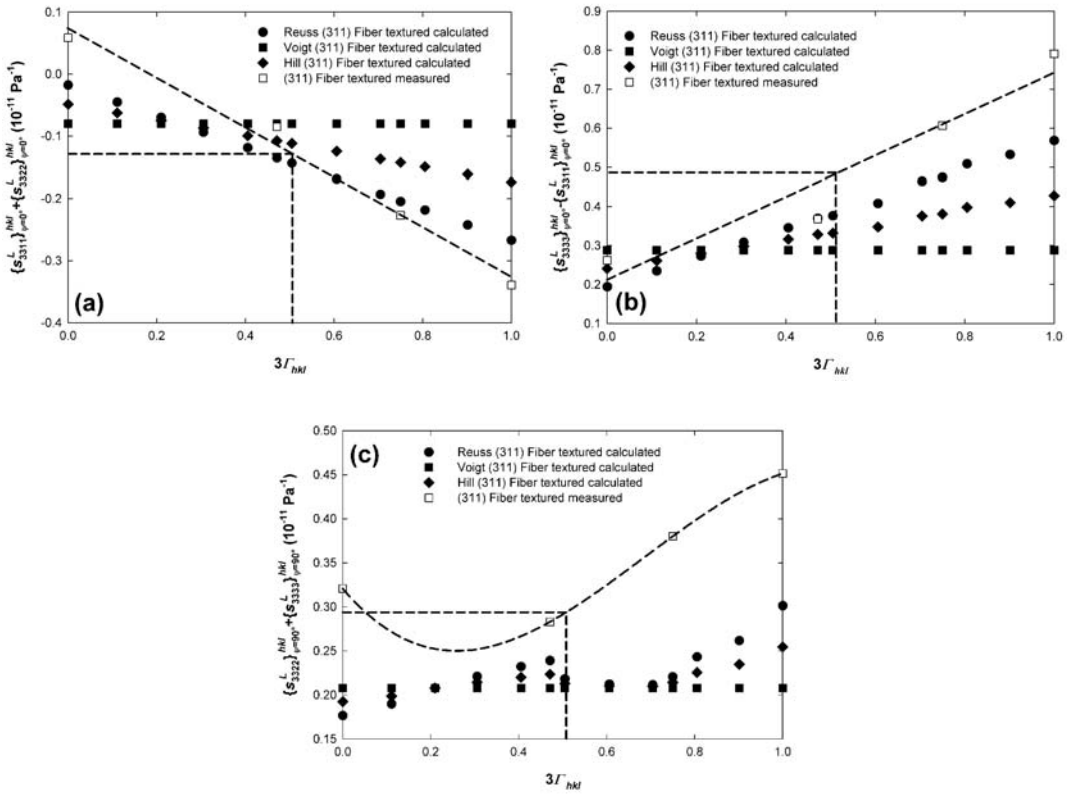

Figure 4.8: The figures (a)-(c) show calculated and measured *compliance terms* as a function of $3\Gamma_{hkl}$. The *compliance terms* for Reuss, Voigt and Hill were calculated for a (311) fiber textured CrN sample with ISO and ψ_{FWHM} of 13% and 12°, respectively. The resolution of the ODF was 5°. The white squared data points were calculated from the slopes and intersections of the $\left\{\epsilon_{33}^{L}\right\}_{\psi}^{hkl} - \sin^2\psi$ plots in Fig. 4.7a-d. At $\psi = 0°$, the X-ray elastic constant $2\{s_1\}_{\psi=0°}^{hkl}$ (Eq. 2.40) is equal to $\left\{S_{3311}^{L}\right\}_{\psi=0°}^{hkl} + \left\{S_{3322}^{L}\right\}_{\psi=0°}^{hkl}$ (a). For textured materials this relation only holds at $\psi = 0°$. $2\{s_1\}_{\psi=0°}^{hkl}$ can be calculated from the intersection of the corresponding $\left\{\epsilon_{33}^{L}\right\}_{\psi}^{hkl} - \sin^2\psi$ plot at $\psi = 0°$. The *compliance term* $\left\{S_{3333}^{L}\right\}_{\psi=0°}^{hkl} - \left\{S_{3311}^{L}\right\}_{\psi=0°}^{hkl}$ can be determined from the slope of the corresponding $\left\{\epsilon_{33}^{L}\right\}_{\psi}^{hkl} - \sin^2\psi$ plot. Due to the fact that the averaged slope of $\left\{\epsilon_{33}^{L}\right\}_{\psi}^{hkl} - \sin^2\psi$ plot is considered, this equation holds for the whole $\sin^2\psi$-range. At $\psi = 90°$, the *compliance term* $\left\{S_{3322}^{L}\right\}_{\psi=90°}^{hkl} + \left\{S_{3333}^{L}\right\}_{\psi=90°}^{hkl}$ correlates to the intersection of the corresponding $\left\{\epsilon_{33}^{L}\right\}_{\psi}^{hkl} - \sin^2\psi$ plot at $\psi = 90°$. The data shows that there is a difference between the measured and calculated *compliance terms*. It is assumed that this difference is the result of inaccurate SECs and/or stress gradients in the CrN film. The *mechanical out-of-plane* Young's modulus $\left\{E_{3333}^{S}\right\}^{\mathrm{M}}$, the Poisson's ratio $\left\{\nu_{3311}^{S}\right\}^{\mathrm{M}}$ and the *mechanical in-plane* biaxial modulus $\left\{M^{S}\right\}^{\mathrm{M}}$ are 240.79 GPa, 0.16 and 344.8 GPa, respectively. *Calculated* and *experimental* data are listed in Tab. 4.2.

4.3 TiN sample

The third sample is a 0.53 μm thick TiN thin film deposited onto a 315 μm thick Si(100) substrate. The curvature was -4.796 m, the corresponding stress value was about -1178 MPa. A dominant (200) fiber texture was found (Fig. 4.10). The ISO and ψ_{FWHM} were 15% and 13°, respectively. Moreover, the X-ray strains $\left\{\epsilon_{33}^{L}\right\}_{\psi}^{hkl}$ as a function of $\sin^2\psi$ for multiple reflexes were measured. Altogether four crystallographic reflexes could be found in the 2θ range of the TiN sample. The X-ray strains of four representative crystallographic refelexes are plotted in Fig. 4.11a-d. The $\left\{\epsilon_{33}^{L}\right\}_{\psi}^{hkl} - \sin^2\psi$ relation is extremly non-linear for all reflexes *hkl*. This can be a result of stress gradients [12], complex stress states [26] or macroscopic elastic anisotropy (texture). The TiN sample possesses a (200) fiber texture, *i.e.* $3\Gamma_{uvw} = 0$. The corresponding $3\Gamma_{hkl}^{*}$ value is therefore 0.18 (Eq. 2.61). The $3\Gamma_{hkl}^{*}$ value is used to determine the *mechanical compliances* from Figs. 4.12a-c. The *mechanical out-of-plane* Young's modulus $\left\{E_{3333}^{S}\right\}^{\mathrm{M}}$, the Poisson's ratio $\left\{\nu_{3311}^{S}\right\}^{\mathrm{M}}$ and the *mechanical in-plane* biaxial modulus $\left\{M^{S}\right\}^{\mathrm{M}}$ are 412.5 GPa, 0.21 and 561.8 GPa, respectively. *Calculated* and *experimental* data are listed in Tab. 4.3.

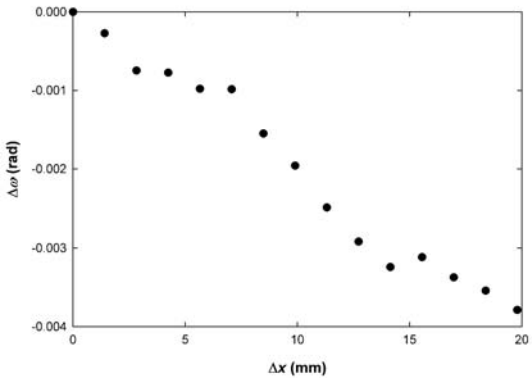

Figure 4.9: The plot of $\Delta\omega$ vs. Δx (Sec. 3.3). The curvature is -4.796 m. The TiN thickness and the Si(100) substrate thickness were 0.53 μm and 315 μm, respectively. The equibiaxial stress is -1178 MPa and was calculated according to Eq. 3.4.

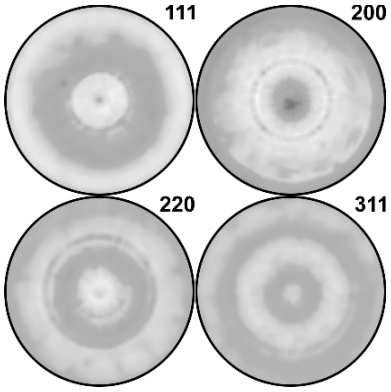

Figure 4.10: This figure shows the pole figures of the TiN sample. The detector of the diffractometer was fixed at the 2θ positions of the corresponding crystallographic reflexes listed in Tab. 3.2. The angular resolution in α and β space was 5°. The pole figures were measured in equal area mode with a counting time of 2 s. The background was automatically subtracted by the measurement software. The pole figures were measured with a Seifert PTS 3000. A (200) fiber was found and used for the calculation.

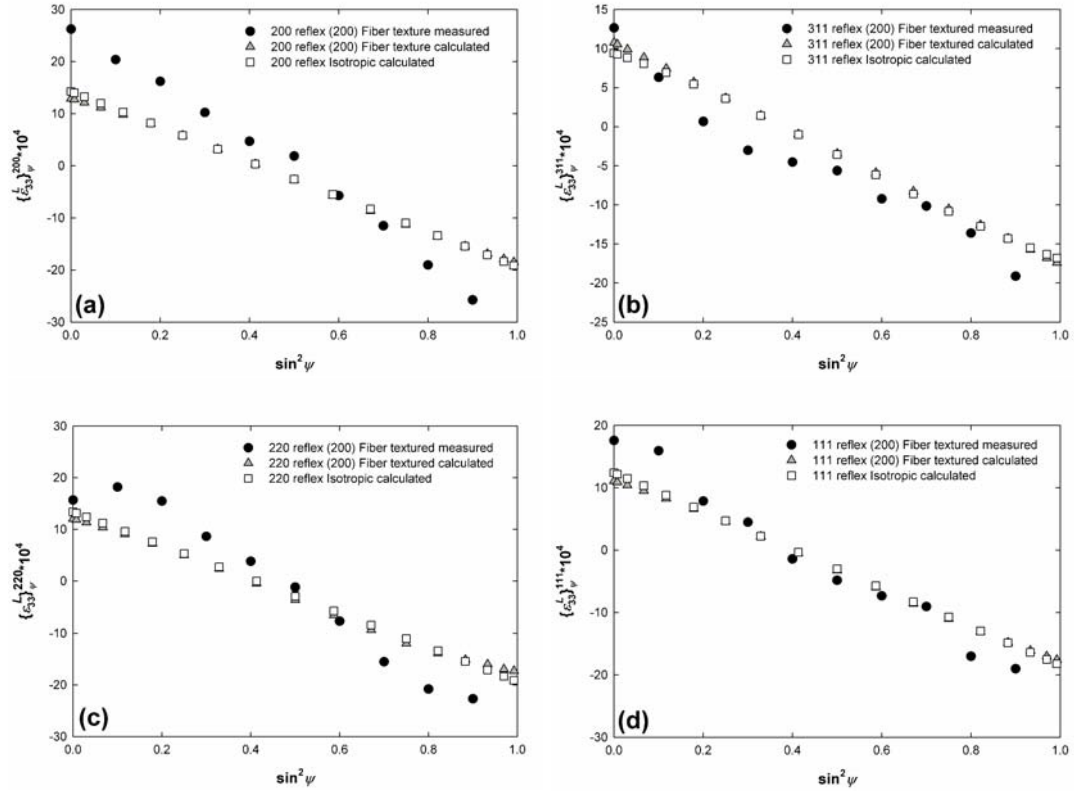

Figure 4.11: The figures (a)-(d) show the X-ray strain of four crystallographic reflexes of a (200) fiber textured TiN sample as a function of $\sin^2\psi$. The black circled data points represent the *experimental* data. The X-ray strain was determined from the $\{d\}_{\psi}^{hkl}$ values according to Eq. 3.1 using a lattice free parameter $a_0 = 4.248$ [81, 82]. The gray triangled (white squared) points represent the calculated X-ray strain for the fiber textured (isotropic) case. The *experimental* determined stress value of -1178 MPa was used for the calculation. The equibiaxial stress of the TiN sample was determined using X-ray curvature method described in Cha. 3.3. A fiber textured (isotropic) ODF with an angular resolution of 5° was used.

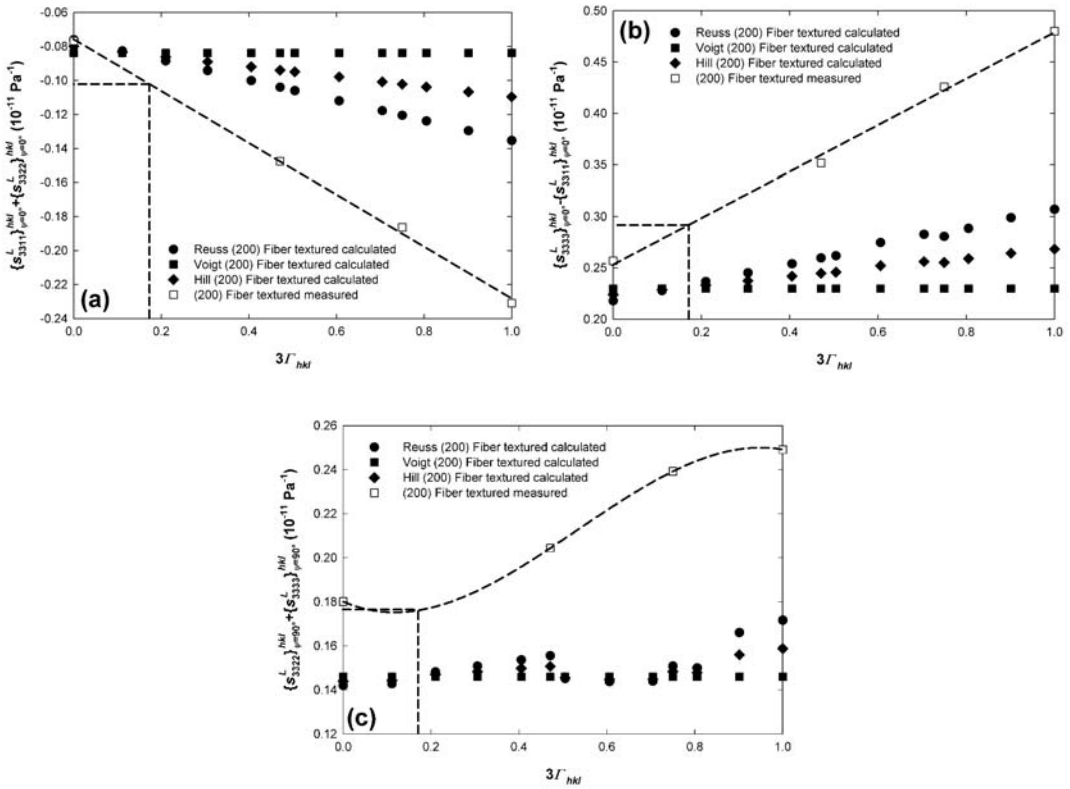

Figure 4.12: The figures (a)-(c) show calculated and measured *compliance terms* as a function of $3\Gamma_{hkl}$. The *compliance terms* for Reuss, Voigt and Hill were calculated for a (200) fiber textured TiN sample with $\psi_{\mathrm{FWHM}} = 13°$ and ISO=15°. The resolution of the ODF was 5°. The white squared data points were calculated from the slopes and intersections of the $\left\{\epsilon_{33}^{L}\right\}_{\psi}^{hkl} - \sin^2\psi$-plots in Fig. 4.11a-d. At $\psi = 0°$, the X-ray elastic constant $2\{s_1\}_{\psi=0°}^{hkl}$ (Eq. 2.40) is equal to $\{S_{3311}\}_{\psi=0°}^{hkl} + \{S_{3322}\}_{\psi=0°}^{hkl}$ (a). For textured materials this relation only holds at $\psi = 0°$. $2\{s_1\}_{\psi=0°}^{hkl}$ can be calculated from the intersection of the corresponding $\left\{\epsilon_{33}^{L}\right\}_{\psi}^{hkl} - \sin^2\psi$-plot at $\psi = 0°$. The *compliance term* $\{S_{3333}\}_{\psi=0°}^{hkl} - \{S_{3311}\}_{\psi=0°}^{hkl}$ can be determined from the slope of the corresponding $\left\{\epsilon_{33}^{L}\right\}_{\psi}^{hkl} - \sin^2\psi$-plot. Due to the fact that the averaged slope of $\left\{\epsilon_{33}^{L}\right\}_{\psi}^{hkl} - \sin^2\psi$-plot is considered, this equation holds for the whole $\sin^2\psi$-range. At $\psi = 90°$, the *compliance term* $\{S_{3322}\}_{\psi=90°}^{hkl} + \{S_{3333}\}_{\psi=90°}^{hkl}$ correlates to the intersection of the corresponding $\left\{\epsilon_{33}^{L}\right\}_{\psi}^{hkl} - \sin^2\psi$-plot at $\psi = 90°$. The figures clearly show that the measured data points are not in good agreement with the calculated Hill data. A possible reason could be that the SECs of TiN and/or the lattice parameter a_0 are not correct. The *mechanical out-of-plane* Young's modulus $\left\{E_{3333}^{S}\right\}^{\mathrm{M}}$, the Poisson's ratio $\left\{\nu_{3311}^{S}\right\}^{\mathrm{M}}$ and the *mechanical in-plane* biaxial modulus $\left\{M^{S}\right\}^{\mathrm{M}}$ are 412.5 GPa, 0.21 and 561.8 GPa, respectively. *Calculated* and *experimental* data are listed in Tab. 4.3.

4.4 Experimental and simulated data

Tabs. 4.1-4.3 summarize the *experimental* and *calculated* data from Cha. 4. The Cu data show similar results for the *experimental* and *calculated mechanical out-of-plane* Young's Modulus $\left\{E^S_{3333}\right\}^{\mathrm{M}}$, Poisson's ratio $\left\{\nu^S_{3311}\right\}^{\mathrm{M}}$ and *mechanical in-plane* biaxial modulus $\left\{M^S\right\}^{\mathrm{M}}$ (Tab. 4.1). Fig. 4.4 shows that the *calculated* data of the $3\Gamma_{hkl}$ plots is comparable with the *experimental* data. However, the *experimental* data for CrN (Fig. 4.8) and TiN (Fig. 4.12) significantly differ from the *calculated* data (Tabs. 4.2 and 4.3). The *experimental* data of the $3\Gamma_{hkl}$ plots (Figs. 4.8 and 4.12) is not comparable in magnitude but in its $3\Gamma_{hkl}$ dependence with the *experimental* data. Possible reasons for the difference in the *experimental* and *calculated* data are stress gradients [12], change in chemical composition [83], change in morphology [84],texture gradients [85], incorrect unstressed lattice parameter or incorrect SECs.

Table 4.1: *Mechanical out-of-plane* Young's Modulus $\left\{E^S_{3333}\right\}^{\mathrm{M}}$, Poisson's ratio $\left\{\nu^S_{3311}\right\}^{\mathrm{M}}$ and *mechanical in-plane* biaxial modulus $\left\{M^S\right\}^{\mathrm{M}}$ of Cu.

	$3\Gamma_{uvw}$	ψ_{FWHM}	ISO	$3\Gamma^*_{hkl}$	$\left\{E^S_{3333}\right\}^{\mathrm{M}}$	$\left\{\nu^S_{3311}\right\}^{\mathrm{M}}$	$\left\{M^S\right\}^{\mathrm{M}}$
		(°)	(%)		(GPa)		(GPa)
Calculation	1.0	14	10	0.89	174.1	0.29	245.5
Experiment	1.0	14	10	0.89	169.4	0.23	223.3

Table 4.2: *Mechanical out-of-plane* Young's Modulus $\left\{E^S_{3333}\right\}^{\mathrm{M}}$, Poisson's ratio $\left\{\nu^S_{3311}\right\}^{\mathrm{M}}$ and *mechanical in-plane* biaxial modulus $\left\{M^S\right\}^{\mathrm{M}}$ of CrN.

	$3\Gamma_{uvw}$	ψ_{FWHM}	ISO	$3\Gamma^*_{hkl}$	$\left\{E^S_{3333}\right\}^{\mathrm{M}}$	$\left\{\nu^S_{3311}\right\}^{\mathrm{M}}$	$\left\{M^S\right\}^{\mathrm{M}}$
		(°)	(%)		(GPa)		(GPa)
Calculation	0.47	12	13	0.51	357.7	0.20	447.0
Experiment	0.47	12	13	0.51	240.8	0.16	344.8

Table 4.3: *Mechanical out-of-plane* Young's Modulus $\left\{E^S_{3333}\right\}^{\mathrm{M}}$, Poisson's ratio $\left\{\nu^S_{3311}\right\}^{\mathrm{M}}$ and *mechanical in-plane* biaxial modulus $\left\{M^S\right\}^{\mathrm{M}}$ of TiN.

	$3\Gamma_{uvw}$	ψ_{FWHM}	ISO	$3\Gamma^*_{hkl}$	$\left\{E^S_{3333}\right\}^{\mathrm{M}}$	$\left\{\nu^S_{3311}\right\}^{\mathrm{M}}$	$\left\{M^S\right\}^{\mathrm{M}}$
		(°)	(%)		(GPa)		(GPa)
Calculation	0.0	13	15	0.18	533.0	0.22	685.9
Experiment	0.0	13	15	0.18	412.5	0.21	561.8

5 Summary

Within this thesis a new method was introduced to determine *mechanical out-of-plane* Young's modulus, a Poisson's ratio and *mechanical in-plane* biaxial modulus of thin films deposited on single crystal substrates using static diffraction techniques. The procedure consists of two static diffraction measurements, *i.e.* the curvature determination of the thin film - substrate composite and the X-ray strain measurement of multiple crystallographic reflections. It was shown that the determination of the X-ray curvature is a fast and simple method to obtain the homogeneous equibiaxial macroscopic stress within the thin film [54]. The anisotropy of X-ray strain was simulated within Cha. 2. It was shown that X-ray strain anisotropies, due to texture, influence the X-ray elastic stiffness of a thin film. The grain interaction models were briefly described and used to calculate mechanical and X-ray compliance tensors for different materials. It was shown how to calculate mechanical elastic constants for arbitrary fiber textured materials with different ψ_{FWHM} and ISO. The formalism to extract relevant data from the *experimental* $\left\{\epsilon_{33}^{L}\right\}_{\psi}^{hkl} - \sin^2\psi$ graphs was discussed. The accessible data obtained from X-ray strain measurements are the intersections of strain at $\psi = 0°$ and $\psi = 90°$ as well as the averaged slopes. The slopes can be averaged, if and only if, the standard deviation of the slope is small enough. If the $\sin^2\psi$ plots are extremely nonlinear only because of anisotropy, the slopes can be evaluated at the angles $\psi = 0°$ and $\psi = 90°$. If not, the averaged slope can be used instead of explicitly calculating the slopes at $\psi = 0°$ and $\psi = 90°$. This procedure allows the determination of the values $\left\{S_{3311}^{L}\right\}_{\psi=0°}^{\mathrm{H},hkl}$, $\left\{S_{3333}^{L}\right\}_{\psi=0°}^{\mathrm{H},hkl}$ and $\left\{S_{3333}^{L}\right\}_{\psi=90°}^{\mathrm{H},hkl} + \left\{S_{3322}^{L}\right\}_{\psi=90°}^{\mathrm{H},hkl}$. At different polar angles ψ it is possible to determine X-ray compliance tensor components for various hkl reflexes which can be plotted as a function of $3\Gamma_{hkl}$. The corresponding $3\Gamma_{hkl}^{*}$ value for a specific fiber textured material with $3\Gamma_{uvw}$, ψ_{FWHM} and ISO is correlated with a crystallographic reflex. Although this crystallographic reflex is commonly not accessible, the corresponding X-ray compliance component can be found in the $3\Gamma_{hkl}$ plot along

the regression line of all measured X-ray compliance components. This specific X-ray compliance component must be equal to the mechanical compliance component and thus reveals the correct value for $3\Gamma^*_{hkl}$. The $3\Gamma^*_{hkl}$ values can be *calculated* for any fiber texture material identified through $3\Gamma_{uvw}$, ψ_{FWHM} and ISO. Consecutively this leads to the connection between X-ray elastic and mechanical stiffness in the $3\Gamma^*_{hkl} - 3\Gamma_{uvw}$ plots. It was demonstrated that this correlation is independent of the materials, *i.e.* of the mechanical crystal anisotropy and that it is possible to extract a "user-friendly" function which can be used to directly calculate the correct $3\Gamma^*_{hkl}$ value.

In Cha. 4 the *experimental* data for three materials were used to determine the mechanical elastic constants. The *experimental* data of Cu are in good agreement with *calculated* data. The *mechanical out-of-plane* Young's modulus $\left\{E^S_{3333}\right\}^{\mathrm{M}}$, Poisson's ratio $\left\{\nu^S_{3311}\right\}^{\mathrm{M}}$ and *mechanical in-plane* biaxial modulus $\left\{M^S\right\}^{\mathrm{M}}$ of Cu are 169.40 GPa, 0.23 and 223.3 GPa, respectively. The *experimental* data for CrN and TiN differ from the *calculated* values significantly. Possible reasons are the existence of stress gradients, inaccurate unstressed lattice parameters and SECs and/or elastic anisotropy. The *mechanical out-of-plane* Young's modulus $\left\{E^S_{3333}\right\}^{\mathrm{M}}$, Poisson's ratio $\left\{\nu^S_{3311}\right\}^{\mathrm{M}}$ and *mechanical in-plane* biaxial modulus $\left\{M^S\right\}^{\mathrm{M}}$ of CrN are 240.79 GPa, 0.16 and 344.8 GPa, respectively. For TiN they are 412.5 GPa, 0.21 and 561.8 GPa.

In the future it will be an important task to improve this method for high temperature measurements. The lattice parameter a_0 is the most critical parameter in all calculations presented within this thesis. Due to the fact that a_0 is temperature dependent it will be a necessity to know the exact temperature behaviour of this parameter. If so, it should be possible to determine *mechanical out-of-plane* Young's modulus, Poisson's ratio and *mechanical in-plane* biaxial modulus at elevated temperatures which is extremely important for thin film design. Due to the fact that nearly all tools coated with nitrides exhibit high temperatures when used the described method can be a useful technique to determine the temperature dependent mechanical elastic constants. In comparison to other techniques used to determine the mechanical elastic constants [43, 44, 47, 50], the X-ray beams can be used as a probe which is not influenced by high temperatures. The development of X-ray tools proceeds and will deliver new, faster and more accurate possibilities to characterize X-ray strains in special and information provided by X-rays in common.

As part of the PhD-thesis, three main author peer reviewed papers were published in international scientific journals and two main author papers were submitted. The papers summarize the evolution of the work described in this thesis. Scientific research has also been done in the field of high-temperature residual stress analysis of thin films and in the field of high-temperature residual stress gradient analysis.

6 Bibliography

[1] Martinez, E., Romero, J., Lousa, A., and Esteve, J. *Surf. Coat. Technol.* **163**, 571–577 (2003).

[2] Mendibide, C., Steyer, P., Fontaine, J., and Goudeau, P. *Surf. Coat. Technol.* **201**(7), 4119–4124 (2006).

[3] Bajt, S., Edwards, N. V., and Madey, T. E. *Surf. Sci. Rep.* **63**(2), 73–99 (2008).

[4] Miyoshi, K., Pouch, J. J., Alterovitz, S. A., Pantic, D. M., and Johnson, G. A. *Wear* **133**(1), 107–123 (1989).

[5] Ohnuma, H., Nihira, N., Mitsuo, A., Toyoda, K., Kubota, K., and Aizawa, T. *Surf. Coat. Technol.* **177**, 623–626 (2004).

[6] Hultman, L. *Vacuum* **57**(1), 1–30 (2000).

[7] Hellgren, N., Lin, N., Broitman, E., Serin, V., Grillo, S. E., Twesten, R., Petrov, I., Colliex, C., Hultman, L., and Sundgren, J. E. *Int. J. Mater. Res.* **16**(11), 3188–3201 (2001).

[8] Carvalho, N. J. M., Zoestbergen, E., Kooi, B. J., and De Hosson, J. T. M. *Thin Solid Films* **429**(1-2), 179–189 (2003).

[9] Peng, R. L., Wang, Y. D., Oden, M., and Almer, J. *Residual Stresses Vii, Proceedings* **490-491**, 643–648 (2005).

[10] Cunha, L. and Andritschky, M. *Surf. Coat. Technol.* **111**(2-3), 158–162 (1999).

[11] Genzel, C. and Reimers, W. *Surf. Coat. Technol.* **119**, 404–409 (1999).

[12] Genzel, C. and Reimers, W. *Zeitschrift Fur Metallkunde* **94**(6), 655–661 (2003).

[13] Genzel, C., Stock, C., and Reimers, W. *Mater. Sci. Eng. A* **372**(1-2), 28–43 (2004).

[14] Genzel, C., Klaus, A., Denks, I., and Wulz, H. G. *Mater. Sci. Eng. A* **390**(1-2), 376–384 (2005).

[15] Welzel, U. and Mittemeijer, E. J. *Z. Kristallogr.* **222**(3-4), 160–173 (2007).

[16] Welzel, U., Leoni, M., Lamparter, P., and Mittemeijer, E. J. *J. Mater. Sci. Technol.* **18**(2), 121–124 (2002).

[17] Guisbiers, G., Van Overschelde, O., and Wautelet, M. *Acta Mater.* **55**(10), 3541–3546 (2007).

[18] Panicaud, B., Grosseau-Poussard, J. L., and Dinhut, J. F. *Appl. Surf. Sci* **252**(16), 5700–5713 (2006).

[19] Pauleau, Y. *Vacuum* **61**(2-4), 175–181 (2001).

[20] Martinschitz, K. J., Daniel, R., Mitterer, C., and Keckes, J. *Thin Solid Films* **516**(8), 1972–1976 (2008).

[21] Ahlgren, M. and Blomqvist, H. *Surf. Coat. Technol.* **200**(1-4), 157–160 (2005).

[22] Davis, R. F., Einfeldt, S., Preble, E. A., Roskowski, A. M., Reitmeier, Z. J., and Miraglia, P. Q. *Acta Mater.* **51**(19), 5961–5979 (2003).

[23] Pao, C. W. and Srolovitz, D. J. *J. Mech. Phys. Solids* **54**(12), 2527–2543 (2006).

[24] Suresh, S. and Freund, L. B. *Thin Film Materials Stress, Defect Formation and Surface Evolution.* Cambridge University Press, Cambridge, (2003).

[25] Newnham, R. E. *Properties of materials Anisotropy Symmetry Structure.* Oxford University Press, New York, (2005).

[26] Noyan, I. C. and Cohen, J. B. *Residual Stress Measurement by Diffraction and Interpretation.* Springer, (1987).

[27] Nye, J. F. *Physical Properties of Crystals.* Oxford Univ. Press, (1976).

[28] Liu, B., Wang, J. Y., Zhou, Y. C., Liao, T., and Li, F. Z. *Acta Mater.* **55**(9), 2949–2957 (2007).

[29] Le Page, Y., Saxe, P., and Rodgers, J. R. *Phys. Status Solidi B* **229**(3), 1155–1161 (2002).

[30] Isono, Y., Kishimoto, H., and Tanaka, T. *Mater. Sci. Res. Int.* **4**(1), 39–44 (1998).

[31] Voigt, W. *Lehrbuch der Kristallphysik.* Teubner, Leipzig, (1910).

[32] Reuss, A. *Z. Angew. Math. Mech.* **9**(1), 49–58 (1929).

[33] Hill, R. *Proc. R. Soc. London, Ser. A* **65**(389), 349–355 (1952).

[34] Eshelby, J. D. *Proc. R. Soc. London, Ser. A* **241**(1226), 376–396 (1957).

[35] Vook, R. W. and Witt, F. *J. Appl. Phys.* **36**(7), 2169 (1965).

[36] Welzel, U., Freour, S., and Mittemeijer, E. J. *Philos. Mag.* **85**(21), 2391–2414 (2005).

[37] Van Houtte, P., Delannay, L., and Kalidindi, S. R. *Int. J. Plast.* **18**(3), 359–377 (2002).

[38] Welzel, U. and Freour, S. *Philos. Mag.* **87**(26), 3921–3943 (2007).

[39] Genzel, C., Reimers, W., Malek, R., and Pohlandt, K. *Mater. Sci. Eng. A* **205**(1-2), 79–90 (1996).

[40] Steuwer, A., Santisteban, J. R., Withers, P. J., Edwards, L., and Fitzpatrick, M. E. *J. Appl. Cryst.* **36**, 1159–1168 (2003).

[41] Ma, C. H., Huang, J. H., and Chen, H. *Thin Solid Films* **418**(2), 73–78 (2002).

[42] Möller, H. and Martin, G. *K.W.I. Eisenforschung* **21**, 261–269 (1939).

[43] Fischer-Cripps, A. C. *Nanoindentation*. Springer, New York, (2004).

[44] Hurley, D. C., Tewary, V. K., and Richards, A. J. *Meas. Sci. Technol.* **12**(9), 1486–1494 (2001).

[45] Read, D. T., Cheng, Y. W., Keller, R. R., and McColskey, J. D. *Scr. Mater.* **45**(5), 583–589 (2001).

[46] Leisure, R. and Willis, F. *J. Phys.: Condens. Matter* **9**, 6001–6029 (1997).

[47] Cheng, Y. W., Read, D. T., McColskey, J. D., and Wright, J. E. *Thin Solid Films* **484**(1-2), 426–432 (2005).

[48] Wei, X., Lee, D., Shim, S., Chen, X., and Kysar, J. W. *Scr. Mater.* **57**(6), 541–544 (2007).

[49] Keller, R. R., Phelps, J. M., and Read, D. T. *Mater. Sci. Eng. A* **214**(1-2), 42–52 (1996).

[50] Huang, H. B. and Spaepen, F. *Acta Mater.* **48**(12), 3261–3269 (2000).

[51] Hayakawa, M., Imai, S., and Oka, M. *J. Appl. Cryst.* **18**(Dec), 513–518 (1985).

[52] Gnaupel-Herold, T., Brand, P. C., and Prask, H. J. *J. Appl. Cryst.* **31**, 929–935 (1998).

[53] Stoney, G. G. *Proc. Phys. Soc. London, Sect. A* **82**, 172 (1909).

[54] Segmüller, A., Noyan, I. C., and Speriosu, V. S. *Prog. Cryst. Growth Charact. Mater.* **18**, 21–66 (1989).

[55] Wolfram Research, Inc. *Mathematica, Version 5.0, Champaign, IL* (2003).

[56] Leoni, M., Welzel, U., Lamparter, P., Mittemeijer, E. J., and Kamminga, J. D. *Philos. Mag. A* **81**(3), 597–623 (2001).

[57] Welzel, U. *Diffraction Analysis of Residual Stress; Modelling Elastic Grain Interaction.* PhD thesis, Universitt Stuttgart, (2002).

[58] Sands, D. E. *Vectors and tensors in crystallography.* Constable and Company, Ltd., London, (1982).

[59] Landau, L. and Lifshitz, E. *Lehrbuch der theoretischen Physik.* Elastizitttstheorie. Akadmie Verlag, Berlin, (1991).

[60] Landau, L. and Lifshitz, E. *Lehrbuch der theoretischen Physik.* Klassische Feldtheorie. Akadmie Verlag, Berlin, (1997).

[61] van Houtte, P. and De Buyser, L. *Acta metall. mater.* **41**(2), 323–336 (1993).

[62] Barral, M., Lebrun, J., Sprauel, J., and Maeder, G. *Metall. Mater. Trans. A* **18**(7), 1229–1238 (1987).

[63] Dölle, H. and Hauk, V. *Z. Metallkd.* **68**(11), 725–728 (1977).

[64] Bunge, H. J. *Texture Analysis in Materials Science.* Butterworths, London, (1982).

[65] LaboSoft, s.c. *LaboTex - The Texture Analysis Software, Version 3.0.17A, Cracow,* (1997-2008).

[66] Swanson and Tatge. *Natl. Bur. Stand. (U.S.), Circ. 539* **0**, 15 (1953).

[67] Gall, D., Shin, C. S., Spila, T., Oden, M., Senna, M. J. H., Greene, J. E., and Petrov, I. *J. Appl. Phys.* **91**(6), 3589–3597 (2002).

[68] Almer, J., Lienert, U., Peng, R. L., Schlauer, C., and Oden, M. *J. Appl. Phys.* **94**(1), 697–702 (2003).

[69] Kim, J. O., Achenbach, J. D., Mirkarimi, P. B., Shinn, M., and Barnett, S. A. *J. Appl. Phys.* **72**(5), 1805–1811 (1992).

[70] Stickforth, J. *Tech. Mitt. Krupp - Forsch.-Ber.* **24**(3), 89–102 (1966).

[71] Bartsch, H. J. *Taschenbuch mathematischer Formeln.* Fachbuchverlag Leipzig-Köln, Leipzig, (1994).

[72] Bunge, H. J., Kiewel, R., Reinert, T., and Fritsche, L. *J. Mech. Phys. Solids* **48**(1), 29–66 (2000).

[73] Wenk, H. R., Matthies, S., Donovan, J., and Chateigner, D. *J. Appl. Cryst.* **31**, 262–269 (1998).

[74] Huang, F. and Weaver, M. L. *J. Appl. Phys.* **98**(7) (2005).

[75] Bollenrath, F., Hauk, V., and Müller, E. H. *Z. Metallkd.* **58**, 76–82 (1967).

[76] Zener, C. *Elasticity and Anelasticity of Metals.* University of Chicago Press, Chicago, (1948).

[77] Martinschitz, K. J. and Keckes, J. *J. Appl. Cryst.* , First paper in series (2008).

[78] Eiper, E., Martinschitz, K. J., and Keckes, J. *Powder Diffr.* **21**(1), 25–29 (2006).

[79] Zhao, Z. B., Hershberger, J., Yalisove, S. M., and Bilello, J. C. *Thin Solid Films* **415**(1-2), 21–31 (2002).

[80] Koch, R. *Intrinsic stress of epitaxial thin films and surface layers.* Growth and Properties of Ultrathin Epitaxial Layers. Elsevier, Amsterdam, (1997).

[81] Dopita, M. and Rafaja, D. *Z. Kristallogr* , 67–72 (2006).

[82] Benegra, M., Lamas, D. G., de Rapp, M. E. F., Mingolo, N., Kunrath, A. O., and Souza, R. M. *Thin Solid Films* **494**(1-2), 146–150 (2006).

[83] Hones, P., Consiglio, R., Randall, N., and Levy, F. *Surf. Coat. Technol.* **125**(1-3), 179–184 (2000).

[84] Hohl, F., Stock, H. R., and Mayr, P. *Surf. Coat. Technol.* **54**(1-3), 160–166 (1992).

[85] Rauschenbach, B. and Gerlach, J. W. *Cryst. Res. Technol.* **35**(6-7), 675–688 (2000).

7 Conference contributions

7.1 Talks

- Meca Sens IV, Vienna, Austria, 24 - 26 September 2007
- CRG Evaluation of the HMI Beamlines at the 7T-MPW, Berlin, Germany, 20 February 2008 (invited)
- Denver X-Ray Conference, Denver, USA, 4 - 8 August 2008

7.2 Poster sessions

- Denver X-Ray Conference, Denver, USA, 7 - 11 August 2006
- Gordon Research Conference, Waterville, USA, 30 Juli - 4 August 2006
- ECRS 7, Berlin, Germany, 13 - 15 September 2006
- Meca Sens IV, Vienna, Austria, 24 - 26 September 2007
- RSD Symposium, Leoben, Austria, 6 - 7 December 2007
- ICMCTF, San Diego, USA, 28 April - 2 May 2008
- Denver X-Ray Conference, Denver, USA, 4 - 8 August 2008

8 List of Papers

8.1 Main author papers

Paper A
Martinschitz K.J., Eiper E., Massl S., et al.
Rapid determination of stress factors and absolute residual stresses in thin films
Journal of Applied Crystallography **39** (6): 777-783 (2006)

Paper B
Martinschitz K.J., Eiper E., Keckes J.
Stress factors and absolute residual stresses in thin films determined by the combination of curvature and $sin^2\psi$ methods
Materials Science Forum **524-525** : 711-715 (2006)

Paper C
Martinschitz K.J., Daniel R., Mitterer C. and Keckes J.
Stress evolution in CrN/Cr coating systems during thermal straining
Thin Solid Films **516** (8): 1972-1976 (2008)

Paper D
Martinschitz K.J. and Keckes J.
Elastic constants of fibre-textured thin films determined by diffraction under static conditions: I. Theoretical concept
Journal of Applied Crystallography submitted

Paper E
Martinschitz K.J. and Keckes J.
Elastic constants of fibre-textured thin films determined by diffraction under static conditions: II. Empirical data
Journal of Applied Crystallography submitted

8.2 Co author papers

Paper F
Eiper E., Keckes J., Martinschitz K.J., et al.
Size-independent stresses in Al thin films thermally strained down to-100 degrees C
Acta Materialia **55** (6): 1941-1946 (2007)

Paper G
Keckes J., Eiper E., Martinschitz K.J., et al.
High-temperature residual stresses in thin films characterized by x-ray diffraction substrate curvature method
Review of Scientific Instruments **78** (3): (2007)

Paper H
Keckes J., Eiper E., Martinschitz K.J., et al.
In-situ x-ray diffraction as a tool to probe mechanical phenomena down to the nanoscale
Advanced Engineering Materials **8** (11): 1084-1088 (2006)

Paper I
Eiper E., Martinschitz K.J., Keckes J.
Combined elastic strain and macroscopic stress characterization in polycrystalline Cu thin films
Powder Diffraction **21** (1): 25-29 (2006)

Paper J
Eiper E., Martinschitz K.J., Gerlach J.W., et al.
X-ray elastic constants determined by the combination of $sin^2\psi$ and substrate-curvature methods
Zeitschrift für Metallkunde **96** (9): 1069-1073 (2005)

A

Rapid determination of stress factors and absolute residual stresses in thin films

K.J. Martinschitz[a], E. Eiper[a], S. Massl[a], H. Köstenbauer[b], R. Daniel[c], G. Fontalvo[b], C. Mitterer[b,c] and J. Keckes[a]

[a]Erich Schmid Institute of Materials Science, Austrian Academy of Sciences, A–8700 Leoben, Austria
[b]Department of Physical Metallurgy and Materials Testing, Universiy of Leoben, Leoben, Austria
[c]Christian-Doppler Laboratory for Advanced Coatings, University of Leoben, Leoben, Austria

Abstract A methodology is presented that allows the determination of experimental stress factors in thin films on the basis of static diffraction measurements. The approach relies on the characterization of thin films deposited on a monocrystalline substrate serving as a mechanical sensor. Rocking-curve measurements of the symmetrical reflections of the substrate are used to determine the substrate curvature and subsequently the macroscopic stress imposed on the film. The elastic strain in the film is determined by lattice-spacing measurement at different sample tilt angles. The calculated experimental stress factors are applied to thin films deposited on other types of substrates and are used to determine the absolute magnitude of the residual stress. The approach is applied to nanocrystalline TiN and CrN thin films deposited on Si(100) and steel substrates, characterized using a laboratory-type θ/θ goniometer.

A.1 Introduction

The determination of residual stresses in anisotropic polycrystalline thin films by diffraction methods is a challenging task [1]. Such films often exhibit strong textures that limit the possibilities to determine the lattice spacing of the film at specific sample tilt angles. Moreover, the presence of texture requires the use of dedicated stress factors F_{ij} in order to calculate residual stresses from the measured elastic strain [2]. Stress factors of textured thin films can be determined experimentally or by modelling. The experimental determination of stress factors usually requires the use of techniques that enable the controlled loading of the film in the diffraction system to determine the corresponding elastic response of the crystal lattice [3–5]. The mechanical loading is usually carried out by four-point bending or by tensile straining. The main problem with such techniques is the precise determination of macroscopic strain and stability over the period when the elastic strain is determined. Alternatively, stress factors of thin films can be calculated on the basis of single-crystal elastic constants, the orientation distribution function and the assumed elastic interaction between the grains [1, 6–9]. Significant effort has been devoted to formulate and apply various elastic interaction models in order to evaluate, in particular, oscillatory $\sin^2\psi$ dependences. The calculation of theoretical stress factors is usually a laborious task since the orientation distribution function of the crystallites must be determined experimentally and the application of the specific elastic interaction model is not trivial. Another problem lies in the fact that the theoretical stress factors are calculated on the basis of bulk elastic constants of known materials. For new or non-stoichiometric materials with unknown compliances, the application of the method is complicated. The purpose of this work is to introduce a new simple diffraction technique for the determination of experimental stress factors and the absolute magnitude of residual stresses in thin films. In the first step, the technique is used to determine stress factors of thin films deposited on Si(100) substrates by combination of substrate curvature and elastic strain characterization. Secondly, the experimental stress factors are used to determine the residual stress in chemically and structurally identical thin films deposited on bulk steel substrates. This approach is demonstrated for nanocrystalline CrN and TiN thin films.

A.2 Assumptions and methodology

The majority of thin films deposited on solid substrates possess a certain amount of residual stress originating usually from the deposition procedure and the films thermal history. Following the general condition of mechanical equilibrium, the integration of the stress over the whole thin-filmsubstrate composite yields [2]

$$\int_V \sigma_{ij} dV = 0 \tag{A.1}$$

When the thin film is deposited on a relatively thin substrate, the residual stress and the balanced mechanical moments between film and substrate cause a bending of the composite. When the thin film is deposited on a substrate with known mechanical properties and the film thickness is at least 100 times smaller than that of the substrate, the radius of the substrate curvature R can be used to determine the stress imposed on the films using the Stoney formula [10],

$$\sigma_{\mathrm{C}}^{S} = \frac{E}{6\,(1-\nu)}\frac{h_{\mathrm{s}}^{2}}{h_{\mathrm{f}}}\frac{1}{R} \tag{A.2}$$

where h_{s} and h_{f} represent the substrate and film thickness, respectively, and the term $E/(1-\nu)$ is the biaxial modulus of the substrate. In this work, monocrystalline Si(100) wafers with the modulus of 181 GPa [11] were chosen to limit the possible experimental errors. The modulus of Si(100) is well defined, therefore the only possible source of error is in the measurement of the curvature R and the thickness parameters h_{s} and h_{f}.

σ_{C}^{S} in Eq. A.2 represents the macroscopic residual stress in the film calculated using the curvature method (denoted by letter C) and expressed in the sample coordinate system S (Fig. A.1). Using a powder diffractometer equipped with two axes (θ/θ goniometer), the substrate curvature R can be determined by the measurement of rocking curves on substrate symmetrical reflections (*e.g.* Si 400) at different sample positions x_i as demonstrated in Fig. A.2(a). The radius of substrate curvature can be calculated according to [12]

$$R = \frac{\Delta x}{2\sin(\Delta\omega/2)} \tag{A.3}$$

For a homogeneous thin film that is unpassivated, the stress state in the plane of the film can be considered isotropic and biaxial according to

$$\sigma_{11}^{S} = \sigma_{22}^{S} = \sigma_{\mathrm{C}}^{S},\ \sigma_{12}^{S} \cong 0 \ \textit{and}\ \sigma_{i3}^{S} \cong 0. \tag{A.4}$$

The residual stress state in the thin film corresponds to spatially uniform deformation of the stress-free plane in the substrate (Fig. A.1). If the substrate is under the film, concave

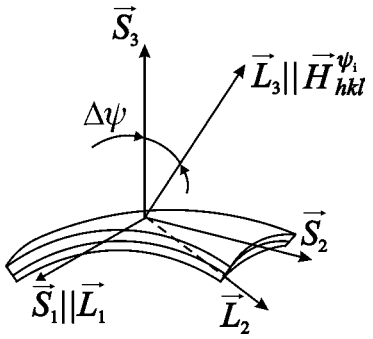

Figure A.1: Definition of the coordinate systems used in this work. S and L refer to the sample and laboratory coordinate systems, respectively. The diffraction characterization of a sample at different tilt angles ψ_i allows the determination of the elastic strain in the film.

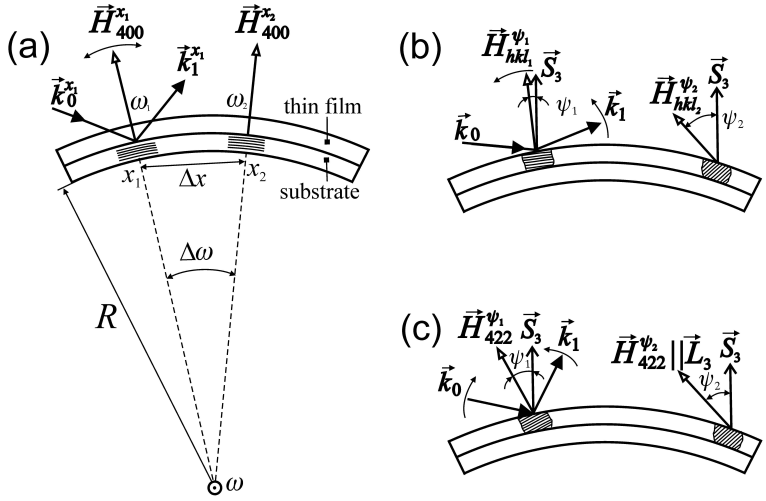

Figure A.2: Schematic description of the diffraction procedures used in this work. (a) The characterization of the radius of substrate curvature R was performed by measuring rocking curves of Si 400 reflections, locking the angle between the primary $\vec{k}_0$ and secondary $\vec{k}_1$ diffraction vectors to 69.13°. The measurements were performed at different sample positions x_i , differing 2 mm laterally. From the angular positions ω_i, the corresponding angle $\Delta\omega$ between the scattering vectors $\vec{H}^{x_i}_{400}$ was determined. (b) Applying a detector scan mode and a constant incident angle of 5°, the lattice spacings of various TiN and CrN $(hkl)_i$ crystallographic planes with specific diffraction vectors $\vec{H}^{\psi_i}_{hkl}$ forming different angles ψ_i with the sample normal S_3 were determined. (c) Elastic strains in TiN and CrN were determined by the characterization of 422 reflections at different sample tilt angles ψ_i.

and convex bending of the composite corresponds to tensile and compressive stresses in the film, respectively. Due to the in-plane symmetry and the spherical deformation of the stressfree plane in the substrate, the magnitude of the residual stress can be determined from the substrate curvature measurement performed along an arbitrary in-plane direction. Similarly, the magnitude of elastic deformation in the film can be determined by the diffraction measurement of crystallographic planes oriented parallel to any in-plane film direction. For this reason, the characterization of residual stress in the film can be performed by tilting the sample around one goniometer axis lying in the film surface: the so-called ω geometry.

Consequently, the diffraction scan of an *hkl* reflection with the scattering vector $\vec{H}^{\psi}_{hkl}$, carried out at an orientation specified by angle ψ (Figs. A.1, A.2b and A.2c), can be used to determine the average interplanar spacing of the family of crystallographic planes (*hkl*). Applying the unstressed lattice spacing d_0^{hkl} , the experimental elastic strain ϵ_{ψ}^{hkl} along the direction L_3 (Figs. A.1 and A.2c) is consistent with the component $\left\{\epsilon_{33}^{L}\right\}_{\psi}^{hkl}$ (of the strain tensor $\left\{\epsilon_{ij}^{L}\right\}^{hkl}$ defined in the L system) and can be expressed as

$$\epsilon_{\psi}^{hkl} = \frac{d_{\psi}^{hkl} - d_0^{hkl}}{d_0^{hkl}} = \left\{\epsilon_{33}^{L}\right\}_{\psi}^{hkl} = a_{3i}a_{3j}\left\{\epsilon_{ij}^{S}\right\}^{hkl} \tag{A.5}$$

where $\left\{\epsilon_{ij}^{S}\right\}^{hkl}$ is the elastic strain in the sample coordinate system S and a_{ij} is a rotation matrix characterizing the transformation between laboratory L and sample S coordinate systems (Fig. A.1). The measured elastic strain calculated for the reflection *hkl* and for the sample orientation defined by angle ψ can be related to the macroscopic stress as follows:

$$\left\{\epsilon_{33}^{L}\right\}_{\psi}^{hkl} = F_{ij}(hkl,\psi)\sigma_{ij}^{S}. \tag{A.6}$$

The stress factors $F_{ij}(hkl,\psi)$ represent a tensor function [13]. Considering the conditions in Eq. A.4 and the in-plane isotropic biaxial stress state,

$$\left\{\epsilon_{33}^{L}\right\}_{\psi}^{hkl} = \left[F_{11}(hkl,\psi) + F_{22}(hkl,\psi)\right]\sigma_{\mathrm{D}}^{S}, \tag{A.7}$$

where σ_{D}^{S} represents the macroscopic in-plane residual stress determined by a diffraction measurement (denoted by letter D). The term σ_{D}^{S} represents a quantity depending significantly on the size of the irradiated volume, and on the sample position from which the scattering signal originates, and is associated only with one crystalline phase of the film. The term σ_{C}^{S} (Eq. A.2) expresses the macroscopic deformation imposed on the film as a geometrical and a mechanical element whereby the composition, the structure of the film, the number of phases, as well as the physical inhomogeneity within the film, are not considered [14]. If the lattice-spacing characterization is performed on the representative film volume consisting of only one phase and the mechanical state of that volume can be assessed by the Stoney formula, the measured elastic strain $\left\{\epsilon_{ij}^{S}\right\}^{hkl}$ (Eq. A.7) then be related to the macroscopic stress σ_{C}^{S} (Eq. A.2). Inserting

the macroscopic in-plane residual stress σ_{C}^{S} (Eq. A.2) calculated using the curvature method into Eq. A.7 ($\sigma_{\mathrm{D}}^{S} = \sigma_{\mathrm{C}}^{S}$), the stress factor $F_{11}(hkl,\psi) + F_{22}(hkl,\psi)$ component can be readily determined for the specific thin film. This provides an opportunity to determine experimental stress factors $F_{ij}(hkl,\psi)$ on the basis of the static diffraction measurement, which allows linking of the macroscopic stress imposed on the film and the elastic response of the crystal lattice of the specific phase. It should be emphasized that the experimental stress factors $F_{ij}(hkl,\psi)$ (Eq. A.6) express the mechanical properties of the specific thin film deposited under specific deposition conditions and being distinguished by distinct morphology, nanostructure, porosity, etc. Consequently, the experimental stress factors can be applied to calculate residual stresses in thin films which possess identical or at least very similar structural and mechanical properties as that one on which the experimental stress factors $F_{ij}(hkl,\psi)$ were determined.

Subsequently, when characterizing another thin film which is structurally, chemically and mechanically identical to that used for the determination of stress factors, the unknown inplane residual stress σ_{U}^{S} in the film (distinguished by the letter U) can be calculated according to

$$\sigma_{\mathrm{U}}^{S} = \frac{\left\{\epsilon_{33}^{L}\right\}_{\psi}^{hkl}}{[F_{11}(hkl,\psi) + F_{22}(hkl,\psi)]}, \tag{A.8}$$

whereby $\left\{\epsilon_{33}^{L}\right\}_{\psi}^{hkl}$ represents the diffraction data obtained from the film with unknown stresses. It must be emphasized here that the characterization of the new thin film with the unknown stress σ_{U}^{S} should be performed under identical experimental conditions (same *hkl* reflection choice and sample tilt angles ψ_i) as were used to characterize stress factors.

When strain characterization is performed at N distinct sample orientations specified by the angles ψ_i, the unknown stress σ_{U}^{S} is

$$\sigma_{\mathrm{U}}^{S} = \frac{1}{N}\sum_{i=1}^{N} \frac{\left\{\epsilon_{33}^{L}\right\}_{\psi_i}^{hkl_i}}{\{F_{11}[(hkl)_i,\psi_i] + [F_{22}(hkl)_i,\psi_i]\}}. \tag{A.9}$$

Eq. A.9 can be simplified and the unknown residual stress σ_{U}^{S} can be expressed as

$$\sigma_{\mathrm{U}}^{S} = \sigma_{\mathrm{C}}^{S} \frac{\sum_{i=1}^{N}\left|\left\{d_{\psi_i}^{hkl}\right\}_{\mathrm{U}} - d_0^{hkl}\right|}{\sum_{i=1}^{N}\left|\left\{d_{\psi_i}^{hkl}\right\}_{\mathrm{C}} - d_0^{hkl}\right|} \tag{A.10}$$

where $\left\{d_{\psi_i}^{hkl}\right\}_{\mathrm{U}}$ and $\left\{d_{\psi_i}^{hkl}\right\}_{\mathrm{C}}$ represent lattice-spacing measurements performed on the sample with unknown stress (U) and on the sample (C) where the macroscopic stress σ_{C}^{S} was determined using the curvature method, respectively. In this section, the methodology was formulated to allow the information from the residual stress characterization performed using the curvature method and the elastic strains determined using diffraction at different sample tilt angles ψ to be combined. Generally, thin films possessing a residual stress are in a state of recovery and, with time, the stress can

relax. This effect is observed especially in the case of metallic films. For this reason, when determining the experimental stress factors, the characterization of the macroscopic stress and the elastic strain should be performed within a relatively short time interval.

A.3 Experiment

TiN and CrN thin films were deposited using reactive magnetron sputtering in laboratory-scale (TiN, [15], [16]) and industrial-scale (CrN, Balzers RCS) deposition systems. Monocrystalline Si(100) wafers with thicknesses of 124 and 325 μm and dimensions 30 x 7 mm were used. The wafers were covered with Si_xO_{1-x} and Si_xN_{1-x} layers, each with thickness 50 nm. Additionally, steel substrates with the lateral dimensions 10 x 10 mm and thickness 1 mm were prepared by mechanical and subsequent electrolytic polishing. The substrates were ultrasonically cleaned in acetone and alcohol prior to deposition. A TiN thin film with thickness of 0.5 mm was deposited on steel and on 124 mm thick Si(100) substrates during one deposition run in which the substrate temperature was 753 K. Similarly, a 3 μm thick CrN thin film was deposited on steel and on 325 μm thick Si(100) substrates at a temperature of 623 K.

The structural characterization of the films was performed under laboratory conditions using a powder diffractometer equipped with two circles (θ/θ goniometer) enabling movement of the X-ray source (tube) and the detector independently, whereby the sample is fixed and the film surface is oriented horizontally. The main reason for the use of this type of goniometer was to verify the approach of applying a relatively simple laboratory device. The setup comprised Cu K_α radiation, a parallel beam produced by an X-ray mirror, line focus and an energy dispersive point detector. The samples were characterized using the following approaches.

(a) The radius of curvature of two Si(100) substrates was determined by the measurement of rocking curves of Si 400 reflections by locking the X-ray source and the detector to the 2θ value of 69.13°. The measurements were performed at different sample positions x_i, differing 2 mm laterally. From the angular positions ω_i, the corresponding angle $\Delta\omega$ between the scattering vectors $\vec{H}_{400}^{x_i}$ was determined (Fig. A.2a).

(b) After setting the incident angle to 5°, the diffraction scans were measured using the detector scan mode applying the 2θ range of 33-155°. In this way, the lattice spacings of various (hkl) crystallographic planes with specific diffraction vector $\vec{H}_{hkl_i}^{\psi_i}$ forming different angles ψ_i with the sample normal S_3 were determined (Fig. A.2b).

(c) The lattice spacing d_ψ^{hkl} of TiN and CrN 422 reflections was determined at different sample tilt angles ψ_i. The angles between the sample normal S_3 and the diffraction vector $\vec{H}_{422}^{\psi_i}$ were 0, 18, 26, 33, 39, 45, 51 and 57°, resulting in a $\Delta \sin^2\psi$ step of 0.1 (Fig. A.2c).

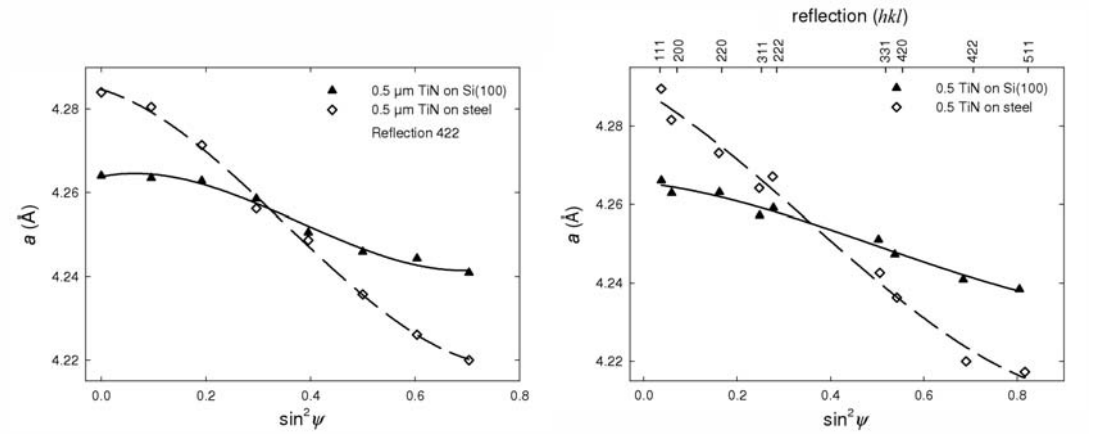

Figure A.3: $\sin^2\psi$ plots for the 0.5 μm TiN thin film deposited on 124 μm thick Si(100) and on 1 mm thick steel substrates are represented by filled and empty symbols, respectively. The lattice parameters were obtained by the measurement of (a) 422 and (b) various *hkl* reflections, applying the procedures described in Figs. A.2(c) and A.2(b), respectively. The maximal standard error is 0.0003 Å.

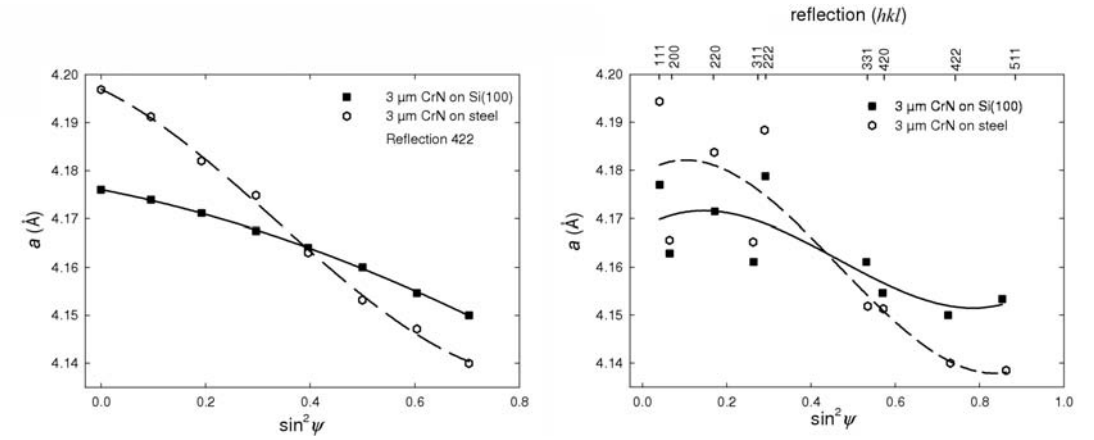

Figure A.4: $\sin^2\psi$ plots for the 3 μm CrN thin film deposited on 325 μm thick Si(100) and on 1 mm thick steel substrates are represented by filled and empty symbols, respectively. The lattice parameters were obtained by the measurement of (a) 422 and (b) various *hkl* reflections applying the procedures described in Figs. A.2(c) and A.2(b), respectively. The maximal standard error is 0.0003 Å.

A.4 Results and discussion

In Figs. A.3(a) and A.4(a), the lattice parameters of TiN and CrN thin films determined by the diffraction measurement of 422 reflections [cf. (c) in §3] are presented as a function of $\sin^2\psi$. In Figs. A.3(b) and A.4(b), lattice parameters of TiN and CrN thin films determined by the measurement of various *hkl* reflections [cf. (b) in §3] are presented. The data in Figs. A.3 and A.4 show that the dependencies are not linear

and cannot therefore be evaluated by applying isotropic X-ray elastic constants (XEC) s_1 and $\frac{1}{2}s_2$ [2].

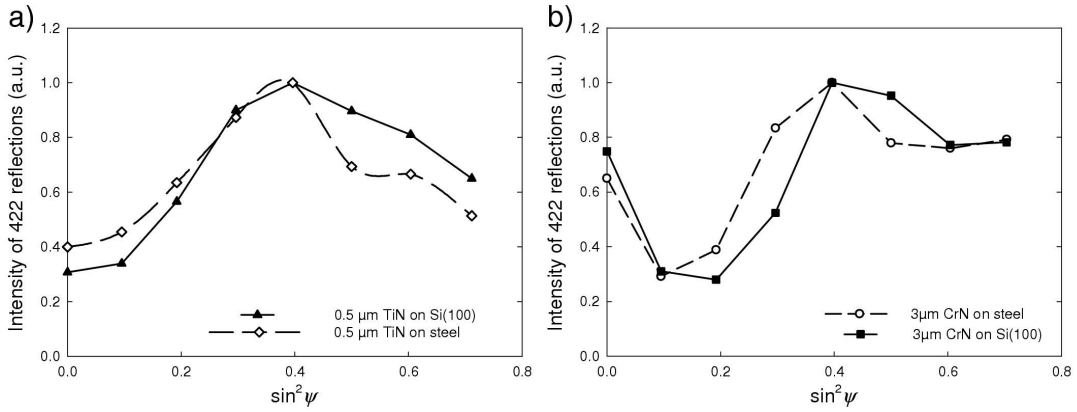

Figure A.5: Intensity as a function of ψ collected at 2θ positions corresponding to 422 reflections. The results indicate that the films deposited on different substrates possessed very similar preferred orientations.

Samples from Figs. A.3 and A.4 were additionally analysed by pole-figure measurements. The results indicated that TiN and CrN films possessed fibre textures with more fibre components. In Fig. A.5, intensity distributions as a function of angle show that the films possess a similar preferred orientation. It should be noted that the four samples analysed in this work were selected from a larger set of samples, where the similarities in texture between samples deposited on Si(100) and steel were the main criteria. Further, it was assumed that the TiN and CrN deposited on different substrates possess very similar mechanical and structural properties and therefore the conditions specified in §2 apply.

The dependencies in Figs. A.3(a) and A.4(a) were fitted using cubic polynomial functions and the unstressed parameters a_0 of TiN and CrN were determined from the interception of $\sin^2\psi$ plots (Tab. A.1). Considering the measurement errors and the scattering of the data in Figs. A.3(a) and A.4(a), the error associated with the a_0 determination was estimated to be 0.001 Å[17]. For comparison, a similar procedure was applied to the plots in Figs. A.3(b) and A.4(b). It is assumed that the values extracted from Figs. A.3(a) and A.4(a) correspond to the real unstressed lattice parameters, whereas the values in Figs. A.3(b) and A.4(b) are only estimates, presented here for comparison.

The results from rocking-curve measurements performed on Si 400 reflections, namely the relative ω_i positions of the peaks as a function of x_i, are presented in Fig. A.6. The results indicate that, in the case of TiN/Si(100) structure, the thinner substrate serves as a more sensitive "sensor" to determine the curvature. The stress magnitude was calculated from the curvature data using Eq. A.2 and indicates relatively high compression in TiN and CrN films on Si(100) (Tab. A.1).

Experimental results of the elastic strain characterization (Figs. A.3 and A.4) and the macroscopic residual stresses (Tab. A.1) were used to calculate stress factors of

the films deposited on Si(100) using Eq. A.7. The stress factors for TiN and CrN films are presented in Fig. A.7.

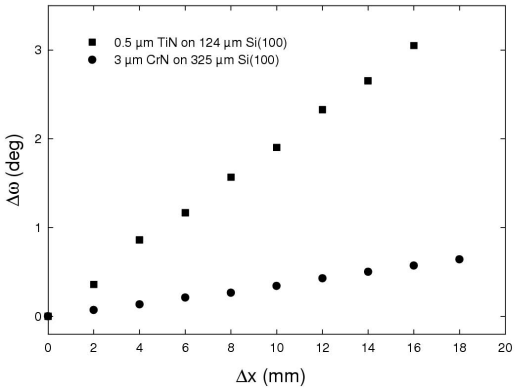

Figure A.6: Plots of $\Delta\omega$ dependence on Δx for TiN/Si(100) and CrN/(100) samples (Tab. A.1) obtained by the procedure of Fig. A.2(a). The results show different radii of substrate curvature R, which were used to calculate the macroscopic stress (Eqs. A.2 and A.2). The maximal standard error is 0.01°

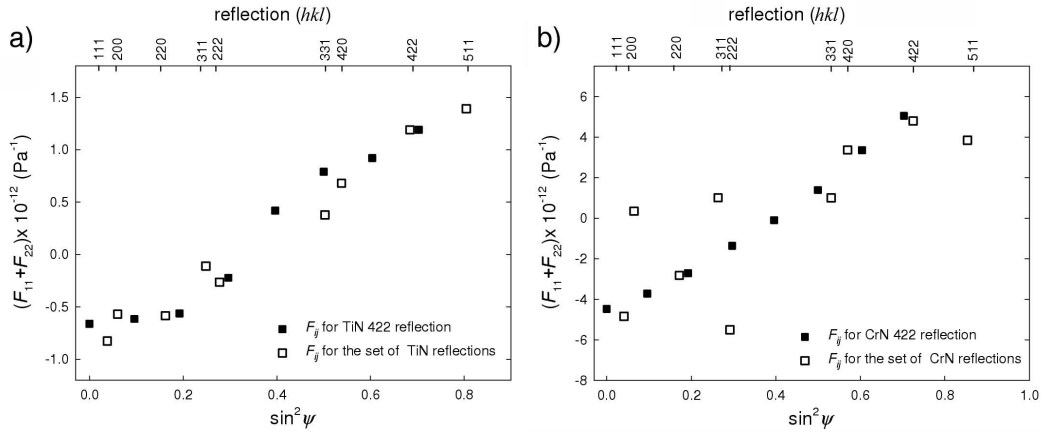

Figure A.7: Experimental stress factors for (a) TiN and (b) CrN thin films. The factors were calculated from the data in Figs. A.3 and A.4, applying Eq. A.10 and unstressed lattice parameters (Tab. A.1).

After determining the stress factors for the films deposited on Si(100), residual stresses were evaluated for the films deposited on steel. Applying the experimental stress factors (Eq. A.7) and the unstressed lattice parameter (Tab. A.1), the unknown stresses in TiN and CrN on steel were determined using Eqs. A.9 and A.10 (Figs. A.3(a) and A.4(a), and A.3(b) and A.4(b), and methods (c) and (b) in §3, respectively). The calculated stress values are presented in Tab. A.1 and show that the application of unstressed lattice parameters obtained using two procedures [namely from the intercepts in Figs. A.3(a) and A.4(a), and Figs. A.3(b) and A.4(b)] yields similar values. The maximum error associated with the determination of the stress values was estimated to be about 25%.

The results in Tab. A.1 show that the stresses in films on steel are about 2.4 times higher than those for films on Si(100). This can be explained by the specific mismatch of thermal expansion coefficients (TECs) of TiN, CrN, Si and steel [15, 18, 19]. Additionally, the stress values determined from the measurements performed using the procedures (b) and (c) in §3 are comparable and show that the method presented in this work is not sensitive to the reflection choice.

For practical purposes, the determination of the experimental stress factors can be $F_{11}\left[(hkl)_i, \psi_i\right] + F_{22}\left[(hkl)_i, \psi_i\right]$ performed only for one reflection hkl_i at the specific tilt angle ψ_i. The evaluation of the unknown residual stresses in other samples can then be carried out also on the basis of one reflection measurement and by applying the known stress factors. The critical point in this case is the determination of the unstressed lattice spacing d_0^{hkl} when calculating $F_{11}\left[(hkl)_i, \psi_i\right] + F_{22}\left[(hkl)_i, \psi_i\right]$ for the sample with known macroscopic stress σ_{C}^{S} (Eq. A.2). In this case, satisfactory data were obtained by the measurement of two diffraction peaks with relative large $\Delta\psi$ angular difference when determining $F_{11}\left[(hkl)_i, \psi_i\right] + F_{22}\left[(hkl)_i, \psi_i\right]$.

It should be noted that extensive experiments were performed also for other substrate thicknesses when testing the method presented in this work. It was found that the application of relatively thin substrates (about 100 μm or thinner) can result in the sample cracking. Conversely, the application of thick substrates often caused film rupture or resulted in very weak substrate bending which was not possible to characterize. Another problem occurred when films exhibited very low stress after deposition and therefore resulted in negligible substrate bending. For the above reasons, the selection of a substrate material with suitable thickness and TEC is an important prerequisite in order to apply the method presented in this work.

The TiN and CrN structures analysed in this work were selected from a larger set of samples in which the films were deposited on various substrates (*e.g.* Al_2O_3, SiO_2 , NaCl). It was observed that the films grow on some substrates with various preferred orientations or even heteroepitaxially. Therefore, the method presented in this work cannot be applied generally, but only in special cases. In the future, a general methodology should be formulated allowing the recalculation of the experimental stress factors for thin films possessing different textures.

The application of the Stoney formula (Eq. A.2) is not naturally limited only to monocrystalline substrates. Polycrystalline substrates with known mechanical properties can also be used as a mechanical sensor. In that case, the curvature of the

film/substrate composite can be determined by X-ray diffraction characterization of the orientation of the film fibre axis using ω scans at different sample positions.

It is believed that in the future this technique will be an effective method to study elastic interactions in nanoscale materials deposited on monocrystalline substrates, especially at high temperatures.

A.5 Conclusions

A new method for the determination of experimental stress factors in thin films on the basis of static diffraction measurements is introduced. The approach is based on the diffraction characterization of substrate curvature and lattice spacing at different sample tilt angles for the film/substrate structure, with the known mechanical properties of the substrate serving as a mechanical sensor and for calibration.

The new method is demonstrated for nanocrystalline TiN and CrN thin films deposited on Si(100) and steel substrates and characterized using a θ/θ goniometer. The characterization of the experimental stress factors and absolute residual stresses is straightforward and provides an opportunity to determine stresses in films exhibiting non-linear $\sin^2\psi$ in a rapid way.

This work was supported by the country of Styria within the project Multimethodenanalytik Nanoteilchen und Nanoteilchenverbunden, and by the Austrian NANO Initiative via a grant from the Austrian Science Fund FWF within the project Stress-Design Development of Fundamentals for Residual Stress Design in Coated Surfaces. A part of this work on thin-film deposition was also financially supported by the Christian Doppler Society and the companies Plansee AG (Reutte, Austria) and Balzers AG (Balzers, Liechtenstein).

Table A.1: Basic parameters and properties of the structures investigated.

The radius of curvature of the TiN/Si(100) and CrN/Si(100) structures was determined by the procedure described in §3(a) (Fig. A.2a). The residual stresses in those structures were calculated using the Stoney formula. The unstressed lattice spacing a_0 was estimated from the intersection of the $\sin^2\psi$ plots. The stresses in TiN and CrN films on steel were calculated on the basis of measurements of 422 and *hkl* reflections.

Thin film	Substrate thickness	Radius of curvature (m)	Stress curvature (MPa)	a_0 from 422 (Å)	Stress $\sin^2\psi$ from 422 (MPa)	a_0 from *hkl* (Å)	Stress $\sin^2\psi$ from *hkl* (MPa)
0.5 μm TiN	Si(100):124 μm	0.31	-2932	4.2558		4.2552	
0.5 μm TiN	Steel:1 mm				-7062		-7153
3 μm CrN	Si(100):325 μm	1.61	-655	4.1640		4.1632	
3 μm CrN	Steel:1 mm				-1535		-1671

A.6 References

[1] Dölle, H. *J. Appl. Cryst.* **12**, 489–501 (1979).

[2] Noyan, I. C. and Cohen, J. B. *Residual Stress Measurement by Diffraction and Interpretation.* Springer, (1987).

[3] Marion, R. and Cohen, J. B. *Adv. X-ray Anal.* **20**, 355–367 (1977).

[4] Pina, J., Dias, A., and Lebrun, J. L. *Mater. Sci. Eng. A* **267**(1), 130–144 (1999).

[5] Renault, P. O., Bourhis, E. L., Villain, P., Goudeau, P., Badawi, K. W., and Faurie, D. *Appl. Phys. Lett.* **83**, 473–475 (2003).

[6] Barral, M., Lebrun, J., Sprauel, J., and Maeder, G. *Metall. Mater. Trans. A* **18**(7), 1229–1238 (1987).

[7] Hauk, V. *Structural and Residual Stress Analysis by Nondestructive Methods.* Elsevier, Amsterdam, (1997).

[8] Houtte, P. v. and De Buyser, L. *Acta Mater.* **41**(2), 323–336 (1993).

[9] Welzel, U., Leoni, M., and Mittemeijer, E. J. *Philos. Mag.* **83**(5), 603–630 (2003).

[10] Stoney, G. G. *Proc. Phys. Soc. London, Sect. A* **82**, 172 (1909).

[11] Suresh, S. and Freund, L. B. *Thin Film Materials Stress, Defect Formation and Surface Evolution.* Cambridge University Press, Cambridge, (2003).

[12] Segmüller, A., Noyan, I. C., and Speriosu, V. S. *Prog. Cryst. Growth Charact. Mater.* **18**, 21–66 (1989).

[13] Ortner, B. *J. Appl. Cryst.* **39**, 401–409 (2006).

[14] Rant, S. J., Goldsmith, C. C., and Noyan, I. C. *Adv. X-ray Anal.* **37**, 157165 (1994).

[15] Mayrhofer, P. H., Kunc, F., Musil, J., and Mitterer, C. *Thin Solid Films* **415**(1-2), 151–159 (2002).

[16] Kutschej, K., Mayrhofer, P. H., Kathrein, M., Polcik, P., Tessadri, R., and Mitterer, C. *Surf. Coat. Technol.* **200**(7), 2358–2365 (2005).

[17] Winholtz, R. A. and Cohen, J. B. *Aust. J. Phys.* **41**(2), 189–199 (1988).

[18] Hultman, L. *Vacuum* **57**(1), 1–30 (2000).

[19] Mitterer, C., Mayrhofer, P. H., and Musil, J. *Vacuum* **71**(1-2), 279–284 (2003).

B

Stress factors and absolute residual stresses in thin films determined by the combination of curvature and $\sin^2\psi$ methods

K.J. Martinschitz[a], E. Eiper[a], J. Keckes[a]

[a]Erich Schmid Institute of Materials Science, Austrian Academy of Sciences, A–8700 Leoben, Austria

Abstract A new method is presented which allows the determination of experimental stress factors in anisotropic thin films on the basis of static diffraction measurement. The method is based on the simultaneous characterization of macroscopic stress and elastic strain in thin film using substrate curvature and $\sin^2\psi$ methods, respectively. The curvature of monocrystalline substrate with known mechanical properties is determined using rocking curve measurements on substrate symmetrical reflections. The experimental stress and strain values are used to calculate stress factors for the specific film as a function sample tilt angle and reflection measured. The approach represents a relatively simple recipe to determine residual stress magnitude in thin films on the absolute scale. The procedure is demonstrated on polycrystalline Cu thin film deposited on Si(100).

B.1 Introduction

The determination of residual stresses in thin films requires an application of stress factors F_{ij} expressing the elastic properties of the material and linking experimental elastic strain and unknown residual stress [1]. The application of stress factors is necessary especially in the case of anisotropic thin films where the elastic properties depend on sample orientation. One possibility to determine the stress factors *experimentally* is the *in-situ* determination of elastic strains as a function of external mechanical load applied to the film [2, 3]. The mechanical loading is usually performed by four-point bending or by tensile straining while the in-situ technique requires the use of dedicated diffractometer attachments. Alternatively, theoretical stress factors of thin films can be calculated on the basis of single crystal elastic constants, the orientation distribution function and the supposed elastic interaction between the grains [4–6]. The calculation of stress factors is usually a laborious task since the orientation distribution function of the crystallites must be determined experimentally and the application of the specific elastic interaction model is not trivial. Another problem lies in the fact that the theoretical stress factors are calculated on the basis of bulk elastic constants of known materials. For new or non-stoichiometric materials with unknown compliances, the application of the method is complicated. The main aim of this contribution is to introduce a simple experimental procedure which allows the determination of experimental stress factors in thin films with arbitrary texture on the basis of static diffraction measurement. The approach is based on the combination of substrate curvature and $\sin^2\psi$ method and is demonstrated on Cu thin film deposited on monocrystalline Si(100) substrate.

B.2 Methodology

Strain characterization by diffraction (Fig. B.1) provides information on the local mechanical properties of thin film. When performed with a relatively large X-ray beam (few mm^2 in cross section), a sufficiently large volume is irradiated and the diffraction data can be considered to express statistically representative information on the structural properties and mechanical state of the film on the macroscopic level. Furthermore, it can be supposed that the thin film is homogeneous, in-plane isotropic and the equilibrium conditions for a free surface are valid. Consequently, the residual stresses σ_{ij} in thin film can be considered as biaxial and in-plane isotropic whereby following conditions can be applied [7]

$$\sigma_{11} = \sigma_{22},\ \sigma_{12} \cong 0\ and\ \sigma_{i3} \cong 0. \tag{B.1}$$

The diffraction scan of hkl reflection with the scattering vector $\vec{H}^{\psi}_{hkl}$ carried out at a sample orientation specified by angle ψ (Fig. B.1b) can be used to determine an average interplanar spacing d^{hkl}_{ψ} of the family of crystallographic planes (hkl). Applying the unstressed lattice spacing d^{hkl}_{0}, the experimental elastic strain ϵ^{hkl}_{ψ} along the diffraction vector $\vec{H}^{\psi}_{hkl}$ (Fig. B.1b) can be expressed as

$$\epsilon_{\psi}^{hkl} = \frac{d_{\psi}^{hkl} - d_0^{hkl}}{d_0^{hkl}} = F_{ij}(hkl, \psi)\sigma_{ij}. \tag{B.2}$$

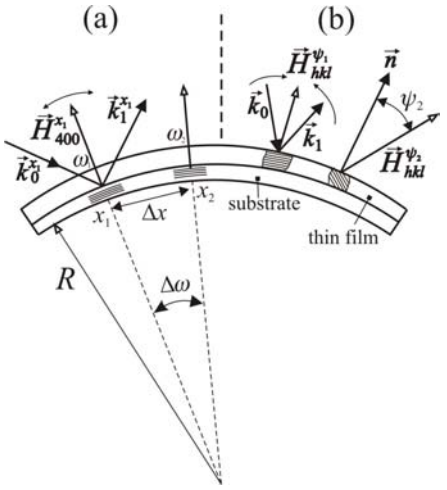

Figure B.1: A schematic description of the diffraction procedures. (a) The radius of substrate curvature R was determined by measuring rocking curves of Si 400 reflections locking the angle between the primary $\vec{k}_0$ and secondary $\vec{k}_1$ diffraction vectors to 69.13 degrees. The measurements were performed at different sample positions x_i differing 1 mm laterally and, from the angular positions ω_i , the corresponding angle $\Delta\omega$ between the scattering vectors $\vec{H}_{400}^{x_i}$ was determined (b) Elastic strains in Cu film were determined by the characterization of hkl reflections at different sample tilt angles ψ_i where ψ_i represent the angle between sample normal $\vec{n}$ and the diffraction vector $\vec{H}_{hkl}^{\psi_i}$.

The stress factors $F_{ij}(hkl, \psi)$ depend on the specific reflection measured, sample orientation, orientation distribution function and elastic interaction between the grains. Considering the condition Eq. B.1 and in-plane isotropic biaxial stress state

$$\epsilon_{\psi}^{hkl} = (F_{11}(hkl, \psi) + F_{22}(hkl, \psi)\sigma_{11}^{\mathrm{D}}, \tag{B.3}$$

where σ_{11}^{D} represents the in-plane residual stress determined by a diffraction measurement (specified by letter D).

When the thin film is deposited on a substrate with known mechanical properties, like monocrystalline Si(100), and the film thickness is at least 100 times smaller than that of the film, the radius of the substrate curvature R can be used to determine the stress imposed on the films using the Stoney formula [8].

$$\sigma^{\mathrm{C}} = \frac{E}{6\,(1-\nu)} \frac{h_{\mathrm{s}}^2}{h_{\mathrm{f}}} \frac{1}{R}, \tag{B.4}$$

where h_{s} and h_{f} represent the substrate and film thickness, respectively, and the term $E/(1-\nu)$ is the biaxial modulus of the substrate. σ^{C} represents the macroscopic residual stress in the film calculated using the curvature method (specified by letter C). The substrate curvature R can be determined by the measurement of rocking

curves on substrate symmetrical reflections (*e.g.* Si 400) at different sample positions x_i as demonstrated in Fig. B.1b. The radius of substrate curvature can be calculated according [9]

$$R = \frac{\Delta x}{2\sin(\frac{\Delta\omega}{2})}. \tag{B.5}$$

Supposing the lattice spacing characterization is performed on the representative film volume consisting only of one phase and the mechanical state of that volume can be assessed by the Stoney formula, the measured elastic strain ϵ_ψ^{hkl} (Eq. B.2) can be related to the macroscopic stress σ^{C} (Fig. B.4). By inserting the macroscopic in-plane residual stress σ^{C} (Eq. B.4) calculated using the curvature method into Eq. B.3 (σ_{11}^{D}=σ^{C}), the stress factor component $F_{11}(hkl,\psi) + F_{22}(hkl,\psi)$ can be easily determined for the specific thin film.

$$(F_{11}(hkl,\psi) + F_{22}(hkl,\psi)) = \frac{\epsilon_\psi^{hkl}}{\sigma^{\mathrm{C}}}. \tag{B.6}$$

It should be emphasized that the experimental stress factors $F_{11}(hkl,\psi)+F_{22}(hkl,\psi)$ (Eq. B.6) express the mechanical properties of the specific thin film deposited under specific deposition conditions and being distinguished by distinct morphology, nanostructure, porosity, *etc.* Subsequently, when characterizing another thin film which is structurally, chemically and mechanically identical with that used for the determination of stress factors, the stress factors $F_{11}(hkl,\psi) + F_{22}(hkl,\psi)$ can be used to determine the residual stress in the film. In case the strain characterization is performed at N distinct sample orientations specified by the angles ψ_i, the unknown stress σ_{11}^{U} can be calculated according

$$\sigma_{11}^{\mathrm{U}} = \sigma^{\mathrm{C}} \frac{\sum_{i=1}^{N} \left| \left\{ d_{\psi_i}^{hkl} \right\}_{\mathrm{U}} - d_0^{hkl} \right|}{\sum_{i=1}^{N} \left| \left\{ d_{\psi_i}^{hkl} \right\}_{\mathrm{C}} - d_0^{hkl} \right|} \tag{B.7}$$

where $\left\{ d_{\psi_i}^{hkl} \right\}_{\mathrm{U}}$ and $\left\{ d_{\psi_i}^{hkl} \right\}_{\mathrm{C}}$ represent lattice spacing of the sample with unknown stress (U) and of the sample (C) where the macroscopic stress σ^{C} was determined using the curvature method, respectively.

B.3 Experiment

A 140 μm thick rectangular Si(100) wafer with the dimensions of 5 x 35 mm^2 was used as a substrate. The wafer was cleaned using isopropanol and acetone and, moreover, ion etching was applied before the Cu deposition to remove contaminants from the surface. Cu thin film with different thickness 2.7 μm was deposited by balanced magnetron sputtering using a copper target, in argon atmosphere at room temperature. The sample was annealed in N_2 atmosphere at 400 °Cfor 10 minutes in order to increase the residual stress magnitude in the film. The structural characterization of

the Cu/Si(100) structure was performed under laboratory conditions using a powder diffractometer equipped with two circles (θ/θ goniometer) enabling to move the X-ray source (tube) and the detector independently whereby the sample is fixed and the film surface is oriented horizontally. The setup included CuK_α radiation, a parallel beam produced by an X-ray mirror, line focus and an energy dispersive point detector. The sample was characterized using two following approaches:

(a) the radius of curvature of Si(100) substrate was determined by the measurement of rocking curves of Si 400 reflections by locking the X-ray source and the detector to the 2θ value of 69.13 degrees. The measurements were performed at different sample positions x_i differing 1 mm laterally and, from the angular positions ω_i, the corresponding angle $\Delta\omega$ between the scattering vectors $\vec{H}_{400}^{x_i}$ were determined (Fig. B.1a).

(b) the lattice spacing d_ψ^{hkl} of Cu 420, 400 and 222 reflections were determined at different sample tilt angles ψ_i (Fig. B.1b).

B.4 Results and Discussion

Results from rocking curve measurements on symmetrical Si 400 reflections, namely the relative ω_i position of the peak as a function of x_i, are presented in Fig. B.2. The ratio $\Delta\omega/\Delta x$ was used to calculate the radius of substrate curvature R=1.84 m and the macroscopic stress imposed on the film σ^{C} =118 MPa applying $E/(1-\nu)$=181 GPa (Eqs. B.4, B.5).

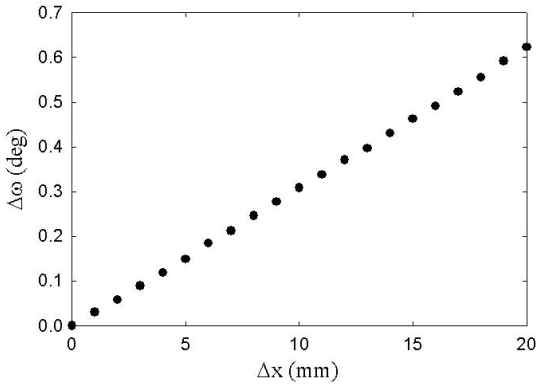

Figure B.2: A plot of $\Delta\omega$ dependence on Δx (Fig. B.1a). The result documents a specific radius of substrate curvature R=1.84 m which was used to calculate the macroscopic stress σ^{C} in the Cu film (Figs. B.4, B.5).

In Fig. B.3, $\sin^2\psi$ plot for Cu 420,400 and 222 reflections are shown. The different slopes of the linear dependencies document anisotropy of the Cu thin film. The intercept of the curves yields the unstressed lattice parameter $a_0 = 3.6147 \pm 0.0005$ Å. Following the usual data evaluation procedure, the results in Fig. B.2 can be used to determine the residual stress in the Cu thin film using appropriate X-ray elastic constants s_1^{hkl} and $\frac{1}{2}s_2^{hkl}$. In this work, a different approach is applied. The experimental data from Fig. B.2 and the known macroscopic stress σ^{C} =118 MPa are used

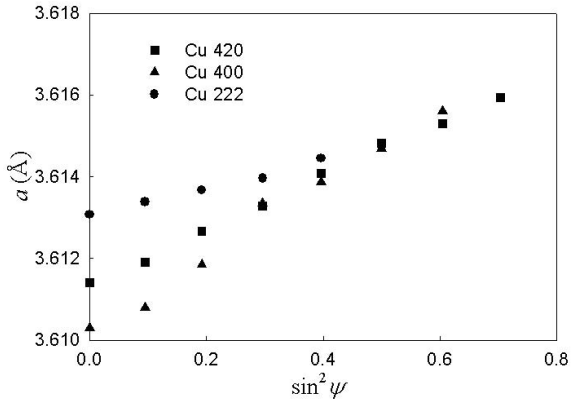

Figure B.3: $\sin^2\psi$ plots for 2.7 μm Cu thin film deposited on 140 μm thick Si(100) substrate. The lattice parameters were obtained by the measurement of Cu hkl reflections with the precision ± 0.0003 Å at different sample tilt angles ψ_i applying the procedures described in Fig. B.1b.

to calculate experimental stress factors $F_{11}(hkl,\psi) + F_{22}(hkl,\psi)$ using Eq. B.6 and applying the condition $\sigma_{11}^{\mathrm{D}} = \sigma^{\mathrm{C}}$.

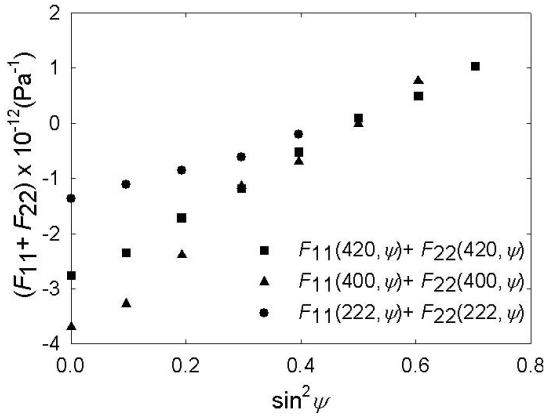

Figure B.4: Experimental stress factors $F_{11}(hkl,\psi) + F_{22}(hkl,\psi)$ calculated using Eq. B.6 on the basis of the diffraction measurements in Fig. B.2 and the macroscopic stress σ^{C}=118 MPa determined using Eq. B.4.

The stress factors in Fig. B.4 characterize the mechanical response of the Cu thin film which is in the state of creep. The factors are dependent on the sample tilt angle ψ and also on the specific reflection hkl. Consequently, the factors can by applied to determine the absolute magnitude of residual stress in structurally identical or comparable thin film deposited on any type of substrate using Eq. B.7. Since the stress factors were calculated for distinct ψ_i orientations this procedure can be easily applied also in the case of thin films exhibiting non-linear $\sin^2\psi$ plots. In the future, it is planed to use the relatively simple method to determine the stress factors at high

temperatures.

B.5 Summary

A methodology to determine experimental stress factors in anisotropic thin films by combing substrate curvature and $\sin^2\psi$ methods is formulated. The approach allows to determine absolute residual stresses in thin films. The approach is applied to polycrystalline Cu thin film deposited on Si(100) serving as a mechanical calibration.

B.6 Acknowledgement

This work was supported by the country of Styria within the project Multimethodenanalytik Nanoteilchen und Nanoteilchenverbunden and by the Austrian NANO Initiative via a grant from the Austrian Science Fund FWF within the project "StressDesign - Development of Fundamentals for Residual Stress Design in Coated Surfaces".

B.7 References

[1] Dölle, H. *J. Appl. Cryst.* **12**, 489–501 (1979).

[2] Marion, R. and Cohen, J. B. *Adv. X-ray Anal.* **20**, 355–367 (1977).

[3] Pina, J., Dias, A., and Lebrun, J. L. *Mater. Sci. Eng. A* **267**(1), 130–144 (1999).

[4] Barral, M., Lebrun, J., Sprauel, J., and Maeder, G. *Metall. Mater. Trans. A* **18**(7), 1229–1238 (1987).

[5] Houtte, P. v. and De Buyser, L. *Acta Mater.* **41**(2), 323–336 (1993).

[6] Welzel, U., Leoni, M., and Mittemeijer, E. J. *Philos. Mag.* **83**(5), 603–630 (2003).

[7] Noyan, I. C. and Cohen, J. B. *Residual Stress Measurement by Diffraction and Interpretation.* Springer, (1987).

[8] Stoney, G. G. *Proc. Phys. Soc. London, Sect. A* **82**, 172 (1909).

[9] Segmüller, A., Noyan, I. C., and Speriosu, V. S. *Prog. Cryst. Growth Charact. Mater.* **18**, 21–66 (1989).

Stress evolution in CrN/Cr coating systems during thermal straining

K.J. Martinschitz[a], R. Daniel[b], C. Mitterer[b] and J. Keckes[a]

[a]Erich Schmid Institute of Materials Science, Austrian Academy of Sciences and Department of Materials Physics, University of Leoben, Leoben, Austria
[b]Department of Physical Metallurgy and Materials Testing, University of Leoben and Christian-Doppler Laboratory for Advanced Coatings, University of Leoben, Leoben, Austria

Abstract CrN, Cr and CrN/Cr coatings were deposited at 350 °C on monocrystalline Si(100) and polycrystalline austenitic stainless steel substrates by magnetron sputtering using Cr targets in Ar + N_2 atmosphere. The stress evolution in the coating systems were characterized using X–ray diffraction and wafer curvature technique in the temperature range of 25-550 °C. Both techniques revealed larger stresses in coatings deposited on the steel substrates. The heat treatment reduces the deposition point defect concentration, which is reflected in a decrease of intrinsic stresses in Cr and CrN coatings. Additionally, roughness of the Cr films decreases. The stresses in the individual sublayers of the CrN/Cr bilayer coatings indicate that the constraint imparted by the CrN layer on the buried Cr layer prevents a stress relaxation in Cr since no stress hysteresis is observed during heating and cooling. The intrinsic stresses of CrN are $-3.4 * 10^9$ Pa on the steel substrate and $-1.7 * 10^9$ Pa on the Si(100) substrate. For Cr intrinsic stresses of $-1.35 * 10^9$ Pa are obtained on steel and $-0.7 * 10^9$ Pa on Si(100). The intrinsic stresses of CrN in the CrN/Cr bilayer system remains at $-3.4 * 10^9$ Pa on the steel but increases to $-2.8 * 10^9$ Pa on the Si(100) substrate. As a result of the annealing cycle, a stress relaxation of approximately $1.3 * 10^9$ Pa is

obtained for CrN on steel but $3.4 * 10^9$ Pa are relaxed for CrN in the CrN/Cr/steel system.

Table C.1: A list of samples characterized using XRD and WCT

Substrat	Si(100) or austenitic stainless steel		
Cr thickness (μm)	0	2	3
CrN thickness (μm)	3	1	0

C.1 Introduction

Hard coatings based on CrN or TiN are routinely used to protect bulk materials from abrasion and corrosion [1, 2]. The application of those coatings demands an optimization of deposition processes [3–5] in order to design coating/substrate systems with improved thermal and mechanical performance. The optimization resides primarily in the engineering of coating nano–structure, residual stress state, interface properties and thermo–mechanical behaviour [6–9].

Residual stresses play a decisive role in coating thermomechanical behaviour. In order to design coatings with improved thermal fatigue resistance, it is of great interest to assess temperature–induced changes in the residual stresses. A common way to look at the changes in the residual stress occurring during thermal cycling is to perform in–situ stress characterization using X–ray diffraction (XRD) and/or wafer curvature technique (WCT). The stress-temperature evolution usually indicates changes caused by defect annihilation, diffusion, changes in nano–structure and recrystallisation.

In the case of multilayered coatings based on the CrN system deposited on steel, temperature–dependent studies of stresses using XRD are relatively rare. The main reason is that those coatings usually exhibit residual stress gradients and gradients of texture with more than one texture component. Moreover, CrN shows relatively strong mechanical anisotropy and therefore the stress characterization using XRD is a complex task since exact X–ray elastic constants (XECs) are usually unknown.

The main aim of this work is to perform a temperature–dependent characterization of stresses in CrN/Cr multilayer systems using XRD and to compare stress values obtained using XRD and WCT at temperatures up to 550 °C. Moreover, the residual stresses of CrN/Cr systems deposited on Si(100) and austenite stainless steel are compared.

C.2 Experimental details

C.2.1 Deposition of the CrN/Cr coating systems

As substrate for specimen preparation, 300 μm thick one side polished Si(100) wafers without oxide or nitride layer, cleaned using isopropanol and acetone were used. Moreover, austenitic stainless steel sheets with a thickness of about 500 μm were mechanically and electrolytically polished. Both types of substrates were coated with CrN and Cr using magnetron sputtering with a Cr target in an Ar + N_2 atmosphere at 350 °C, 1 Pa with a partial pressure of 0.25 Pa for N_2 and 0.75 Pa for Ar, respectively. The

Table C.2: Room–temperature SECs of Cr [12] and CrN [13]. The anisotropy factor was calculated using the formula $A = 2C_{44}/(C_{11} - C_{12})$ and the room-temperature XECs using the software ElastiX [14].

Coating	C_{11} (10^{11} Pa)	C_{44} (10^{11} Pa)	C_{12} (10^{11} Pa)	A	$s_1^{RT,111}$ (10^{-11} Pa)	$\frac{1}{2}s_2^{RT,111}$ (10^{-11} Pa)
CrN	5.42	0.88	0.27	0.34	−0.0923	0.4446
Cr	3.50	1.01	0.68	0.72	−0.0854	0.4613

bias voltage was −80 V for CrN and −40 V for Cr. Tab. C.1 summarizes the samples investigated in this study. In bilayer systems CrN was always the top layer.

C.2.2 AFM characterization

The surface topography of the coatings was analysed before and after the thermal treatment using a DI Dimension 3100 Atomic Force Microscope (AFM). An area of 10*10 μm was imaged using contact mode.

C.2.3 X–ray diffraction characterization

The structural characterization of the coatings was performed using a four circle diffractometer. Parallel beam geometry with a polycapillary optics on the primary side and Soller slits, a graphite monochromator and a scintillation detector on the secondary side was used. The measurements were performed with Cu K_α radiation. Basic structural properties of the coatings before and after thermal cycling were determined using $\theta/2\theta$ scans in order to analyse possible changes in texture and microstructure. The scans were taken in the 2θ range 35-140 °C with a step size of 0.02 ° and counting time of 1 s.

Residual stresses in the coatings were characterized in the temperature range of 25-550 °C in N_2 atmosphere using the $\sin^2\psi$ method with $\Delta\sin^2\psi = 0.1$. The heating was performed at a constant heating rate of 18 °C/min using an Anton Paar heating chamber DHS 900 [10, 11]. The lattice spacing $d_\psi^{T,hkl}$ measured at the temperature T, reflection hkl and the sample tilt angle ψ was used to calculate the in–plane isotropic biaxial residual stress σ^T according to

$$d_\psi^{T,hkl} = d_0^{hkl}\left(1 + \sigma^T\left[2s_1^{T,hkl} + \frac{1}{2}s_2^{T,hkl}\sin^2\psi\right]\right) \tag{C.1}$$

where $s_1^{T,hkl}$ and $\frac{1}{2}s_2^{T,hkl}$ are the XECs of the individual coating materials. It was supposed that the stresses are in–plane isotropic, *i.e.* $\sigma^T = \sigma_{11}^T = \sigma_{22}^T$. XECs for CrN and Cr layers were calculated from the single–crystal elastic constants (SECs) assuming the Hill model and using the software ElastiX [14]. For simplicity, it was supposed that the coatings are mechanically isotropic. Temperature–dependent SECs of Cr are referenced in [12] but there are no temperature dependent data of SECs for CrN available. For this reason, room–temperature XECs of CrN were applied in the

whole temperature range. The room–temperature SECs of CrN and Cr are repeated in Tab. C.2. The stress values calculated according to Eq.(C.1) remain accurate within an error interval of ±5 % using standard deviation of $\sin^2\psi$ slopes in Gaussian error propagation formula of Eq.(C.1).

C.2.4 Wafer curvature technique

The macroscopic stress σ^T in the coatings deposited on Si (100) substrates was characterized using WCT. The coatings were thermally cycled between 25 and 550 °C in vacuum (pressure $\leq 10^{-3}$ Pa) at a heating/cooling rate of 5 °C/min. The radius R of the bending of the Si(100) substrate was determined as a function of temperature by an optical method based on two parallel laser beams. The macroscopic stress σ was then calculated by the modified Stoney's formula [15]:

$$\sigma = \frac{E}{6\,(1-\nu)}\frac{h_\mathrm{s}^2}{h_\mathrm{f}}\frac{1}{R} \tag{C.2}$$

Here, $E/(1-\nu) = 181 * 10^9$ Pa [15] is the biaxial Young's modulus of the Si(100) substrate. h_f and h_s are the thicknesses of the film and substrate, respectively. The film and substrate thickness of the single layer were determined by analysing cross–sections of scanning electron microscopy images. The stress values calculated according to Eq.(C.2) remain within an error interval of ±5 % using standard deviation of rocking curve slopes in Gaussian error propagation formula of Eq.(C.2).

C.3 Results and discussion

C.3.1 Surface topography

The surface topography of the coatings was analysed before and after the thermal treatment using Atomic Force Microscopy. The AFM images of the CrN, CrN/Cr and Cr coating on steel recorded before and after annealing at 550 °C are compared in Fig. C.1. For CrN, the surface morphology remains unchanged by annealing. This holds also true for the CrN top layer in Cr/CrN coatings. The Cr coating exhibits a small reduction in averaged surface roughness from 5.13 nm to 4.34 nm and a reduction in root mean square roughness from 6.46 nm to 5.71 nm (Fig. C.1). The reduction in root mean square roughness of Cr indicates that surface inclusions or hillocks can be neglected at those temperatures as mechanisms for stress relaxation.

C.3.2 Residual stresses in the coatings

On the basis of XRD $\theta/2\theta$ scans, CrN (111) and Cr (111) reflections were selected in order to determine the elastic strain in the coatings using the $\sin^2\psi$ method. In Fig. C.2 representative $\sin^2\psi$ data of 3 μm thick CrN coatings are presented. Since both coatings exhibit a nearly linear behaviour of the lattice parameter a as function of $\sin^2\psi$, the stresses were calculated using the isotropic XECs listed in Tab. C.2.

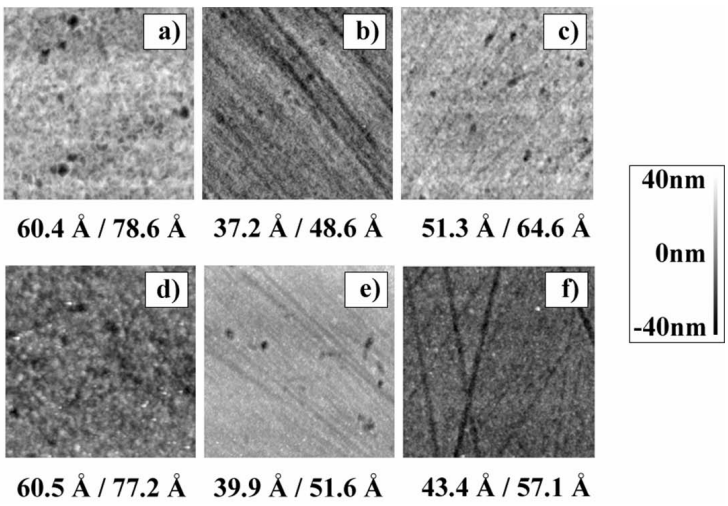

Figure C.1: AFM images of CrN, CrN/Cr and Cr on steel before and after annealing. Cr shows a smaller surface roughness after annealing whereas CrN roughness is the same before and after annealing. The first number is the averaged roughness and the second number is the root mean square roughness. a) 3 μm CrN on steel before annealing, b) 3 μm Cr on steel before annealing, c) 1 μm CrN on 2 μm CrN/steel before annealing, d) 3 μm CrN on steel after annealing, e) 3 μm Cr on steel after annealing, f) 1 μm CrN on 2 μm CrN/steel after annealing.

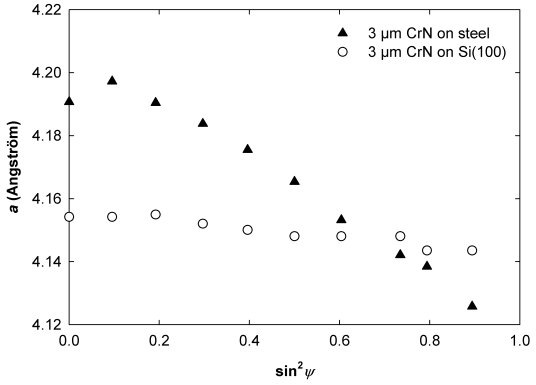

Figure C.2: $\sin^2\psi$ plots of CrN on Si(100) and steel substrate to check stress state. It would be much harder to deal with non–linearities as with linear behaviour. This plot shows the linear behaviour of both CrN coatings except at low polar angles ψ.

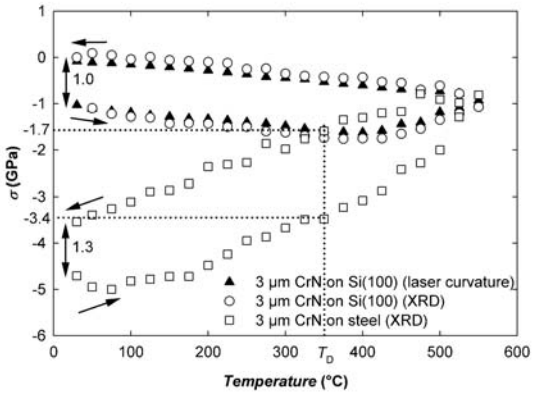

Figure C.3: Stress in 3 μm CrN on Si(100) measured with X–rays and waver curvature method and 3 μm CrN on steel measured with X–rays. T_D is the deposition temperature of 350 °C. The intrinsic stresses in CrN on Si and steel are $-1.7 * 10^9$ Pa and $-3.4 * 10^9$ Pa, respectively.

Each coating/substrate system was characterized two times to demonstrate reproducibility. For each thermocycle virginal samples were used. The results of absolute stresses were equal within a tolerance of 5 %. A third series of samples was thermally cycled two times to prove thermo–elastic behaviour in the same temperature range of 25-550 °C in the second run.

Residual stresses as a function of temperature in 3 μm thick CrN coatings deposited on Si(100) and steel are presented in Fig. C.3. Stress values for CrN on Si(100) from using XRD and WCT document that both experimental techniques provide comparable data. This justifies the use of isotropic XECs Tab. C.2 in the case of CrN when evaluating stresses from XRD data.

Upon heating, the compressive stresses in CrN on Si(100) linearly increase following the thermo–elastic line. The thermal stress in CrN originates from the specific mismatch of coefficients of thermal expansion (CTEs) between the Si substrate and the CrN layer Tab. C.3. The total stress can be written as

$$\sigma^{\mathrm{T}} = \sigma^{\mathrm{i}} + \sigma^{\mathrm{th}} \tag{C.3}$$

where σ^{T}, σ^{i} and σ^{th} are the total, intrinsic and thermal stress, respectively.

Heating to the deposition temperature of 350 °C, a stress of $-1.7 * 10^9$ Pa is obtained for CrN on Si(100)(Fig. C.3). It is believed that this value corresponds to the intrinsic stress generated by the non–equilibrium growth conditions. Above $\approx$ 400 °C, the annealing of defects results in a noticeable decrease of the stresses. The stress development during cooling to room temperature is linear and follows the thermo–elastic slope given by the mismatch of CTEs and the biaxial modulus of the coating.

In the case of CrN deposited on steel (Fig. C.3), the stresses were characterized using XRD only. Since the CTE of steel is larger than that of CrN, heating results in a decrease of the compressive stress level in CrN. Above $\approx$ 450 °C, a slight relaxation of

Table C.3: Thermal expansion coefficients for CrN [16], Cr [17], Si(100) and steel [15]

CrN	Cr	Si(100)	Steel
(10^{-6} K^{-1})	(10^{-6} K^{-1})	(10^{-6} K^{-1})	(10^{-6} K^{-1})
6	8	3	11

the stresses in the coating caused by the annihilation of point defects takes place. The stress dependence during cooling is linear and corresponds to the mismatch of CTEs. Interestingly, the intrinsic stress σ^{i} in CrN on steel of about $-3.4 * 10^9$ Pa is larger as for CrN on Si(100). An explanation could be a fact that the atoms peening the growing coating on steel possess a higher energy since the conductive substrate causes an increase of the electric field in the deposition chamber. Furthermore, the different adatom mobility in the early film growth stage, interdiffusion and the reactions with the substrate may change the stress value. A comparison of the stress relaxation $\Delta\sigma$, which is the difference in stress before and after annealing at room temperature (RT), in CrN coatings on Si (100) and steel shows that the stress relaxation in CrN on steel with more than $1.3 * 10^9$ Pa is larger than in CrN on Si(100) with $1 * 10^9$ Pa. This indicates that the CrN coatings on steel possess a higher concentration of defects.

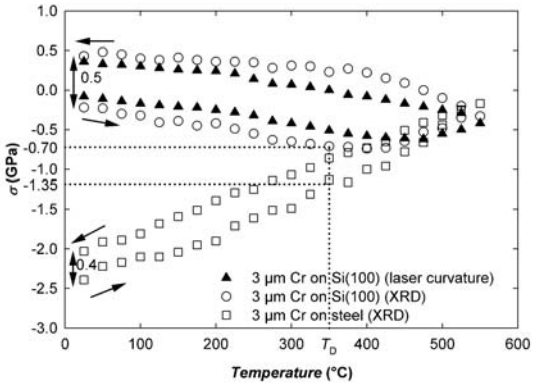

Figure C.4: Stress in 3 μm Cr on Si(100) measured with X–rays and wafer curvature method and 3 μm Cr on steel measured with X–rays. T_{D} is the deposition temperature of 350 °C. The intrinsic stresses in Cr on Si and steel are $-0.70 * 10^9$ Pa and $-1.35 * 10^9$ Pa, respectively.

In Fig. C.4, results from 3 μm thick Cr coatings on Si(100) and steel are presented. The 3 μm thick Cr layer on Si(100) exhibits a slight relaxation of stresses when annealed above a deposition temperature of 350 °C. The cooling branch is nearly linear and parallel to the heating one in the thermo–elastic region. The linear increase/decrease of the branches can be again explained by the specific mismatch of CTEs. The intrinsic stress σ^{i} in Cr deposited on Si(100) ($-0.7 * 10^9$ Pa) is approximately half of that in Cr on steel ($-1.35 * 10^9$ Pa), similarly as in the case of CrN coatings (Fig. C.3).

In Fig. C.5, temperature–dependent stress changes in sublayers of CrN/Cr coating systems deposited on Si(100) and steel are presented. The aim was to understand how

the Cr layer influences the stress in CrN during annealing. It is evident that in both types of coating systems, the stresses in the as–deposited Cr layers are approximately equal to the stresses in the corresponding Cr coatings (Fig. C.4). The thermal annealing of the coating systems causes no stress-temperature hysteresis in Cr and at room–temperature stress values are obtained as prior to heating. This indicates that the CrN top layer prevents the relaxation of the stresses above deposition temperature. This can be explained by a suppression of diffusion–driven processes at the Cr surface by the CrN top layers. In other words, the presence of the CrN top layer forces the Cr layer into a thermoelastic response.

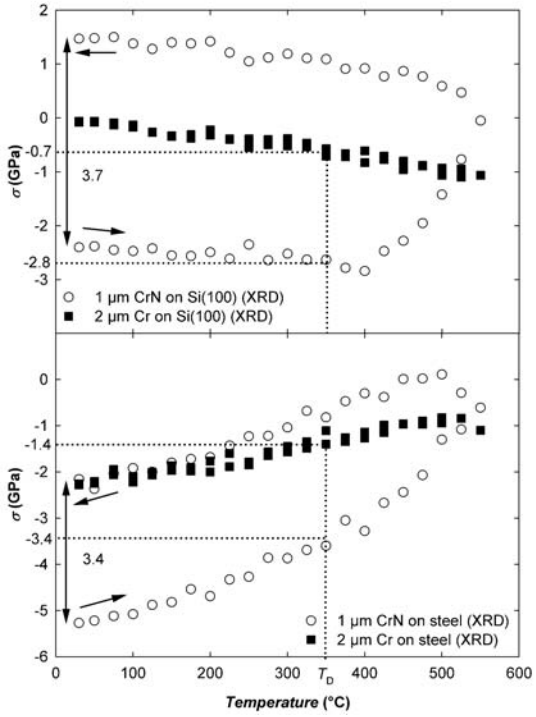

Figure C.5: Stress of a 1 μm CrN and 2 μm Cr double layer on Si(100) and steel substrate measured with X–rays. CrN is top layer, Cr interface layer is between CrN and substrate. T_D is the deposition temperature of 350 °C. The intrinsic stresses in CrN and Cr on Si are $-2.8 * 10^9$ Pa and $-0.7 * 10^9$ Pa. The intrinsic stresses in CrN and Cr on steel are $-3.4 * 10^9$ Pa and $-1.4 * 10^9$ Pa.

The temperature–dependencies of stresses in the CrN top layer of the CrN/Cr coating systems on Si(100) and steel (Fig. C.5) show that the presence of Cr sublayers increase the stress levels in the as–deposited CrN. There are two possible explanations for this effect namely (i) the density of point defects in CrN growing on Cr is significantly large and/or (ii) there is a strong gradient of point defect density in CrN as recently reported for TiN coatings [18]. The intrinsic stress in CrN on Cr/Si(100) is $-2.8 * 10^9$ Pa and $-3.4 * 10^9$ Pa in CrN on Cr/steel. This result documents that the

Cr sublayer on Si(100) causes a significant increase of the intrinsic stresses in comparison with CrN on Si(100) deposited without Cr (Fig. C.3). The annealing of CrN/Cr coating systems above deposition temperature results in a strong stress relaxation in CrN. Remarkably, a comparison of the stress-temperature results in CrN sublayers on Cr shows that the stress relaxation after cooling down is comparable (about $-3.7 * 10^9$ Pa in CrN on Cr/Si(100) and $-3.4 * 10^9$ Pa in CrN on Cr/steel) which documents an important role of the Cr sublayer in the formation of point defects. On Si(100) and steel substrates the relaxation in CrN was significantly smaller (Fig. C.3). No sample exhibited any kind of delamination or flaking after any thermocycle.

C.4 Conclusions

A comparison of the experimental data obtained using XRD and WCT technique indicates that both techniques provide comparable data which differ only within the experimental errors and are therefore complementary (Figs. C.3, C.4). The main advantage of XRD is the possibility to obtain the stresses of different phases in multilayered systems as a function of the temperature. This was demonstrated for a multilayered hard coating on steel to temperatures up to 550 °C. The results indicate significant differences in stresses in CrN/Cr deposited on Si(100) and steel and allow to analyse phenomena like intrinsic and extrinsic stresses and the influence of substrate material.

The difference in stress relaxation at room temperature for CrN on steel and CrN on Si originates from the different concentration of defects in CrN. It is believed that the conductivity of the steel substrate increases the impact of the impinging atoms in sputter process and therefore generates higher point density than in nonconductive Si substrates. It was shown that no Cr hysteresis in thermocycle can be observed in CrN/Cr/steel and CrN/Cr/Si systems, *i.e.* CrN influences the thermo–mechanical behaviour of Cr significantly in comparison to single Cr/steel or Cr/Si systems. The presence of Cr in the CrN top layer of the CrN/Cr coating systems on Si(100) and steel increase the stress levels in the as deposited CrN. Two explanations are (i) the density of point defects in CrN growing on Cr is significantly large and/or (ii) there is a strong gradient of point defect density in. In the future, it will be necessary to understand not only the temperature–dependencies of volume–averaged stresses in the coatings but also the depth gradients as a function of temperature.

C.5 Acknowledgment

This work was supported by the Austrian NANO Initiative via a grant from the Austrian Science Fund FWF within the project “StressDesign –Development of Fundamentals for Residual Stress Design in Coated Surfaces.”

C.6 References

[1] Jagielski, J., Khanna, A. S., Kucinski, J., Mishra, D. S., Racolta, P., Sioshansi, P., Tobin, E., Thereska, J., Uglov, V., Vilaithong, T., Viviente, J., Yang, S. Z., and Zalar, A. *Appl. Surf. Sci* **156**(1-4), 47–64 (2000).

[2] Rocha, L. A., Ariza, E., Ferreira, J., Vaz, E., Ribeiro, E., Rebouta, L., Alves, E., Ramos, A. R., Goudeau, P., and Riviere, J. P. *Surf. Coat. Technol.* **180-81**, 158–163 (2004).

[3] Han, Z. H., Tian, J. W., Lai, Q. X., Yu, X. J., and Li, G. Y. *Surf. Coat. Technol.* **162**(2-3), 189–193 (2003).

[4] Pradhan, S. K., Nouveau, C., Vasin, A., and Djouadi, M. A. *Surf. Coat. Technol.* **200**(1-4), 141–145 (2005).

[5] Mendibide, C., Steyer, P., Esnouf, C., Goudeau, P., Thiaudiere, D., Gailhanou, M., and Fontaine, J. *Surf. Coat. Technol.* **200**(1-4), 165–169 (2005).

[6] Zhao, Z. B., Rek, Z. U., Yalisove, S. M., and Bilello, J. C. *Thin Solid Films* **472**(1-2), 96–104 (2005).

[7] Kim, D., Heiland, B., Nix, W. D., Arzt, E., Deal, M. D., and Plummer, J. D. *Thin Solid Films* **371**(1-2), 278–282 (2000).

[8] Cunha, L., Andritschky, M., Pischow, K., and Wang, Z. *Thin Solid Films* **356**, 465–471 (1999).

[9] Evans, A. G. and Hutchinson, J. W. *Acta metall. mater.* **43**(7), 2507–2530 (1995).

[10] Resel, R., Tamas, E., Sonderegger, B., Hofbauer, P., and Keckes, J. *J. Appl. Cryst.* **36**, 80–85 (2003).

[11] Keckes, J. *J. Appl. Cryst.* **38**, 311–318 (2005).

[12] Landolt, H. and Brnstein, R. *Numerical Data and Functional Relationships in Science and Technology*, volume 2 of *Group III: Crystal and Solid State Physics*. Springer, Berlin Heidelberg New-York, (1969).

[13] Birkholz, M. *Thin Film Analysis by X-Ray Scattering*. WILEY-VCH, (2006).

[14] Wern, H., Koch, N., and Maas, T. *Mater. Sci. Forum* **404**, 127–132 (2002).

[15] Suresh, S. and Freund, L. B. *Thin Film Materials Stress, Defect Formation and Surface Evolution*. Cambridge University Press, Cambridge, (2003).

[16] Gall, D., Shin, C. S., Spila, T., Oden, M., Senna, M. J. H., Greene, J. E., and Petrov, I. *J. Appl. Phys.* **91**(6), 3589–3597 (2002).

[17] Holzwarth, U. and Stamm, H. *J. Nucl. Mater.* **300**(2-3), 161–177 (2002).

[18] Köstenbauer, H., Fontalvo, G. A., Kapp, M., Keckes, J., and Mitterer, C. *Surf. Coat. Technol.* **201**(8), 4777–4780 (2007).

D

Elastic constants of fiber-textured thin films determined by X-ray diffraction. I. Theoretical concept

K.J. Martinschitz[a] and J. Keckes[a]

[a]Department of Materials Physics, University of Leoben and Erich Schmid Institute for Materials Science, Austrian Academy of Sciences, Jahnstrasse 12, A-8700 Leoben, Austria

Abstract A new methodology is presented that allows a rapid determination of elastic constants of polycrystalline thin films by X-ray diffraction under static conditions. In the present paper, a theoretical concept is developed and tested on calculated examples of Cu and CrN films. The mechanical elastic constants are extrapolated from X-ray elastic constants considering crystal and macroscopic elastic anisotropy. The derived algorithm enables to find a reflection and the corresponding value of the X-ray anisotropic factor Γ for which the X-ray elastic constants correspond to their mechanical counterparts in the case of fiber textured cubic polycrystalline aggregates. The approach is independent of the crystal elastic anisotropy and depends on the fiber texture type, texture sharpness and the amount of randomly oriented crystallites in the film. In the next paper of this series, an experimental application of the approach based on the simultaneous use of $\sin^2\psi$ and X-ray diffraction substrate curvature techniques is demonstrated.

D.1 Synopsis

Supposing the Hill grain interaction model, it is demonstrated that X-ray elastic constants can be used to determine mechanical elastic constants of cubic fiber textured thin films. The algorithm to determine the mechanical elastic constants strongly depends on the fiber texture type, texture sharpness and the amount of randomly oriented crystallites in the polycrystalline aggregate.

D.2 Introduction

X-ray elastic constants and diffraction stress factors are usually used to calculate residual stresses from experimental X-ray elastic strains [1, 2]. In the case of specimen with crystal elastic anisotropy, X ray elastic constants differ for various *hkl* reflections and are moreover dependent on the macroscopic elastic anisotropy (texture), grain-interaction mechanism and single-crystal elastic constants [3–6].
Recently, a new rapid experimental approach based on a simultaneous application of $\sin^2\psi$ and X-ray diffraction substrate curvature techniques was proposed [7–10]. The new approach provides an opportunity to quantify experimental X-ray elastic strains and macroscopic stresses in thin films using a static diffraction experiment. The stresses applied on the film are determined from the geometrical changes of the elastically deformed substrate which is attached to the film [11, 12]. The experimental *stress* and *strain* can then be used to evaluate experimental X-ray elastic constants, stress factors and grain-interaction phenomena [7, 8, 10].
Mechanical elastic constants can be extrapolated from X-ray elastic constants considering crystal and macroscopic elastic anisotropy. In the case of cubic polycrystalline aggregates with macroscopic elastic isotropy (quasi-isotropic materials) which obey the Hill grain interaction model, it was demonstrated that X-ray elastic constants correspond to their mechanical counterparts for $\Gamma_{hkl} = 0.2$ whereby Γ_{hkl} is the X-ray anisotropic factor according to the Reuss grain-interaction model with

$$\Gamma_{hkl} = \frac{h^2k^2 + k^2l^2 + l^2h^2}{(h^2 + k^2 + l^2)^2} \tag{D.1}$$

where (hkl) are Miller indices of a crystallographic plane [13]. According to the Reuss model, X ray elastic anisotropy is often expressed as a function of $3\Gamma_{hkl}$ and this formalism will be applied hereafter [14].
It is the aim of this paper to analyze under which conditions the knowledge of X-ray elastic constants can be used to determine or estimate mechanical elastic constants of cubic fiber textured thin films. At first, selected mechanical elastic constants of Cu and CrN will be calculated using the Hill model that represents a reasonable simplification of the problem [15–17]. As a next step, the mechanical values will be compared with the X-ray elastic constants. As a result a certain type of $3\Gamma_{hkl}$ dependent selection rule will be derived whereby *hkl* in $3\Gamma_{hkl}$ denotes a reflection for which mechanical and X-ray elastic constants are equal. In the next paper of this series, the approach will

be demonstrated on experimental characterization of fiber textured thin films [18]. It should be noted that the methodology derived in this paper can be generally applied to any equibiaxially loaded or stressed polycrystalline aggregate with the fiber texture oriented perpendicular to the stress direction.

D.3 Mechanical elastic constants of thin films

D.3.1 Hill grain interaction model

Elastic behavior of a thin film deposited on a solid substrate (Fig. D.1) can be represented by the Hook's law:

$$\left\{\epsilon_{ij}^{S}\right\}^{\mathrm{M}} = \left\{S_{ijkl}^{S}\right\}^{\mathrm{M}} \left\{\sigma_{kl}^{S}\right\} \tag{D.2}$$

where $\left\{\epsilon_{ij}^{S}\right\}^{\mathrm{M}}$ is the mechanical (M) elastic strain, $\left\{S_{ijkl}^{S}\right\}^{\mathrm{M}}$ expresses the mechanical elastic constants of the film and $\left\{\sigma_{kl}^{S}\right\}$ represents the residual stress [19, 20]. The stress, strain and compliance tensors in Eq. D.2 are expressed in the sample coordinate system (S) (Fig. D.1). In general, $\left\{S_{ijkl}^{S}\right\}^{\mathrm{M}}$ of a polycrystalline film depends on texture, single crystal elastic constants and grain interaction mechanism [4]. For practical cases, the Hill grain-interaction model can be used to evaluate $\left\{S_{ijkl}^{S}\right\}^{\mathrm{M}}$ of the film [15] using an arithmetic mean of the compliance tensors $\left\{S_{ijkl}^{S}\right\}^{\mathrm{R}}$ and $\left\{S_{ijkl}^{S}\right\}^{\mathrm{V}}$ obtained from the Reuss and Voigt grain-interaction models:

$$\left\{S_{ijkl}^{S}\right\}^{\mathrm{M}} = \frac{1}{2}(\left\{S_{ijkl}^{S}\right\}^{\mathrm{R}} + \left\{S_{ijkl}^{S}\right\}^{\mathrm{V}}) \tag{D.3}$$

Elastic constants according to the Reuss average $\left\{S_{ijkl}^{S}\right\}^{\mathrm{R}}$ can be calculated as follows

$$\left\{S_{ijkl}^{S}\right\}^{\mathrm{R}} = \int S_{ijkl}^{S}(g) f(g)\, dg \tag{D.4}$$

In the case of Voigt average, $\left\{S_{ijkl}^{S}\right\}^{\mathrm{V}}$ can be determined according

$$\left\{S_{ijkl}^{S}\right\}^{\mathrm{V}} = [\int C_{ijkl}^{S}(g) f(g)\, dg]^{-1} \tag{D.5}$$

whereby $f(g)$ represents the orientation distribution function (ODF) of the crystallites in the film [17, 21]. S_{ijkl}^{S} and C_{ijkl}^{S} in Eqs. D.4,D.5 are single crystal elastic constants expressed in S whereas $f(g)$ indicates the volume fraction of the crystallites with the orientation g. The integration in Eqs. D.4,D.5 is carried out over the whole ODF space [4].

The tensor $\left\{S_{ijkl}^{S}\right\}^{\mathrm{M}}$ (Eq. D.2) represents the elastic behavior of the material in the sample coordinate system S (Fig. D.1) [19] and can be expressed in the L system using

$$\left\{S^L_{ijkl}\right\}^{\mathrm{M}}_{\phi,\psi} = a_{im}a_{jn}a_{ko}a_{lp}\left\{S^S_{mnop}\right\}^{\mathrm{M}} \tag{D.6}$$

where a_{ij} represents a direction cosines between L and S systems (Fig. D.1) [2].

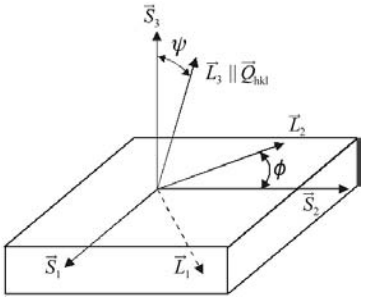

Figure D.1: A definition of two coordinate systems used for the characterization of in-plane elastic strains using $\sin^2\psi$ method: sample system S, laboratory system L [2]. The X-ray elastic strain along the direction $\vec{L}_3$ (which is parallel to the diffraction vector $\vec{Q}_{hkl}$) is characterized by measuring the reflection *hkl*. The orientation of the vector $\vec{Q}_{hkl}$ with respect to $\vec{S}_i$ is defined by the angles ϕ and ψ. The direction cosines a_{ij} (Eq. D.6) represent a transformation from S to L coordinate systems.

In practical cases, Young's modulus E is usually used to express elastic behavior of materials. The E magnitude in the direction $\vec{L}_3$ can be obtained from $\left\{S^L_{ijkl}\right\}^{\mathrm{M}}_{\phi,\psi}$ tensor:

$$\frac{1}{\{E\}^{\mathrm{M}}_{\phi,\psi}} = \left\{S^L_{3333}\right\}^{\mathrm{M}}_{\phi,\psi}. \tag{D.7}$$

The *out-of-plane* Young's modulus $\{E\}^{\mathrm{M}}_{\phi,\psi=0}$ can be obtained from Eq. D.7 using $\left\{S^L_{3333}\right\}^{\mathrm{M}}_{\phi,\psi=0}$.

D.4 Calculation of mechanical elastic constants

Using the procedure from the previous section, Young's moduli of Cu and CrN thin films with various fiber textures were calculated numerically applying single crystal elastic constants from Tab. D.1 and various types of ODFs.

In Fig. D.2, an exemplary 111 pole figure, a distribution of the intensity across the pole figure and a corresponding ODF demonstrate a strong 111 fiber texture with 10% fraction of randomly oriented crystallites.

As a parameter for the ODF calculation, the full width at half maximum in the centre of pole figure (as usually experimentally measured using a ψ scan [17]) and hereafter denoted as ψ_{FWHM} was used (Fig. D.2). Since the aim is to develop a simple laboratory method to determine elastic constants of thin films, ψ_{FWHM} was used as a measure of the texture sharpness [instead of using variables expressed in terms of ϕ_1, Φ and ϕ_2 angles (Fig. D.2) which are usually needed to define ODF properties according to the

Table D.1: Single crystal elastic constants of Cu and CrN at room temperature and the Zener's anisotropy ratio [22] (ZAR) defined by Eq. D.8 [20, 23].

Material	S_{1111}	S_{1122}	S_{1212}	ZAR
	in GPa^{-1} 10^{-3}			
Cu	15.00	-6.28	3.32	3.21
CrN	1.860	-0.09	2.84	0.34

Bunge's notation [17]]. Numerous ODFs with ψ_{FWHM} in the range 0-180 with the step of 5 degrees were generated in order to calculate $\left\{S^S_{ijkl}\right\}^{\mathrm{M}}$ (Eq. D.2) and subsequently *out-of-plane* Young's modulus $\{E\}^{\mathrm{M}}_{\phi,\psi=0}$ (Eq. D.7). This calculation was performed for various *uvw* fiber textures whereas *uvw* represents indices of (*uvw*) crystallographic planes oriented preferably parallel to the sample surface. Additionally, it was supposed that the films possess also crystallites with a random orientation (further denoted as ISO) in the range of 0-100 %. In practical cases, the ISO can be determined (i) accurately using ODF analysis of the experimental pole figure data or (ii) estimated by analyzing the background in the *uvw* pole figure data.

As an example of the procedure, calculated *out-of-plane* Young's moduli $\left\{E^{111}\right\}^{\mathrm{M}}_{\phi=0,\psi=0}$ and $\left\{E^{100}\right\}^{\mathrm{M}}_{\phi=0,\psi=0}$ of Cu and CrN thin films with 111 and 100 fiber textures are presented in Figs. D.3 and D.4. As a parameter for the calculation, the texture sharpness ψ_{FWHM} and the amount of the randomly oriented crystallites ISO were applied. The three dimensional plots document that the moduli of the film exhibit relatively strong maxima or minima for small ψ_{FWHM} and ISO but converge to the moduli of isotropic Cu and CrN when one of the parameters increases.

Cu and CrN possess different types of crystal elastic anisotropy (Tab. D.1) with the Zener's anisotropy ratio ZAR [22] defined as

$$ZAR = \frac{8(S_{1111} - S_{1122})}{S_{1212}} \tag{D.8}$$

The ZAR>1 indicates that in Cu the $\langle hhh\rangle$ the direction is harder than the $\langle 00l\rangle$ one. Therefore the modulus $\left\{E^{111}\right\}^{\mathrm{M}}_{\phi=0,\psi=0}$ of a Cu film with a strong 111 fiber texture is significantly larger than the modulus $\left\{E^{100}\right\}^{\mathrm{M}}_{\phi=0,\psi=0}$ of a Cu film with a strong 100 fiber texture (Fig. D.3). In the case of CrN, an opposite situation must be considered (Fig. D.4). The three-dimensional dependencies similar to those in Figs. D.3,D.4 were generated for various types of *uvw* fiber textures.

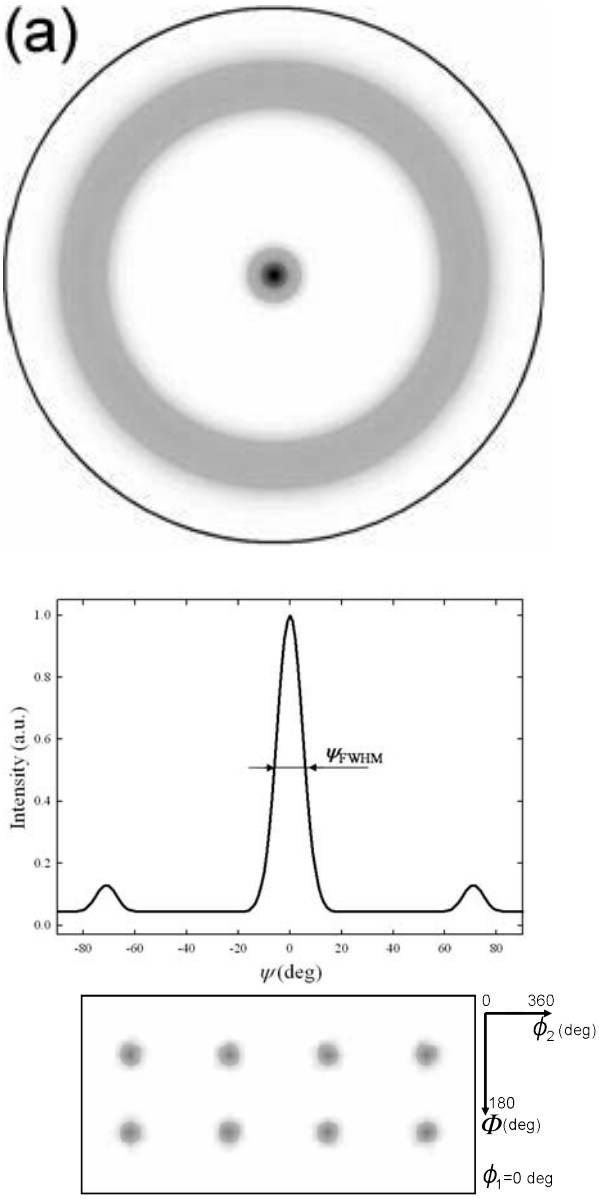

Figure D.2: A calculated 111 pole figure of a cubic thin film with a strong 111 fiber texture and 10% fraction of randomly oriented crystallites (a). In (b), a distribution of the intensity across the pole figure whereas the variable $\psi_{\mathrm{FWHM}} = 10$ degrees represents the sharpness of the texture. A representative $\phi_1 = 0$ degrees section of the ODF (c) which is identical for all ϕ_1 values documents a 111 fiber character of the texture [17].

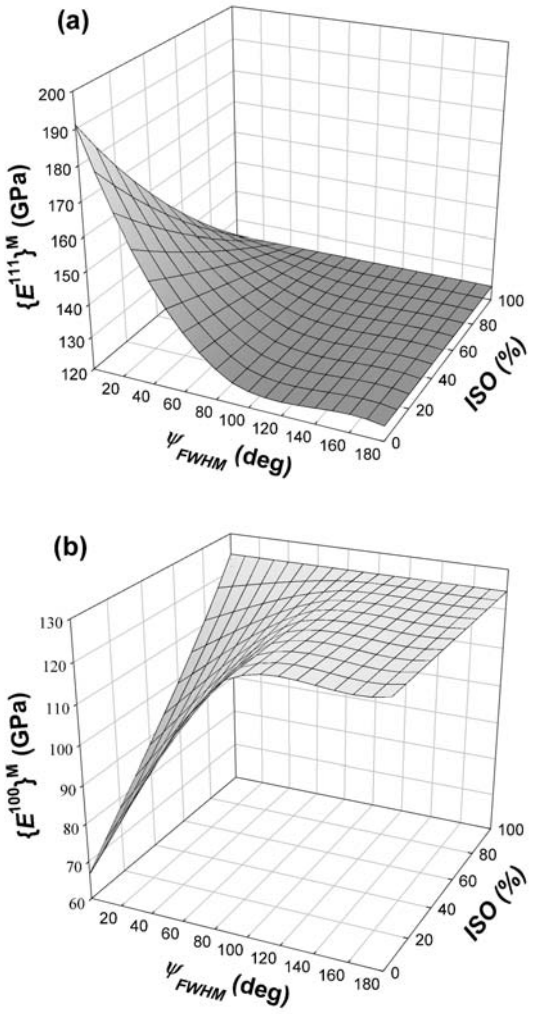

Figure D.3: Calculated *out-of-plane* Young's moduli of 111 (a) and 100 (b) fiber textured Cu thin films as a function the texture sharpness ψ_{FWHM} (Fig. D.2) and ISO.

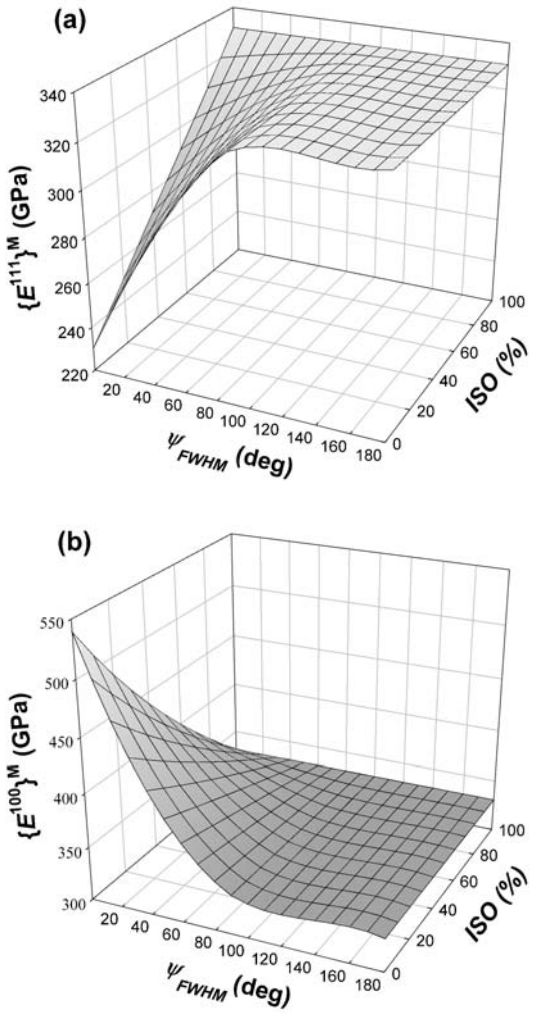

Figure D.4: Calculated *out-of-plane* Young's moduli E of 111 (a) and 100 (b) fiber textured CrN thin films as a function the texture sharpness ψ_{FWHM} (Fig. D.2) and ISO.

The results in Figs. D.3,D.4 represent *out-of-plane* Young's moduli calculated from the tensor $\left\{S^S_{ijkl}\right\}^{\mathrm{M}}$. In the case of fiber-textured thin films, however, the elastic behavior is in-plane isotropic (*i.e.* independent on the angle ϕ) but dependent on the tilt angle ψ (Fig. D.1) In order to demonstrate this situation, Young's moduli of CrN and Cu fiber-textured thin films (Fig. D.2) were calculated as a function of angles ϕ and ψ (Fig. D.5) using Eqs. D.3-D.7 and are presented in polar coordinates in Fig. D.5. The differences in crystal elastic anisotropy causes that CrN modulus possess a minimum at $\psi = 0$ degrees in contrast to the Cu dependence which exhibits a maximum in the centre of the polar plot (Fig. D.5).

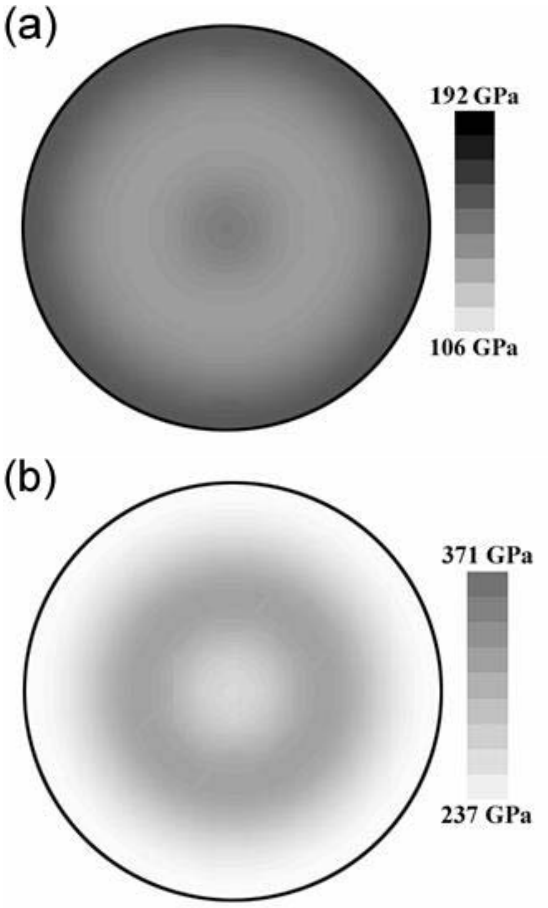

Figure D.5: Calculated Young's moduli of Cu (a) and CrN (b) expressed in polar coordinates ϕ and ψ (Fig. D.1). The moduli were calculated using the ODF from Fig. D.2.

D.5 X-ray elastic constants of thin films

D.5.1 X-ray elastic moduli

X-ray diffraction Hook's law relates X-ray elastic strain $\left\{\epsilon_{33}^{L}\right\}_{\phi,\psi}^{hkl}$ measured in the direction $\vec{L}_3$ by scanning the reflection *hkl*, X ray elastic compliances $\left\{S_{33ij}^{L}\right\}_{\phi,\psi}^{hkl}$ and the macroscopic stress $\left\{\sigma_{ij}^{L}\right\}$ expressed in L coordinate system (Fig. D.1) as follows

$$\left\{\epsilon_{33}^{L}\right\}_{\phi,\psi}^{hkl} = \left\{S_{33ij}^{L}\right\}_{\phi,\psi}^{hkl} \left\{\sigma_{ij}^{L}\right\} \tag{D.9}$$

whereas $\left\{S_{33ij}^{L}\right\}_{\phi,\psi}^{hkl}$ depend generally on texture, grain-interaction mechanism, reflection *hkl*, single crystal elastic constants and on ϕ and ψ angles [1, 4]. $\left\{S_{33ij}^{L}\right\}_{\phi,\psi}^{hkl}$ can be calculated according to the Hill grain-interaction model as follows [4, 24]

$$\left\{S_{33ij}^{L}\right\}_{\phi,\psi}^{hkl} = \frac{1}{2}(\left\{S_{33ij}^{L}\right\}_{\phi,\psi}^{\mathrm{R},hkl} + \left\{S_{33ij}^{L}\right\}_{\phi,\psi}^{\mathrm{V}}) \tag{D.10}$$

X ray elastic compliances $\left\{S_{33ij}^{L}\right\}_{\phi,\psi}^{\mathrm{V}}$ represent an elastic behavior of the film according to the Voigt grain-interaction model (V) and can be calculated as

$$\left\{S_{33ij}^{L}\right\}_{\phi,\psi}^{\mathrm{V}} = a_{3k}a_{3l}a_{im}a_{jn}\left\{S_{klmn}^{S}\right\}^{\mathrm{V}} \tag{D.11}$$

where $\left\{S_{ijkl}^{S}\right\}^{\mathrm{V}}$ tensor was obtained using Eq. D.5 [4].
X ray elastic compliances according to the Reuss grain interaction model (R) can be obtained by the integration over the crystal orientations g for which the diffraction vector $\vec{Q}_{hkl}$ is parallel to the direction $\vec{L}_3$ [4]:

$$\left\{S_{33ij}^{L}\right\}_{\phi,\psi}^{\mathrm{R},hkl} = \int \left\{S_{33ij}^{L}\right\}[g(\vec{Q}_{hkl}\|\vec{L}_3)]f[g(\vec{Q}_{hkl}\|\vec{L}_3)]dg \tag{D.12}$$

Considering fiber-textured cubic thin films with the fiber axis oriented perpendicular to the sample surface, it will be in the next supposed that:

(i) the mechanical state of the films is biaxial and in-plane isotropic with $\sigma_{11}^{S} = \sigma_{22}^{S} = \sigma^{S}$ and $\epsilon_{11}^{S} = \epsilon_{22}^{S} = \epsilon^{S}$. Moreover, shear stresses σ_{12}^{S} and σ_{21}^{S} , shear strains ϵ_{12}^{S}, ϵ_{13}^{S} and ϵ_{23}^{S} as well as out of plane stresses σ_{i3}^{S} can be neglected on the macroscopic scale.

(ii) the thin films are in-plane elastic isotropic and not only the distribution of crystallites but also grain-interaction mechanism possess a rotational symmetry. The elastic properties of the films are therefore not dependent on the azimuth angle ϕ with $\left\{S_{ijkl}^{L}\right\}_{\phi,\psi}^{\mathrm{M}} = \left\{S_{ijkl}^{L}\right\}_{\psi}^{\mathrm{M}}$.

The above implicates that the Eqs. D.9 can be expressed as follows [25]

$$\left\{\epsilon_{33}^{L}\right\}_{\psi}^{hkl} = \sigma^{S}\lfloor(\left\{S_{3311}^{L}\right\}_{\psi}^{hkl} + \left\{S_{3322}^{L}\right\}_{\psi}^{hkl}) + (\left\{S_{3333}^{L}\right\}_{\psi}^{hkl} - \left\{S_{3311}^{L}\right\}_{\psi}^{hkl})\sin^2 + \left\{S_{3313}^{L}\right\}_{\psi}^{hkl}\sin 2\psi\rfloor \tag{D.13}$$

In the case of experimental dependence of $\left\{\epsilon_{33}^{L}\right\}_{\psi}^{hkl}$ on $\sin^2\psi$, the term $\left\{S_{3311}^{L}\right\}_{\psi}^{hkl} + \left\{S_{3322}^{L}\right\}$ corresponds to the intercept on the $\left\{\epsilon_{33}^{L}\right\}_{\psi}^{hkl}$ axis and the term $\left\{S_{3333}^{L}\right\}_{\psi}^{hkl} - \left\{S_{3311}^{L}\right\}_{\psi}^{hkl}$ is responsible for the curvature in $\sin^2\psi$ plots. Especially in the case of approximately linear $\left\{\epsilon_{33}^{L}\right\}_{\psi}^{hkl} - \sin^2\psi$ dependencies, the term $\left\{S_{3313}^{L}\right\}_{\psi}^{hkl}\sin 2\psi$ (proposed by [25]) is usually neglected [4].

Since the tensor components $\left\{S_{33ij}^{L}\right\}_{\psi}^{hkl}$ change as a function of the orientation of the diffraction vector $\vec{Q}_{hkl}$, their knowledge can be used to determine diffraction elastic constants as a function of (hkl) and ψ. For example, the diffraction modulus $\{E\}_{\psi}^{hkl}$ along the direction $\vec{L}_3$ reads

$$\frac{1}{\{E\}_{\psi}^{hkl}} = \left\{S_{3333}^{L}\right\}_{\psi}^{hkl} \tag{D.14}$$

On condition that the $\left\{S_{3333}^{L}\right\}_{\psi}^{hkl}$ components are independent of the angle ψ and ϕ and the material is quasi isotropic , the Eq. D.13 can be written as

$$\left\{\epsilon_{33}^{L}\right\}_{\psi}^{hkl} = \sigma^{S}(2\left\{s_1\right\}^{hkl} + \frac{1}{2}\left\{s_2\right\}^{hkl}\sin^2\psi) \tag{D.15}$$

in which the symbols $\{s_1\}^{hkl}$ and $\frac{1}{2}\{s_2\}^{hkl}$ represent isotropic X-ray elastic constants [1, 2]. The constants are sometimes substituted as [2]

$$\{s_1\}^{hkl} = -\frac{\{\nu\}^{hkl}}{\{E\}^{hkl}}, \frac{1}{2}\{s_2\}^{hkl} = \frac{1+\{\nu\}^{hkl}}{\{E\}^{hkl}} \tag{D.16}$$

The symbol $\{\nu\}^{hkl}$ represents the diffraction Poisson's number. In the case of macroscopic elastic isotropic aggregates, $\{E\}^{hkl}$ and $\{\nu\}^{hkl}$ can be calculated using Eqs. 15 and 16 provided $\left\{\epsilon_{33}^{L}\right\}_{\psi}^{hkl}$ and σ^{S} are known.

D.6 Calculation of diffraction elastic moduli

X ray elastic compliances $\left\{S_{33ij}^{L}\right\}_{\psi}^{hkl}$ express elastic behavior of the aggregate along the diffraction vector $\vec{Q}_{hkl}$. In Fig. D.6, Young's moduli of 111 fiber-textured Cu and CrN thin films are presented as a function of the tilt angle ψ.

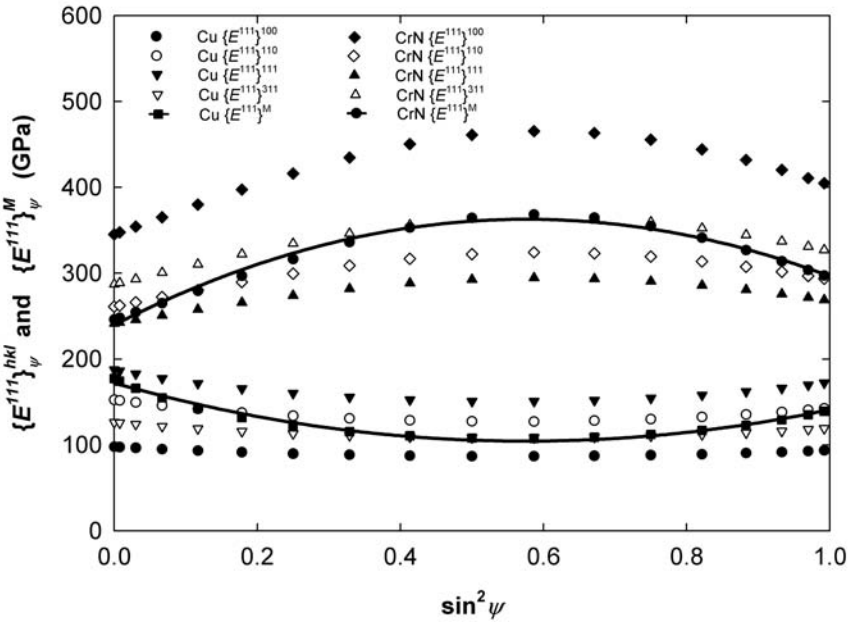

Figure D.6: Exemplary diffraction $\left\{E^{111}\right\}_{\psi}^{hkl}$ and mechanical $\left\{E^{111}\right\}_{\psi}^{\mathrm{M}}$ Young's moduli of Cu and CrN films with 111 fiber texture as a function of the sample tilt angle ψ. The moduli were calculated using the ODF from Fig. D.2 supposing the Hill grain interaction model [15].

The data in Fig. D.6 document that the mechanical moduli $\{E^{111}\}_{\psi}^{\mathrm{M}}$ always lies between $\{E^{111}\}_{\psi}^{111}$ and $\{E^{111}\}_{\psi}^{100}$ diffraction moduli for materials with different crystal elastic anisotropy even in the case of very sharp 111 fiber texture (Fig. D.2). For $\psi = 0$ the *out-of-plane* mechanical modulus $\{E^{111}\}_{\psi=0}^{\mathrm{M}}$ approaches the $\{E^{111}\}_{\psi=0}^{111}$ values because of the specific texture type. Since, in cubic crystals, (111) crystallographic plane possesses an in-plane elastic isotropy the in plane mechanical modulus $\{E^{111}\}_{\psi=90}^{\mathrm{M}}$ approaches the diffraction modulus $\{E^{111}\}_{\psi=90}^{mnp}$ of (mnp) crystallographic plane (with $m{+}n{+}p{=}0$) which is perpendicular to the (111) plane (*e.g.* $(1\vec{1}0)$). It should be mentioned that this relatively simplified behavior can be observed only in the case of 111 fiber textures. In the case of thin film with other type of *uvw* fiber texture, the magnitude of the in-plane modulus $\{E^{uvw}\}_{\psi=90}^{\mathrm{M}}$ is influenced by the elastic anisotropy of the *uvw* plane.

D.7 A comparison of mechanical and X-ray elastic constants

D.7.1 General considerations

The results in Fig. D.6 demonstrate that the mechanical elastic constants $\left\{S_{33ij}^{L}\right\}_{\psi}^{\mathrm{M}}$ are constrained by the X-ray elastic constants $\left\{S_{33ij}^{L}\right\}_{\psi}^{hkl}$. A comparison of the Eqs. D.3 and D.10 moreover indicates that the behavior of the Reuss grain interaction model predefines under which conditions $\left\{S_{33ij}^{L}\right\}_{\psi}^{hkl} = \left\{S_{33ij}^{L}\right\}_{\psi}^{\mathrm{M}}$. It is therefore obvious that, by considering a specific ODF, tilt angle ψ and single crystal elastic constants, it is always possible to determine a reflection *hkl* and a corresponding X-ray anisotropy factor $3\Gamma_{hkl}^{*}$ for which the X-ray elastic constants are equal to their mechanical counterparts (Fig. D.6). Further in the text, $3\Gamma_{hkl}^{*}$ will therefore denote conditions according to the Hill model under which $\left\{S_{33ij}^{L}\right\}_{\psi}^{hkl} = \left\{S_{33ij}^{L}\right\}_{\psi}^{\mathrm{M}}$.

D.7.2 Isotropic case

In the case of polycrystalline materials with crystal elastic isotropy or with negligible macroscopic elastic anisotropy, $\{E\}^{hkl}$ and $\{\nu\}^{hkl}$ as well as $\{s_1\}^{hkl}$ and $\frac{1}{2}\{s_2\}^{hkl}$ are independent of the angle ψ and the Eq. D.15 supposes moreover a linear dependence of $\{\epsilon_{33}^{L}\}_{\psi}^{hkl}$ on $\sin^2\psi$ [2]. Provided that the elastic strain $\{\epsilon_{33}^{L}\}_{\psi}^{hkl}$ and the macroscopic stress σ^{S} can be determined by an experiment, the isotropic X-ray elastic constants $\{s_1\}^{hkl}$ and $\frac{1}{2}\{s_2\}^{hkl}$ and subsequently also $\{E\}^{hkl}$ and $\{\nu\}^{hkl}$ can be obtained by solving a system of linear equations of Eq. D.15 type when $\{\epsilon_{33}^{L}\}_{\psi}^{hkl}$ is known for different ψ [26, 27]. An example of this procedure is presented in Fig. D.7. Considering the single crystal elastic constants from Tab. D.1 and an in plane isotropic stress $\sigma^{S} = 100$ MPa, calculated diffraction strains $\{\epsilon_{33}^{L}\}_{\psi}^{hkl}$ for a quasi-isotropic Cu thin film are presented in Fig. D.7a.

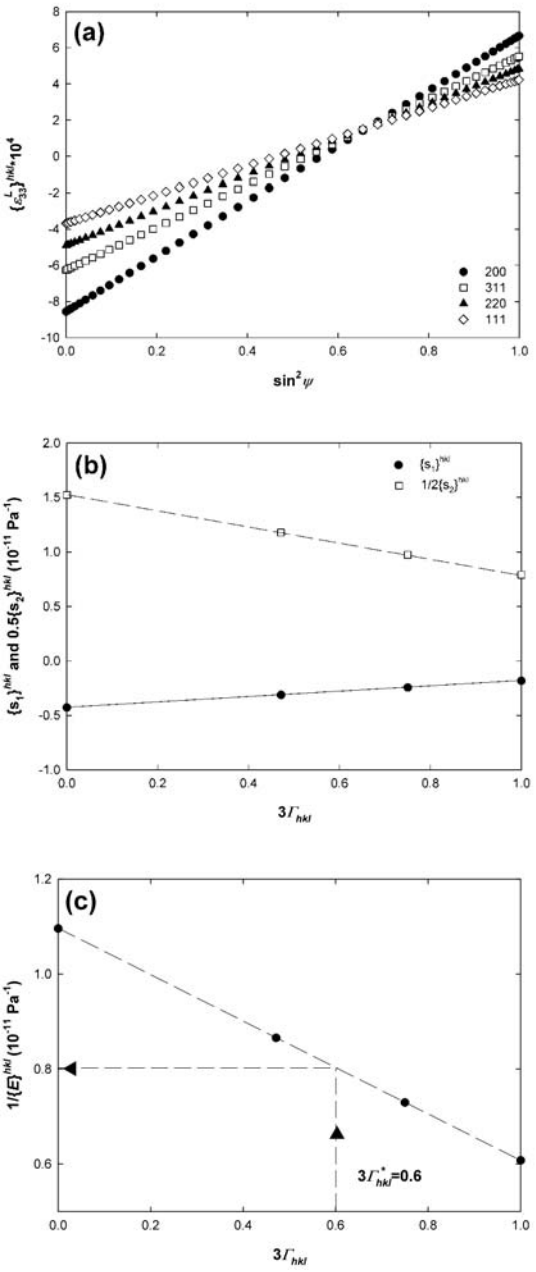

Figure D.7: Calculated X-ray elastic strains in a quasi-isotropic Cu thin film (a). In (b) X-ray elastic constants $\{s_1\}^{hkl}$ and $\frac{1}{2}\{s_2\}^{hkl}$ refined from (a) are plotted as a function of $3\Gamma_{hkl}$. In (c) reciprocal diffraction Young's moduli $1/\{E\}^{hkl}$ obtained from (b) are shown. The mechanical modulus $\{E\}^{\mathrm{M}}$ can be extrapolated for $3\Gamma^*_{hkl} = 0.6$ resulting in 123.45 GPa.

According to Eq. D.15, the slopes in Fig. D.7a correspond to $\frac{1}{2}\{s_2\}^{hkl}$ and the intercepts on $\{\epsilon_{33}^L\}_{\psi}^{hkl}$ axis can be correlated with $\{s_1\}^{hkl}$ magnitude. In practical cases, the X-ray elastic constants are obtained by fitting the experimental data from Fig. D.7a using Eq. D.15. Reciprocal diffraction elastic moduli $1/\{E\}^{hkl}$ in Fig. D.7c can be then determined from $\{s_1\}^{hkl}$ and $\frac{1}{2}\{s_2\}^{hkl}$ (Fig. D.7b) as follows

$$\frac{1}{\{E\}^{hkl}} = \{s_1\}^{hkl} + \frac{1}{2}\{s_2\}^{hkl} \tag{D.17}$$

The reciprocal mechanical modulus $1/\{E\}_{\psi}^{\mathrm{M}} = 0.81 * 10^{-11}$ Pa^{-1} was extrapolated from the reciprocal diffraction moduli $1/\{E\}_{\psi}^{hkl}$ supposing $1/\{E\}^{\mathrm{M}} = 1/\{E\}^{hkl}$ for $3\Gamma_{hkl}^* = 0.6$, as predicted by the Hill grain interaction model for quasi-isotropic materials [13]. The mechanical modulus $\{E\}^{\mathrm{M}}$ is therefore 123.45 GPa. This procedure is however valid only in the case of elastic isotropic aggregates.

D.8 Fiber-textured thin films

The procedure described in Fig. D.7 represents an often used simplification. Polycrystalline thin films are however usually macroscopic elastic anisotropic and therefore the extrapolation of the mechanical modulus from X-ray elastic constants for $3\Gamma_{hkl}^* = 0.6$ would work only for elastic isotropic materials like tungsten.
In majority of cases, polycrystalline thin films possess a certain *uvw* fiber texture with the fiber axis oriented perpendicular to the substrate surface. Moreover there is always a non zero ISO present in the film. In that case, the mechanical and X ray elastic compliances are dependent on the angle ψ (Fig. D.5,D.6). In order to determine experimental $\left\{S_{33ij}^L\right\}_{\psi}^{\mathrm{M}}$ from $\left\{S_{33ij}^L\right\}_{\psi}^{hkl}$ it is necessary to apply exact $3\Gamma_{hkl}^*$ which is also dependent on ψ, as demonstrated in Fig. D.6. In the next, the possibilities to determine $\left\{S_{33ij}^L\right\}_{\psi}^{\mathrm{M}}$ and $\{E\}_{\psi}^{\mathrm{M}}$ from experimental $\left\{S_{33ij}^L\right\}_{\psi}^{hkl}$ applying the X-ray diffraction Hook's law (Eq. D.13) are discussed.

(i) In the case of in-plane elastic isotropic films $\left\{S_{3311}^L\right\}_{\psi=0}^{hkl}$ is equal to $\left\{S_{3322}^L\right\}_{\psi=0}^{hkl}$ for $\psi = 0$ and Eq. D.13 reduces to $\left\{\epsilon_{33}^L\right\}_{\psi=0}^{hkl} = 2\left\{S_{3311}^L\right\}_{\psi=0}^{hkl}$. $\left\{S_{3311}^L\right\}_{\psi=0}^{hkl}$ can be determined experimentally by evaluating the intercept of the $\sin^2\psi$ dependence on the $\left\{\epsilon_{33}^L\right\}^{hkl}$ axis when σ^S is known. The dependence of $\left\{S_{3311}^L\right\}_{\psi=0}^{hkl}$ on $3\Gamma_{hkl}$ could then be used to determine the thin film mechanical compliance

$$\left\{S_{3311}^S\right\}^{\mathrm{M}} \tag{D.18}$$

(ii) By comparing the intercepts $2\left\{S_{3311}^L\right\}_{\psi=0}^{hkl}$ and the slopes $\left\{S_{3333}^L\right\}_{\psi}^{hkl} - \left\{S_{3311}^L\right\}_{\psi}^{hkl}$ of the $\sin^2\psi$ curves for $\psi \to 0$ (and by simultaneous neglecting the term

$\left\{S^L_{3313}\right\}^{hkl}_{\psi} \sin 2\psi$, since $\left\{S^S_{3313}\right\}^{hkl} = \left\{S^L_{3313}\right\}^{hkl}_{\psi=0}$ for hexagonal macroscopic symmetry of the sample [28], the Eq. D.13 can be used to extract $\left\{S^L_{3333}\right\}^{hkl}_{\psi}$ and the diffraction *out-of-plane* modulus $\{E\}^{hkl}_{\psi=0}$ similar as in Sec. D.7.1. By considering the macroscopic elastic anisotropy, the knowledge of $\{E\}^{hkl}_{\psi=0}$ can be used to determine mechanical Young's modulus $\{E\}^{\mathrm{M}}_{\psi=0}$ or the term

$$\left\{S^S_{3333}\right\}^{\mathrm{M}} \tag{D.19}$$

(iii) Since for $\psi \neq 0$ $\left\{S^L_{3311}\right\}^{hkl}_{\psi} \neq \left\{S^L_{3322}\right\}^{hkl}_{\psi}$ in the case of fiber textured thin films with the fiber axis oriented parallel to $\vec{S}_3$, the diffraction Hook's law from Eq. D.13 can not be used to extract $\left\{S^L_{3333}\right\}^{hkl}_{\psi}$ [and subsequently $\{E\}^{hkl}_{\psi}$] for *arbitrary* ψ angle. From the slopes of $\sin^2\psi$ dependencies, however, one can determine the term $\left\{S^L_{3333}\right\}^{hkl}_{\psi} - \left\{S^L_{3311}\right\}^{hkl}_{\psi}$ which dependence on $3\Gamma_{hkl}$ can be used to evaluate the expression

$$\left\{S^L_{3333}\right\}^{\mathrm{M}}_{\psi} - \left\{S^L_{3311}\right\}^{\mathrm{M}}_{\psi} \tag{D.20}$$

For $\psi \rightarrow 90°$, the Eq. D.20 is equivalent to

$$\left\{S^S_{1111}\right\}^{\mathrm{M}}_{\psi} - \left\{S^S_{1133}\right\}^{\mathrm{M}}_{\psi} \tag{D.21}$$

(iv) By evaluating the intercepts on the $\left\{\epsilon^L_{33}\right\}^{hkl}$ axis for $\psi = 90°$, the Eq. D.13 can be used to determine the term $\left\{S^L_{3333}\right\}^{hkl}_{\psi=90} + \left\{S^L_{3322}\right\}^{hkl}_{\psi=90}$ which, in this special case, can be used to quantify in-plane biaxial modulus of the thin film

$$\left\{S^S_{1111}\right\}^{\mathrm{M}} + \left\{S^S_{1122}\right\}^{\mathrm{M}} \tag{D.22}$$

In order to quantify the parameters defined in Eqs. D.18-D.22, the macroscopic elastic anisotropy of the film must be considered. Further, the determination of *out-of-plane* moduli $\{E\}^{\mathrm{M}}_{\psi=0} = 1/\left\{S^S_{3333}\right\}^{\mathrm{M}}$ from the X-ray elastic constants $\left\{S^L_{3333}\right\}^{hkl}_{\psi=0}$ will be only discussed (Eq. D.19).

D.9 Elastic modulus of 111 fiber-textured Cu

In Fig. D.8, calculated $\sin^2\psi$ dependencies for a Cu thin film with a strong 111 fiber texture from Fig. D.2 are presented in Fig. D.8. The plots were calculated supposing an in plane isotropic stress of $\sigma^S = 100$ MPa and using the single crystal elastic constants from Tab. D.1.

The data in Fig. D.8a were evaluated according to the procedure described in Sec. D.8-ii and $\left\{S^L_{3333}\right\}^{hkl}_{\psi=0}$ values were determined (Fig. D.8b). Using the ODF from

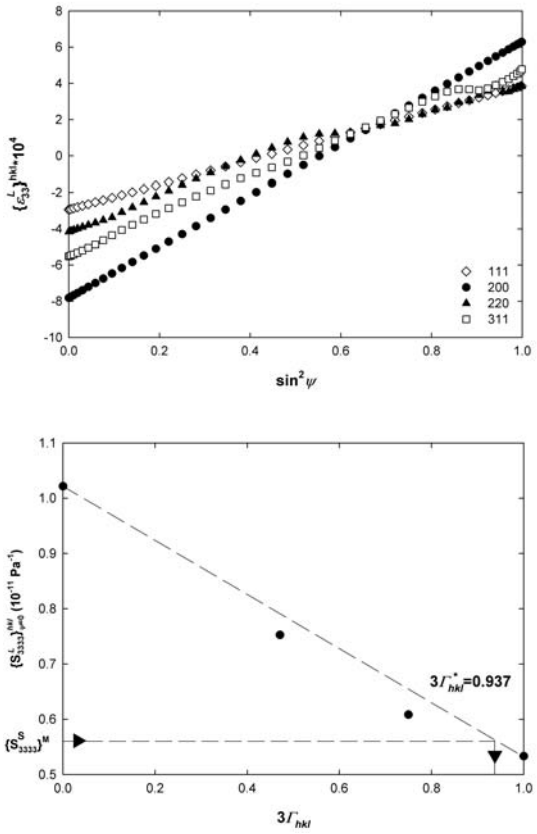

Figure D.8: Calculated X-ray elastic strains in a Cu thin film with a strong 111 fiber texture (a). In (b) X-ray compliances $\left\{S^L_{3333}\right\}^{hkl}_{\psi=0}$ refined from (a) are plotted as a function of $3\Gamma_{hkl}$. Since, for this special type of texture, the mechanical compliance $\left\{S^L_{3333}\right\}^{hkl}_{\psi=0} = 0.575 * 10^{-11}$ Pa^{-1}, $3\Gamma^*_{hkl} = 0.937$ was extrapolated from $\left\{S^L_{3333}\right\}^{hkl}_{\psi=0}$ dependence on $3\Gamma_{hkl}$.

Fig. D.2, *out-of-plane mechanical compliance* $\left\{S^L_{3333}\right\}^{\mathrm{M}}_{\psi=0}$ was additionally calculated with $\left\{E^{111}\right\}^{\mathrm{M}}_{\psi=0} = 174$ GPa. The comparison of *out-of-plane* X-ray and mechanical compliances showed that $\left\{S^S_{3333}\right\}^{\mathrm{M}}_{\psi=0} = \left\{S^L_{3333}\right\}^{hkl}_{\psi=0}$ for $3\Gamma^*_{hkl} = 0.937$. This result demonstrate that, in order to determine $\left\{S^L_{3333}\right\}^{\mathrm{M}}_{\psi=0}$ from $\left\{S^L_{3333}\right\}^{hkl}_{\psi=0}$ (*i.e.* to apply an opposite algorithms flow as that from Fig. D.8b), it is necessary to know a specific $3\Gamma^*_{hkl}$ value (Fig. D.8b) which is strongly texture dependent.

D.10 $\Gamma^*_{hkl} - \Gamma_{uvw}$ plot

In the case of cubic uvw fiber textured films with the fiber axis oriented perpendicularly to the substrate surface, the texture type will be further described using the parameters Γ_{uvw} defined as [13, 21]

$$\Gamma_{uvw} = \frac{u^2v^2 + v^2w^2 + w^2u^2}{(u^2 + v^2 + w^2)^2} \tag{D.23}$$

Supposing various *uvw* fiber textures (i) with the texture sharpness ψ_{FWHM} from the range 0-60 degrees (Fig. D.2), (ii) with the $3\Gamma_{uvw}$ from the range 0-1 and (iii) with the ISO from the range 0-100%, numerous ODFs were generated. Following the algorithm from Sec. D.8-ii, $\left\{S^L_{3333}\right\}^{hkl}_{\psi=0}$ and $\left\{S^L_{3333}\right\}^{\mathrm{M}}_{\psi=0}$ values were calculated numerically for materials with Zener's anisotropy ratio from the range 0.36-9.95 (corresponding to KCl and Na). Then the mechanical and X-ray elastic constants were compared with an aim to find out for which $3\Gamma^*_{hkl}$ value $\left\{S^S_{3333}\right\}^{\mathrm{M}}_{\psi=0} = \left\{S^L_{3333}\right\}^{hkl}_{\psi=0}$. As a results $3\Gamma^*_{hkl} - 3\Gamma_{uvw}$ plots were constructed indicating how the $3\Gamma^*_{hkl}$ depend on the *uvw* fiber texture type, on ψ_{FWHM} (Fig. D.9a) and on ISO (Fig. D.9b).

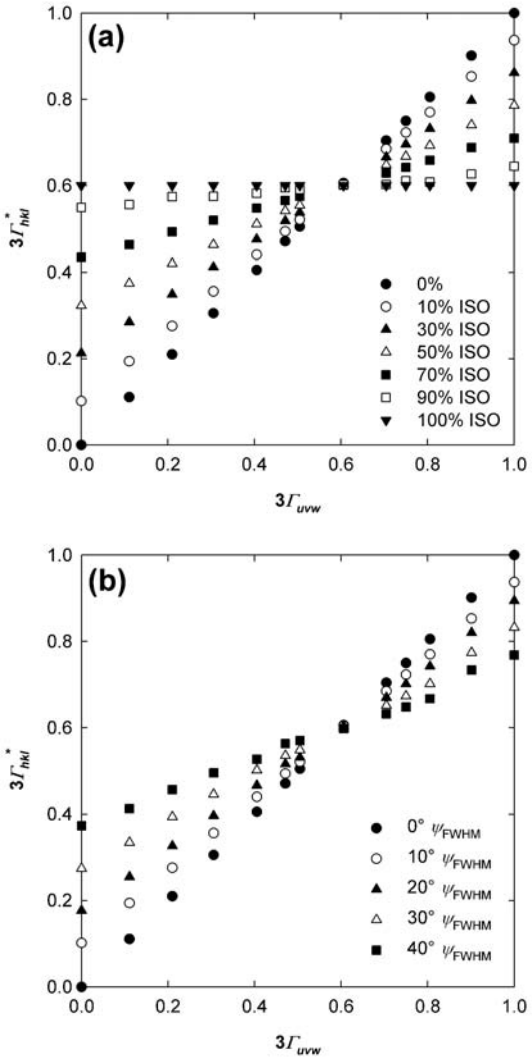

Figure D.9: $\Gamma^*_{hkl}-\Gamma_{uvw}$ plots indicate for which hkl reflection (and the corresponding $3\Gamma^*_{hkl}$ value) the X-ray elastic constants $\left\{S^L_{3333}\right\}^{hkl}_{\psi=0}$ are equal to the mechanical constants $\left\{S^L_{3333}\right\}^{\mathrm{M}}_{\psi=0}$. $3\Gamma^*_{hkl}$ values are plotted as a function of the fiber texture type expressed through Γ_{uvw}. In (a) the dependence of $3\Gamma^*_{hkl}$ on the fraction of randomly oriented crystallites from the range 0-100 % is plotted for various uvw textures with $\psi_{\mathrm{FWHM}} = 10$ degrees. In (b) the dependence of $3\Gamma^*_{hkl}$ on ψ_{FWHM} is plotted for various uvw textures supposing 10 % fraction of randomly oriented crystallites.

The $\Gamma^*_{hkl} - \Gamma_{uvw}$ plots from Fig. D.9 do not depend on the crystal elastic anisotropy of the thin film material and represent therefore a certain type of a universal plot valid for all materials (except those (like tungsten) where $ZAR \cong 1$ and therefore Γ^*_{hkl} is arbitrary).
In Fig. D.9a, one can notice that for very sharp *uvw* fiber textures with $\psi_{\mathrm{FWHM}} = 10$ degrees and small or no fraction of randomly oriented crystallites the X-ray elastic constants corresponds approximately to the mechanical constants for $3\Gamma^*_{hkl} - 3\Gamma_{uvw}$. In other words, in order to determine *out-of-plane* modulus of a thin film with a very sharp *uvw* texture one has to characterize X-ray elastic constants of *uvw* reflections. In any case, the $3\Gamma^*_{hkl}$ value must be selected from the intervals [$3\Gamma_{uvw}$,0.6] or [0.6,$3\Gamma_{uvw}$] for thin films with *uvw* fibre texture. When the fraction of randomly oriented crystallites ISO however increases, X-ray elastic constants of *hkl* reflections for which $3\Gamma^*_{hkl} \rightarrow 0.6$ should be quantified. Similarly in Fig. D.9b, the decrease of the texture sharpness results in the behavior which is typical for elastic isotropic materials and $3\Gamma^*_{hkl} \rightarrow 0.6$. In case of a sharp *uuu* or *u*00 fiber textures the search for exact $3\Gamma^*_{hkl}$ value is extremely important because the application of the procedure from Sec. D.7.2 (valid for elastic isotropic materials) could result in a large error when determining the *out-of-plane* moduli. For the films with *uvw* fibre textures with $3\Gamma^*_{hkl} \rightarrow 0.6$ even the procedure from Sec. D.7.1 could provide relevant results.
The results in Figs. D.9a,b represents a example of the $\Gamma^*_{hkl} - \Gamma_{uvw}$ selection rule. In order to express the dependence of $3\Gamma^*_{hkl}$ plot on the $3\Gamma_{uvw}$, on ψ_{FWHM} and on ISO generally and in an "user-friendly way", the following empirical equation was derived:

$$3\Gamma^*_{hkl} = A + 3\Gamma_{uvw}(1 - \frac{A}{0.6}) \tag{D.24}$$

where $A = (\psi_{\mathrm{FWHM}} * 8.8 + \mathrm{ISO} * 5.8 - \psi_{\mathrm{FWHM}} * \mathrm{ISO} * 0.083)/1000$.
The Eq. D.24 provides an easy way how to determine $3\Gamma^*_{hkl}$ values considering macroscopic elastic anisotropy. The parameters in Eq. D.24 can be obtained from pole figure data (Fig. D.2) or they can be extracted from an ODF analysis of experimental pole figures. The ODF analysis is recommended especially in the case of sharp mixed textures or texture gradients. It is important to note that in the quantification of $3\Gamma^*_{hkl}$ value using Eq. D.24 the crystal elastic anisotropy does not play a role.
The Eq. D.24 represents a simple practical tool which can be used to decide for which *hkl* reflection the $\sin^2\psi$ measurements should be performed in order to determine (or extrapolate) the X-ray elastic strain. That strain and the stress can be used to quantify out-of plane Young's moduli. It is obvious that the considerations from Secs. 4.1-4.5 can be extended to determine also other mechanical elastic constants of thin films (*e.g.* in plane biaxial moduli [Eq. D.22]). Therefore, there is a need for a general approach to compare $\left\{S^L_{33ij}\right\}^{\mathrm{M}}_{\psi}$ and $\left\{S^L_{33ij}\right\}^{hkl}_{\psi}$ for various fiber texture types.
In the next paper of this series, an application of the formalism derived above will be demonstrated on polycrystalline Cu and CrN thin films.

D.11 Conclusion

Supposing the Hill grain interaction model, it was demonstrated that X-ray elastic constants can be used to determine mechanical elastic constants of cubic thin films with strong fiber textures. For this purpose, numerically calculated X-ray elastic constants of polycrystalline films were compared with their mechanical counterparts. The results document that the algorithm to determine the mechanical elastic constants strongly depends on the fiber texture type, texture sharpness and the amount of randomly oriented crystallites in the polycrystalline aggregate. For this purpose a certain type of universal plot (and equation) was derived. An important fact is that the derived algorithm is independent of crystal elastic anisotropy.

D.12 Acknowledgement

This work was supported by the Austrian NANO Initiative via a grant from the Austrian Science Fund FWF within the project "StressDesign - Development of Fundamentals for Residual Stress Design in Coated Surfaces".

D.13 References

[1] Dölle, H. *J. Appl. Cryst.* **12**, 489–501 (1979).

[2] Noyan, I. C. and Cohen, J. B. *Residual Stress Measurement by Diffraction and Interpretation.* Springer, (1987).

[3] Barral, M., Lebrun, J., Sprauel, J., and Maeder, G. *Metall. Mater. Trans. A* **18**(7), 1229–1238 (1987).

[4] van Houtte, P. and De Buyser, L. *Acta metall. mater.* **41**(2), 323–336 (1993).

[5] Badawi, K. F., Villain, P., Goudeau, P., and Renault, P. O. *Appl. Phys. Lett.* **80**(25), 4705–4707 (2002).

[6] Welzel, U., Leoni, M., Lamparter, P., and Mittemeijer, E. J. *J. Mater. Sci. Technol.* **18**(2), 121–124 (2002).

[7] Eiper, E., Martinschitz, K. J., Gerlach, J. W., Lackner, J. M., Zizak, I., Darowski, N., and Keckes, J. *Zeitschrift fr Metallkunde* **96**(9), 1069–1073 (2005).

[8] Eiper, E., Martinschitz, K. J., and Keckes, J. *Powder Diffr.* **21**(1), 25–29 (2006).

[9] Keckes, J., Eiper, E., Martinschitz, K. J., Köstenbauer, H., Daniel, R., and Mitterer, C. *Rev. Sci. Instrum.* **78**(3), – (2007).

[10] Martinschitz, K. J., Eiper, E., Massl, S., Köstenbauer, H., Daniel, R., Fontalvo, G., Mitterer, C., and Keckes, J. *J. Appl. Cryst.* **39**, 777–783 (2006).

[11] Stoney, G. G. *Proc. Phys. Soc. London, Sect. A* **82**, 172 (1909).

[12] Segmüller, A., Noyan, I. C., and Speriosu, V. S. *Prog. Cryst. Growth Charact. Mater.* **18**, 21–66 (1989).

[13] Bollenrath, F., Hauk, V., and Müller, E. H. *Z. Metallkd.* **58**, 76–82 (1967).

[14] Reuss, A. *Z. Angew. Math. Mech.* **9**(1), 49–58 (1929).

[15] Hill, R. *Proc. R. Soc. London, Ser. A* **65**(389), 349–355 (1952).

[16] Bunge, H. J. and Roberts, W. T. *J. Appl. Cryst.* **2**, 116–xxx (1969).

[17] Bunge, H. J. *Texture Analysis in Materials Science.* Butterworths, London, (1982).

[18] Martinschitz, K. J., Daniel, R., Mitterer, C., and Keckes, J. *J. Appl. Cryst.* , Second paper in series (2008).

[19] Nye, J. F. *Physical Properties of Crystals.* Oxford Univ. Press, (1976).

[20] Suresh, S. and Freund, L. B. *Thin Film Materials Stress, Defect Formation and Surface Evolution.* Cambridge University Press, Cambridge, (2003).

[21] Huang, F. and Weaver, M. L. *J. Appl. Phys.* **98**(7) (2005).

[22] Zener, C. *Elasticity and Anelasticity of Metals.* University of Chicago Press, Chicago, (1948).

[23] Birkholz, M. *Thin Film Analysis by X-Ray Scattering.* WILEY-VCH, (2006).

[24] Serruys, W. *Röntgenografisch meten van restspanningen in getextureerd materiaal.* PhD thesis, Katholieke Universiteit Leuven, (1988).

[25] Stickforth, J. *Tech. Mitt. Krupp - Forsch.-Ber.* **24**(3), 89–102 (1966).

[26] Ortner, B. *Adv. X-ray Anal.* **29**, 113–118 (1986).

[27] Ortner, B. *Adv. X-ray Anal.* **29**, 387–394 (1986).

[28] Martinschitz, K. J. *Mechanical elastic constants of thin films determined by X-ray diffraction.* PhD thesis, Leoben, (2008).

Elastic constants of fiber-textured thin films determined by X-ray diffraction. II. Examples

K.J. Martinschitz[a], R. Daniel[b], Ch. Mitterer[b] and J. Keckes[a]

[a]Erich Schmid Institute for Materials Science, Austrian Academy of Science and Department of Materials Physics, University of Leoben, Austria
[b]Department of Physical Metallurgy and Materials Testing and Christian-Doppler Laboratory for Advanced Hard Coatings, University of Leoben, Leoben, Austria

Abstract An experimental application of a new simple self-consistent X-ray diffraction technique introduced in our previous work is demonstrated. The technique is applied to determine out-of-plane Young's moduli of 111 and 311 fiber textured thin films deposited on monocrystalline Si(100) substrates. The moduli are calculated from macroscopic stresses and elastic strains quantified using a static diffraction experiment and considering the thin film texture. The advantage of the new technique remains in the fact that moduli are determined non-destructively and represent volume-averaged quantities.

E.1 Synopsis

A new simple self-consistent X-ray diffraction technique was used to quantify out-of-plane Young's moduli of fiber textured thin films. The advantage of the new technique remains in the fact that moduli are determined non-destructively and using a static diffraction experiment.

E.2 Introduction

The reliability and the performance of thin films used *e.g.* in microelectronics or as protective coatings on working tools is closely related to their mechanical properties [1, 2]. Advanced characterization techniques operating on very small scale have been used to assess phenomena like residual stress, yield stress, hardness *etc.* [1]. Elastic properties of thin films are usually determined by nanoindentation [3], by surface acoustic wave technique [4], by straining or bending of thin film structures [5] or by resonance ultrasound spectroscopy [6].

Recently, it has been demonstrated that X-ray elastic *strain* and macroscopic *stress* in polycrystalline thin films can be rapidly determined by a *simultaneous* application of $\sin^2\psi$ and X ray diffraction substrate curvature techniques [7–9]. The experimental strain and stress can be used to quantify X-ray elastic constants and stress factors. In the previous paper of this series, it was demonstrated under which conditions the knowledge of the X-ray elastic constants can be used to assess *mechanical elastic constants of fiber-textured polycrystalline aggregates* supposing the Hill grain interaction model [10]. It was shown that the macroscopic elastic anisotropy plays a decisive role and, in order to determine *out-of-plane* Young's modulus, the fiber texture type, the texture sharpness and the amount of randomly oriented crystallites in the aggregate must be considered.

The aim of this work is to demonstrate a practical application of the new *self-consistent X-ray diffraction technique* described in the previous paper. *Out-of-plane Young's moduli* of fiber-textured Cu and CrN thin films are determined using X-ray diffraction under static conditions. The main reason to select Cu and CrN was that these materials exhibit a different type of crystal elastic anisotropy and both are extensively used in engineering applications. For a better understanding, it is recommended to read at first the previous paper of this series.

E.3 Experiment

Cu and CrN thin films were deposited on Si(100) using the Balzers RCS coating system. In order to induce a measurable substrate curvature and to avoid a substrate plastic deformation, monocrystalline Si(100) wafers with the thickness of 140 and 400 μm and lateral dimensions of 30 x 8 mm^2 were chosen for the deposition of Cu and CrN films, respectively. The substrates were ultrasonically cleaned in acetone and alcohol and Ar etched prior to the deposition. The Cu was deposited in argon atmosphere at

room temperature and then annealed at 400 °C for 10 minutes in order to increase the residual stress (and substrate curvature) magnitude. The 3 μm thick CrN thin film was deposited at a temperature of 350 °C. The thickness of Cu and CrN thin films was determined from a film cross-section using a scanning electron microscope and yields 0.6 and 3 μm, respectively.
The substrate curvature, elastic strain and texture of Cu and CrN on Si(100) were characterized in laboratory conditions using a Seifert 3000 PTS four-circle diffractometer. The setup comprised Cu K_α radiation, polycapillary optics on the primary side, Soller slits, a graphite monochromator and a scintillation detector on the secondary side. For the elastic strain and curvature characterization, the beam size of 3.0 and 0.5 mm in diameter were chosen. The relatively large beam in the case of strain measurements enabled to assess volume-averaged properties. The limited pole figure characterization was performed using Schultz reflectivity technique with the beam of 2 mm in diameter whereby the ψ range was set to 0-80 degrees. The rectangular samples were glued just with one of their narrower side on sample holders to allow for the free bending when the strain and the curvature were characterized in the diffractometer.

E.4 Method and Results

E.4.1 Macroscopic elastic anisotropy

Texture in Cu and CrN thin films was characterized using pole figure measurements (Figs. E.1,E.2). The orientation distribution function was then calculated from the experimental data in order to assess the amount of randomly oriented crystallites (further denoted as ISO). In the case of Cu, one can easily identify a sharp 111 fiber texture (Fig. E.1) with the width at half maximum ψ_{FWHM} in the centre of 111 pole figure of 14 degrees and 10 % of ISO. For CrN, a 311 texture is visible in Fig. E.2 with $\psi_{\mathrm{FWHM}} = 12$ degrees and ISO of 13 %.
The experimental parameters ψ_{FWHM} and ISO were used to determine $3\Gamma^*_{hkl}$, a parameter denoting conditions according to the Hill grain-interaction model [11] under which X-ray and mechanical elastic constants are equal whereby

$$3\Gamma^*_{hkl} = A + 3\Gamma_{uvw}(1 - \frac{A}{0.6}) \tag{E.1}$$

where $A = (\psi_{\mathrm{FWHM}} * 8.8 + \mathrm{ISO} * 5.8 - \psi_{\mathrm{FWHM}} * \mathrm{ISO} * 0.083)/1000$ [10]. Γ_{uvw} in Eq. E.1 can be expressed as $\Gamma_{uvw} = (u^2v^2 + v^2w^2 + w^2u^2)/(u^2 + v^2 + w^2)^2$ where uvw denote the type of the fiber texture. For Cu and CrN thin films from Figs. E.2,E.3, it was found that $3\Gamma^*_{hkl}$ are equal to 0.89 and 0.51, respectively.

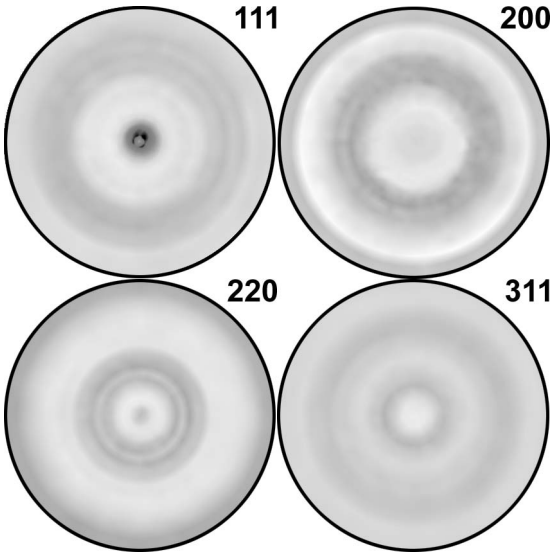

Figure E.1: Experimental Cu 111, 200, 220 and 311 pole figures document a 111 fiber texture in Cu thin film.

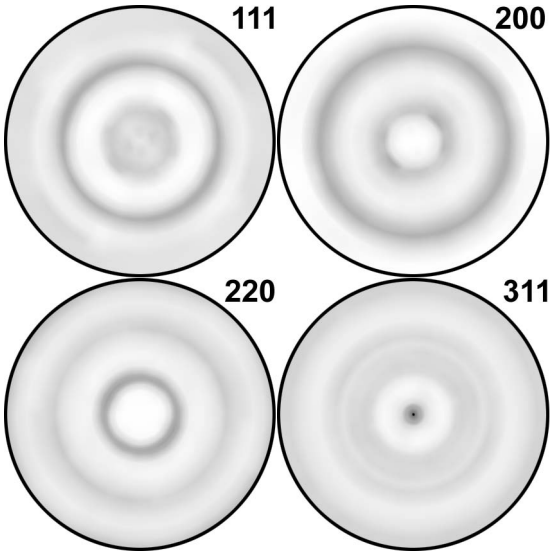

Figure E.2: Experimental CrN 111, 200, 220 and 311 pole figures document a 311 fiber texture.

E.5 Macroscopic stress characterized by X-ray diffraction substrate curvature technique

The pole figure measurements documented that the thin films are in-plane elastic isotropic. Since the films were unpassivated, the residual stress $\langle\sigma\rangle$ in the plane of the film was considered as in-plane isotropic and biaxial and the out of plane components σ_{3i} were neglected:

$$\langle\sigma\rangle = \sigma_{11} = \sigma_{22}, \sigma_{12} \cong 0 \; and \; \sigma_{i3} \cong 0. \tag{E.2}$$

The volume-averaged macroscopic stress in Cu and CrN polycrystalline thin films was determined using X-ray diffraction substrate curvature method which will be briefly described [12–15]. The quantification of the curvature was performed by the measurement of rocking curves of Si 400 reflections at different sample positions x_i (Fig. E.2).

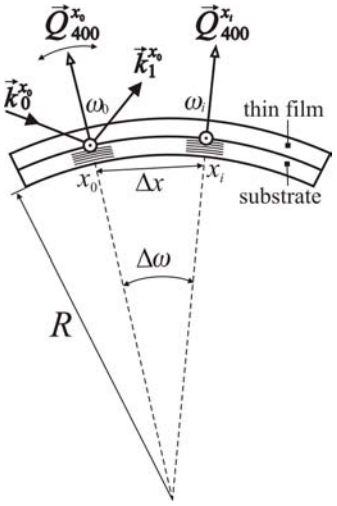

Figure E.3: A schematic description of the X-ray diffraction substrate curvature setup used for the characterization of the sample curvature radius R. The angle between the primary and the secondary diffraction vectors $\vec{k}_0^{x_i}$ and $\vec{k}_1^{x_i}$, respectively, was set to the position corresponding to the Si 400 2θ angle of 69.13 degrees. Then, for each x_i position, the sample was rotated around the ω axis and the intensity was collected as a function of the ω angle with the peak maximum at ω_i. The dependence of $\Delta\omega = \omega_0 - \omega_i$ on $\Delta x = x_0 - x_i$ was used to quantify R (Eqs. E.1,E.2).

For each x_i position, the sample was rotated around the ω axis (Fig. E.3) and the intensity was collected as a function of the ω angle yielding a peak at the angle of ω_i. In Fig. E.4, the plots of $\Delta\omega$ dependence on Δx are presented for Cu/Si(100) and CrN/Si(100) samples.

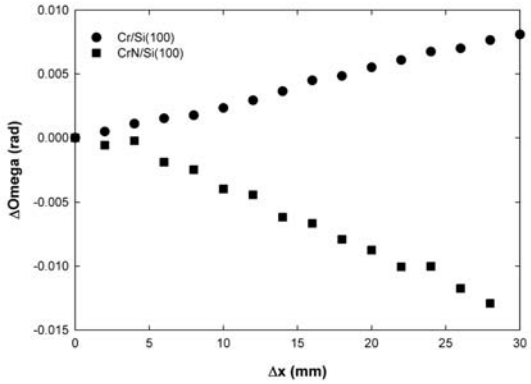

Figure E.4: The plots of $\Delta\omega$ dependence on Δx for Cu/Si(100) and CrN/Si(100) samples. The results document different radii of the curvature R (Eq. E.1) with 2.193 and 3.572 m for Cu and CrN. The convex and the concave bending (*c.f.* Fig. E.2) correspond to tensile and compressive stresses of 275.9 and -1415.9 MPa in Cu and CrN, respectively.

The data in Fig. E.4 were used to calculate the radius of the curvature R according to

$$R \cong (\frac{\partial\Delta\omega}{\partial\Delta x})^{-1}, \tag{E.3}$$

where $\partial\Delta\omega/\partial\Delta x$ represents the slope of the linear dependency. Applying R, it was possible to determine the macroscopic in-plane isotropic residual stress $\langle\sigma\rangle$ in the films using the Stoney formula [12]

$$\langle\sigma\rangle = \frac{E}{6(1-\nu)}\frac{h_\mathrm{s}^2}{h_\mathrm{f}}\frac{1}{R}, \tag{E.4}$$

where h_s and h_f stands for substrate and film thickness, respectively, and the term $E/(1-\nu) = 181$ GPa is the biaxial modulus of the silicon substrate [1]. The macroscopic stress $\langle\sigma\rangle$ in Cu and CrN films (Tab. E.1) was determined with the precision of about ± 10 %.

E.6 Elastic strain in thin films

In Figs. E.5a,b X-ray elastic strains $\left\{\epsilon_{33}^{L}\right\}_{\psi}^{hkl}$ in Cu and CrN films for different *hkl* reflections are presented as a function of the sample tilt angle ψ. In the case of Cu the dependencies are approximately linear whereby for CrN films one can identify relatively strong nonlinearities which can be attributed to the macroscopic elastic anisotropy (texture). The different crystal elastic anisotropy causes that

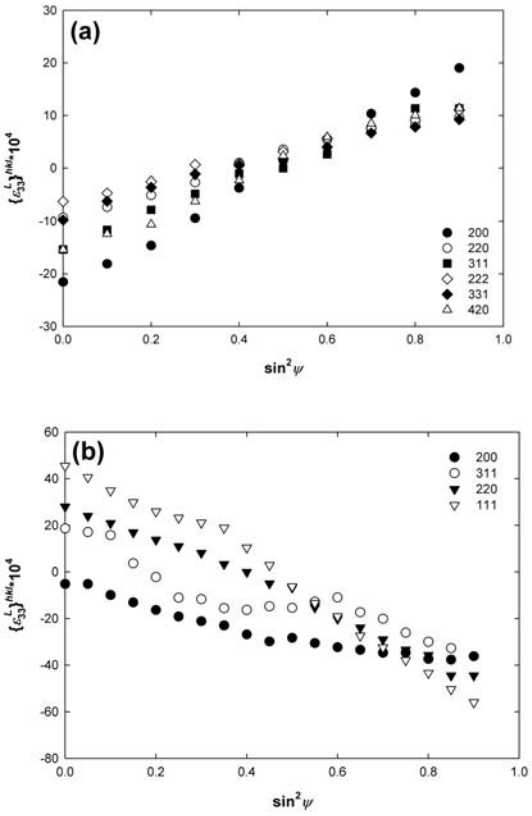

Figure E.5: Measured X-ray elastic strains $\left\{\epsilon_{33}^{L}\right\}_{\psi}^{hkl}$ in Cu (a) and CrN (b) thin films as a function of the sample tilt angle ψ. Positive (a) and negative (b) slopes indicate tensile and compressive stresses in Cu and CrN, respectively.

$$\partial\left\{\epsilon_{33}^{L}\right\}_{\psi=0}^{200}/\partial\sin^2\psi > \partial\left\{\epsilon_{33}^{L}\right\}_{\psi=0}^{hkl}/\partial\sin^2\psi$$

for Cu and

$$\partial\left\{\epsilon_{33}^{L}\right\}_{\psi=0}^{111}/\partial\sin^2\psi > \partial\left\{\epsilon_{33}^{L}\right\}_{\psi=0}^{hkl}/\partial\sin^2\psi$$

for CrN in Fig. E.5.

E.7 X-ray and macroscopic elastic constants

According to the X-ray diffraction Hook's law, the elastic strain $\left\{\epsilon_{33}^{L}\right\}_{\psi}^{hkl}$ of a fiber textured film can be described as follows ([10, 16])

$$\left\{\epsilon_{33}^{L}\right\}_{\psi}^{hkl} = \sigma^{S}\lfloor(\left\{S_{3311}^{L}\right\}_{\psi}^{hkl} + \left\{S_{3322}^{L}\right\}_{\psi}^{hkl}) + (\left\{S_{3333}^{L}\right\}_{\psi}^{hkl} - \left\{S_{3311}^{L}\right\}_{\psi}^{hkl})\sin^2 + \left\{S_{3313}^{L}\right\}_{\psi}^{hkl}\sin 2\psi\rfloor \quad \text{(E.5)}$$

where $\left\{S_{33ij}^{L}\right\}_{\psi}^{hkl}$ represent X-ray elastic constants for a reflection *hkl* measured at a tilt angle ψ. The X-ray elastic constants $\left\{S_{33ij}^{L}\right\}_{\psi}^{hkl}$ from Eq. E.2 can be obtained by a numerical fitting of the experimental X-ray elastic strains $\left\{\epsilon_{33}^{L}\right\}_{\psi}^{hkl}$ from Fig. E.5 applying the macroscopic stress values $\langle\sigma\rangle$ from Tab. E.1. This type of analysis was performed in order to evaluate (i) $\left\{S_{3311}^{L}\right\}_{\psi=0}^{hkl} + \left\{S_{3322}^{L}\right\}_{\psi=0}^{hkl}$ from the intercepts on the $\left\{\epsilon_{33}^{L}\right\}_{\psi}^{hkl}$ axis and (ii) $\left\{S_{3333}^{L}\right\}_{\psi\to=0}^{hkl} - \left\{S_{3311}^{L}\right\}_{\psi\to0}^{hkl}$ from the slopes in Fig. E.5. In Figs. E.6a,b, the fitted parameters $\left\{S_{3311}^{L}\right\}_{\psi=0}^{hkl} + \left\{S_{3322}^{L}\right\}_{\psi=0}^{hkl}$ and $\left\{S_{3333}^{L}\right\}_{\psi\to0}^{hkl} - \left\{S_{3311}^{L}\right\}_{\psi\to0}^{hkl}$ from Fig. E.5 are presented as a function of the X-ray anisotropic factor $3\Gamma_{hkl} = (h^2k^2 + k^2l^2 + l^2h^2)/(h^2 + k^2 + l^2)^2$ [17] for Cu and CrN thin films. Those parameters differ for various *hkl* reflections what is a consequence of crystal elastic anisotropy.

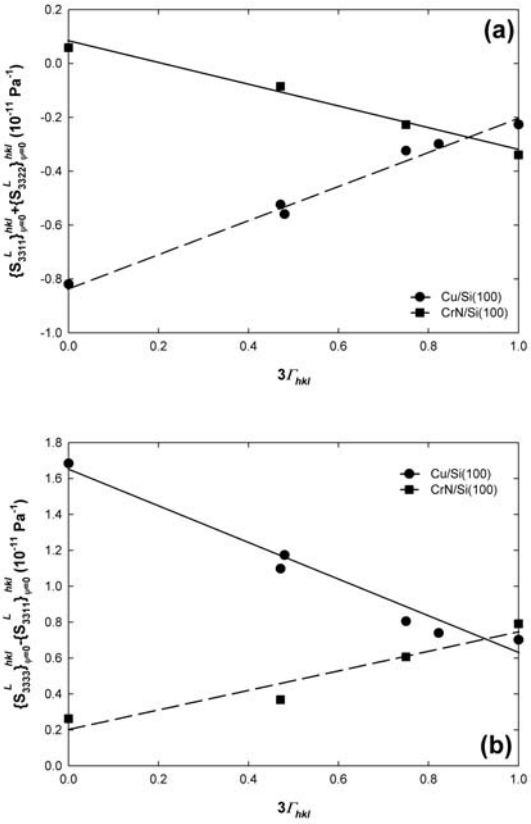

Figure E.6: Fitted X-ray elastic constants $\left\{S^L_{3311}\right\}^{hkl}_{\psi=0} + \left\{S^L_{3322}\right\}^{hkl}_{\psi=0}$ and $\left\{S^L_{3333}\right\}^{hkl}_{\psi=0} - \left\{S^L_{3311}\right\}^{hkl}_{\psi=0}$ obtained from the data in Fig. E.2 applying the macroscopic stress (Fig. E.4).

$\left\{S_{3311}^{L}\right\}_{\psi=0}^{hkl}+\left\{S_{3322}^{L}\right\}_{\psi=0}^{hkl}$ and $\left\{S_{3333}^{L}\right\}_{\psi\to 0}^{hkl}-\left\{S_{3311}^{L}\right\}_{\psi\to 0}^{hkl}$ dependencies on $3\Gamma_{hkl}$ from Fig. E.6 were approximated by linear dependencies and the results are presented in Tab. E.1. By easy calculus it was possible to derive also a dependence of $\left\{S_{3333}^{L}\right\}_{\psi=0}^{hkl}$ on $3\Gamma_{hkl}$ (Tab. E.1). Considering the macroscopic elastic anisotropy and by applying the $3\Gamma_{hkl}^{*}$ from Sec. E.4.1 one could determine an inverse out-of-plane X-ray elastic modulus $\left\{S_{3333}^{L}\right\}_{\psi=0}^{3\Gamma^{*}}$ which is equal to the mechanical compliance $\left\{S_{3333}^{L}\right\}_{\psi=0}^{\mathrm{M}}$. The out-of plane Young's modulus can then be easily determined as follows

$$\frac{1}{\{E\}_{\psi=0}^{\mathrm{M}}}=\left\{S_{3333}^{L}\right\}_{\psi=0}^{\mathrm{M}} \tag{E.6}$$

The experimental out-of-plane Young's moduli of Cu and CrN thin films were easily found to be 169.40 and 240.79 GPa.

Table E.1: An experimental algorithm to determinate out-of-plane mechanical moduli of fiber textured thin films is presented. The macroscopic stress $\langle\sigma\rangle$ was determined using the curvature measurement (Fig.E.3). The $\{\epsilon_{33}^L\}_\psi^{hkl}$ dependencies on $\sin^2\psi$ (Fig. E.5) were analyzed in order to evaluate the intercepts $\{S_{3311}^L\}_{\psi=0}^{hkl} + \{S_{3322}^L\}_{\psi=0}^{hkl}$ and $\{S_{3333}^L\}_{\psi\to 0}^{hkl} - \{S_{3311}^L\}_{\psi\to 0}^{hkl}$ for $\psi \to 0$. The factor $3I_{hkl}^*$ indicates for which value of the X-ray anisotropic factor I the X-ray and mechanical elastic constants are equal (Sec. E.4.1). The compliances and the moduli were then extracted (Eq. E.6).

	$\langle\sigma\rangle$	$\{S_{3311}^L\}_{\psi=0}^{hkl} + \{S_{3322}^L\}_{\psi=0}^{hkl}$	$\{S_{3333}^L\}_{\psi=0}^{hkl} - \{S_{3311}^L\}_{\psi=0}^{hkl}$	$3I_{hkl}^*$	$\{S_{3333}^L\}_{\psi=0}^{hkl}$	$\{E\}_{\psi=0}^{\mathrm{M}}$
	(MPa)	(10^{-11} Pa^{-1})	(10^{-11} Pa^{-1})		(10^{-11} Pa^{-1})	GPa
Cu	275.9	0.62*3I_{hkl}-0.82	-1.04*3I_{hkl}+1.65	0.89	0.5903	169.40
CrN	-1415.9	-0.4*3I_{hkl}+0.074	0.53*3I_{hkl}+0.21	0.51	0.4153	240.79

E.8 Error discussion

The accuracy with which the out-of-plane Young's moduli were determined using the new algorithm is influenced by numerous factors. The approach is based on the combined application of well-established techniques, $\sin^2\psi$ and X-ray diffraction substrate curvature, which experimental accuracy was discussed in numerous papers [14, 18]. The combination of the both techniques can in the worst case results in the accumulation of the experimental errors. The exactness of the elastic strain characterization using the $\sin^2\psi$ method can be improved by increasing the number of measured reflections (Fig E.5).
Another source of the errors can originate from the not-accurate $3\Gamma^*_{hkl}$ parameter which was (due to practical reasons) determined using an empirical equation. The parameter can be determined exactly using a numerical ODF analysis of the texture data or estimated from the pole figure plots. The higher the crystal elastic anisotropy of the materials the more significantly the $3\Gamma^*_{hkl}$ inaccuracy will contribute to the errors when determining the moduli. Relatively large experimental errors can occur when the monocrystalline substrate under the film is plastically deformed during the structural characterization. In that case the Stoney's formula does not hold. For this reason, it is important to pay a significant attention when preparing samples. It is supposed that in the present case the moduli in Tab. E.1 were determined with a precision of about ± 15 %.

E.9 Conclusion

A new simple self-consistent X-ray diffraction technique was used to quantify out-of-plane Young's moduli of fiber textured thin films. The advantage of the new technique remains in the fact that moduli are determined non-destructively and using a static diffraction experiment. The experimental moduli represent volume-averaged data and can be used *e.g.* as an input for finite element modeling.

E.10 Acknowledgement

This work was supported by the Austrian NANO Initiative via a grant from the Austrian Science Fund FWF within the project "StressDesign - Development of Fundamentals for Residual Stress Design in Coated Surfaces".

E.11 References

[1] Suresh, S. and Freund, L. B. *Thin Film Materials Stress, Defect Formation and Surface Evolution.* Cambridge University Press, Cambridge, (2003).

[2] Hultman, L. *Vacuum* **57**(1), 1–30 (2000).

[3] Fischer-Cripps, A. C. *Nanoindentation.* Springer, New York, (2004).

[4] Hurley, D. C., Tewary, V. K., and Richards, A. J. *Meas. Sci. Technol.* **12**(9), 1486–1494 (2001).

[5] Read, D. T., Cheng, Y. W., Keller, R. R., and McColskey, J. D. *Scr. Mater.* **45**(5), 583–589 (2001).

[6] Leisure, R. and Willis, F. *J. Phys.: Condens. Matter* **9**, 6001–6029 (1997).

[7] Eiper, E., Martinschitz, K. J., Gerlach, J. W., Lackner, J. M., Zizak, I., Darowski, N., and Keckes, J. *Zeitschrift fr Metallkunde* **96**(9), 1069–1073 (2005).

[8] Eiper, E., Martinschitz, K. J., and Keckes, J. *Powder Diffr.* **21**(1), 25–29 (2006).

[9] Martinschitz, K. J., Eiper, E., Massl, S., Köstenbauer, H., Daniel, R., Fontalvo, G., Mitterer, C., and Keckes, J. *J. Appl. Cryst.* **39**, 777–783 (2006).

[10] Martinschitz, K. J. and Keckes, J. *J. Appl. Cryst.* , First paper in series (2008).

[11] Hill, R. *Proc. R. Soc. London, Ser. A* **65**(389), 349–355 (1952).

[12] Stoney, G. G. *Proc. Phys. Soc. London, Sect. A* **82**, 172 (1909).

[13] Segmüller, A., Noyan, I. C., and Speriosu, V. S. *Prog. Cryst. Growth Charact. Mater.* **18**, 21–66 (1989).

[14] Zhao, Z. B., Hershberger, J., Yalisove, S. M., and Bilello, J. C. *Thin Solid Films* **415**(1-2), 21–31 (2002).

[15] Keckes, J., Eiper, E., Martinschitz, K. J., Köstenbauer, H., Daniel, R., and Mitterer, C. *Rev. Sci. Instrum.* **78**(3), – (2007).

[16] Stickforth, J. *Tech. Mitt. Krupp - Forsch.-Ber.* **24**(3), 89–102 (1966).

[17] Bollenrath, F., Hauk, V., and Müller, E. H. *Z. Metallkd.* **58**, 76–82 (1967).

[18] Noyan, I. C. and Cohen, J. B. *Residual Stress Measurement by Diffraction and Interpretation.* Springer, (1987).